

1 **Anatomy of the magmatic plumbing system of Los Humeros Caldera (Mexico): implications for geothermal**  
2 **systems**

3

4 Federico Lucci<sup>1, \*</sup>, Gerardo Carrasco-Núñez<sup>2</sup>, Federico Rossetti<sup>1</sup>, Thomas Theye<sup>3</sup>, John C. White<sup>4</sup>, Stefano  
5 Urbani<sup>1</sup>, Hossein Azizi<sup>5</sup>, Yoshihiro Asahara<sup>6</sup>, and Guido Giordano<sup>1, 7</sup>

6

7 <sup>1</sup>Dipartimento di Scienze, Sez. Scienze Geologiche, Università Roma Tre, Largo S. L. Murialdo 1, 00146 Roma,  
8 Italy

9 <sup>2</sup>Centro de Geociencias, Universidad Nacional Autónoma de México, Campus UNAM Juriquilla, 76100,  
10 Queretaro, Mexico

11 <sup>3</sup>Institut für Anorganische Chemie, Universität Stuttgart, Stuttgart, Germany

12 <sup>4</sup>Department of Geosciences, Eastern Kentucky University, Richmond, KY 40475, USA

13 <sup>5</sup>Mining Department, Faculty of Engineering, University of Kurdistan, Sanandaj, Iran

14 <sup>6</sup>Department of Earth and Environmental Sciences, Graduate School of Environmental Studies, Nagoya  
15 University, Nagoya 464-8601, Japan

16 <sup>7</sup>CNR - IDPA, Via Luigi Mangiagalli 34, 20133 Milano

17 *\*Corresponding Author e-mail: [federico.lucci@uniroma3.it](mailto:federico.lucci@uniroma3.it)*

18

19 **ABSTRACT**

20 Understanding the anatomy of magma plumbing systems of active volcanoes is essential not only for  
21 unraveling magma dynamics and eruptive behaviors, but also to define the geometry, depth and temperature  
22 of the heat sources for geothermal exploration. The Pleistocene-Holocene Los Humeros volcanic complex is  
23 part of the Eastern Trans-Mexican Volcanic Belt (Central Mexico) and it represents one of the most important  
24 exploited geothermal fields in Mexico with *ca.* 90 MW of produced electricity.

25 A field-based petrologic and thermobarometric study of lavas erupted during the Holocene (post-Caldera  
26 stage) has been performed with the aim to decipher the anatomy of the magmatic plumbing system existing  
27 beneath the caldera. New petrographical, whole rock major element data and mineral chemistry were  
28 integrated within a suite of **mineral-liquid** thermobarometric models. Compared with previous studies where  
29 a single voluminous melt-controlled magma chamber (or “Standard Model”) at shallow depths was proposed,  
30 our results support a more complex and realistic scenario characterized by a heterogeneous multilayered  
31 system comprising a deep (*ca.* 30 km) basaltic reservoir feeding progressively shallower and smaller distinct  
32 stagnation layers, pockets and batches up to very shallow conditions (1kbar, *ca.* 3km). Evolution of melts in  
33 the feeding system is mainly controlled by differentiation processes **through fractional crystallization**  
34 **(plagioclase + clinopyroxene + olivine + spinel assemblage). We demonstrate the inadequacy of conceptual**  
35 **models based on the classical, melt-dominated, single, voluminous, long-lived magma chamber for the**  
36 **magmatic plumbing systems at LHVC. We instead propose a magmatic plumbing system made of multiple,**  
37 **more or less interconnected magma transport and storage layers within the crust, feeding small (ephemeral)**  
38 **magma pockets at shallow-crust conditions. This revised scenario provides a new configuration of the heat**  
39 **source feeding the geothermal reservoir that should be taken into account to drive future exploration and**  
40 **exploitation strategies.**

41

42 **Keywords**

43 Magmatic plumbing system, Thermobarometry, Calderas, Los Humeros, Trans Mexican Volcanic Belt, heat  
44 source, geothermal exploration

45

## 46 1.INTRODUCTION

47 Recent views on the structure of volcanic plumbing systems have deeply changed, moving from the  
48 “Standard Model” (*sensu* Gualda and Ghiorso, 2013) of a single, bowl-shaped magma chamber inside which  
49 all petrologic processes of differentiation and assimilation occur (e.g. Hildreth, 1979, 1981; Hildreth and  
50 Wilson, 2007) to more complex arrays of stratified and variably interconnected of transient magma  
51 accumulation zones, set in largely crystallized and vertically extensive mush zones (e.g., Bachman and  
52 Bergantz, 2004; 2008; Cashman and Giordano, 2014; Cashman et al., 2017). Furthermore, the time required  
53 for the assembly of large magma chambers is now believed to be very short, in terms of decades to few  
54 thousands of years for tens to hundreds of km<sup>3</sup> of eruptible magma (e.g. Glazner, 2004; Charlier et al., 2007),  
55 which are then rapidly evacuated during eruptions of caldera forming ignimbrites (e.g., Begué et al., 2014;  
56 Rivera et al., 2014; Wotzlaw et al, 2014; Matthews et al., 2015; Carrasco-Núñez et al., 2018). Key factors in  
57 determining the internal architecture of the magmatic systems is the magma intrusion rate that controls  
58 whether successive pulses of magma will coalesce to form progressively larger chambers, as well as the  
59 formation of ductile shells surrounding the magma chamber that prevent country rock failure, favoring the  
60 inflation of the reservoir (Jellinek and de Paolo, 1981; Annen, 2009). Numerical simulations suggest that  
61 caldera systems smaller than 100 km<sup>2</sup> are feed by plumbing systems encapsulated by country rocks that  
62 remain sufficiently brittle, while larger systems are more ductile favoring increase in size (Gregg et al., 2012).  
63 The implications of such innovative conceptual models on the modeling of the heat source in magmatic-  
64 bearing geothermal systems are **significant**. Nonetheless, common numerical modeling of conductive-  
65 convective heat transfer in caldera-related geothermal systems have commonly envisaged the classic magma  
66 chamber as a single body, more or less chemically stratified entirely at magmatic temperatures, whose  
67 dimensions and depths have been usually constrained by volcanological and petrological data (e.g. Verma,  
68 1985; Wohletz et al., 1999). More complex modeling requires the “unpacking” of the stratigraphy of a volcano  
69 by the identification of the various “magma chambers” or magma storage layers that fed the different  
70 **eruptions in space and time** (e.g., Solano et al., 2014; Di Renzo et al., 2016; Cashman et al., 2017; Jackson et  
71 **al., 2018**).

72 A key to decipher where magmas are stored and, therefore, the anatomy of a magmatic plumbing system, is  
73 the understanding of pre-eruptive processes such as mineral crystallization, migration and stagnation of  
74 melts prior to their eruption (Feng and Zhu, 2018, Putirka, 2008; Keiding and Sigmarsson, 2012; Scott et al.,  
75 2012, Barker et al., 2015; Jeffery et al., 2013; Cashman and Giordano, 2014; Pamukcu et al., 2015; Lucci et  
76 al., 2018). As a matter of fact, early segregated minerals reflect the magmatic environment (i.e., pressure –  
77 temperature – magma/fluid composition, oxidation state) and, therefore, with their growth, texture and  
78 chemistry provide an important archive of information (**Ginibre et al., 2002**; Feng and Zhu, 2018; Ginibre et  
79 al., 2007; **Streck, 2008**; Giuffrida and Viccaro, 2017; Viccaro et al., 2016; Putirka et al., 2008; Lucci et al., 2018).  
80 Accordingly, petrographic observations and mineral chemistry of primary minerals, integrated with

81 opportunely selected thermobarometry models (e.g., Putirka, 2008; Masotta et al., 2013) could lead to the  
82 comprehension and reconstruction of the magmatic storage/feeding systems of the erupted products (Feng  
83 and Zhu, 2018; Giuffrida and Viccaro, 2017; Elardo and Shearer, 2014; Petrone et al., 2016; Zheng et al., 2016;  
84 Eskandari et al., 2018; Shane and Coote, 2018; Scott et al., 2012; Stroncik et al., 2009; Barker et al., 2015;  
85 Jeffery et al., 2013; Keiding and Sigmarsson, 2012).

86 In this paper we present a geothermobarometric study of the post-caldera, Pleistocene-Holocene products  
87 of Los Humeros volcanic complex (LHVC), located at the eastern termination of the Neogene-Quaternary  
88 Trans-Mexican Volcanic Belt (TMVB) (Fig. 1), with the aim to reconstruct the present-day geometry and  
89 structure of the magmatic plumbing system. These data are used to build up a conceptual model for the  
90 magmatic heat source of the active and currently exploited geothermal system. The magmatic heat source  
91 for LHVC has been constrained by the geometry of the caldera, the volume and mass balance calculations of  
92 the associated ignimbrites (Ferriz and Mahood, 1984, 1987; Verma, 1984, 1985a, 1985b, Verma et al., 1990;  
93 Verma and Andaverde, 1995; Verma et al., 2011; Verma et al. 2013), all related to a single magma body.

94 Our results allow us to propose of a new and more realistic vision of the magmatic plumbing systems made  
95 of multiple interconnected magma stagnation layers within the crust. These new findings must be considered  
96 into the new developing conceptual geothermal models to improve strategies for exploration and  
97 exploitation of the geothermal system within the LHVC. The results and approach presented in this work have  
98 also a general value and could represent an efficient strategy to explore and reconstruct, through petrological  
99 investigation, the pre-eruptive geometry and the anatomy of active magmatic feeding systems.

100

## 101 **2.GEOLOGICAL SETTING**

### 102 **2.1 Regional Geology**

103 LHVC is the largest and easternmost Quaternary caldera (Fig. 1) of the 1200 km-long active continental arc  
104 of the Trans-Mexican Volcanic Belt (TMVB), generated since ca. 20 Ma by the subduction of Cocos plate  
105 beneath central Mexico (e.g. Demant, 1978, Ferrari et al. 1999, 2012; Gomez-Tuena et al., 2003, 2007a,  
106 2007b, 2018; Norini et al., 2015). LHVC is located in the eastern sector of the TMVB, which is characterized  
107 by monogenetic volcanism, scattered basaltic cinder and scoria cones, maar volcanoes of basaltic and  
108 rhyolitic composition, large rhyolitic domes and major stratovolcanoes such as Pico de Orizaba (or  
109 Citlaltépetl) and Cofre de Perote (e.g., Yáñez and García, 1982; Negendank et al., 1987; Carrasco-Núñez et  
110 al., 2010, 2012a;).

111 The Paleozoic to Mesozoic crystalline basement of eastern TMVB is exposed along the Teziutlán Massif  
112 (Viniegra, 1965; Ferriz and Mahood, 1984) made of metamorphic (greenschists K-Ar dated at  $207 \pm 7$  Ma, in  
113 Yáñez and García, 1982) and intrusive (granodiorites and granites with whole-rock K-Ar ages of  $246 \pm 7$  Ma  
114 and  $181 \pm 5$  Ma, Yáñez and García, 1982) rocks. The crystalline basement is partially covered by a thick, highly  
115 deformed Mesozoic sedimentary succession part of the Sierra Madre Oriental NW-SE thrusts and folds belt

116 formed by the Late Cretaceous to Paleocene compressional Laramide Orogeny (e.g. Campos-Enriquez and  
117 Garduño-Monroy, 1987; Suter, 1987; Fitz-Díaz et al., 2018). Oligocene to Miocene granodiorite and syenite  
118 intrusions are randomly exposed within the area (whole-rock K-Ar ages of 31-15 Ma, Yáñez and García, 1982).  
119 Miocene volcanism in the area is represented by andesites of the Cerro Grande volcanic complex (Gómez-  
120 Tuena and Carrasco-Núñez, 2000), dated at 8.9 to 11 Ma (K/Ar method on whole-rock, Carrasco-Núñez et al.  
121 1997), and the Cuyoaco Andesite dated at 10.5 Ma (K/Ar method, Yáñez and García, 1982) to the west of  
122 LHVC, which may correlate with the Alseseca Andesite (Yáñez and García, 1982) exposed to the north.  
123 Neogene andesitic volcanism (Ferriz and Mahood, 1984; Yáñez and García, 1982) represented by the  
124 Teziutlán Andesite, K-Ar dated (whole-rock) between 3.5 and 5 Ma by Yáñez and García (1982) and at 1.55  
125 Ma by Ferriz and Mahood (1984). This andesitic activity was recently dated by the  $^{40}\text{Ar}/^{39}\text{Ar}$  method at 2.61-  
126 1.46 Ma (Carrasco-Núñez et al., 2017a) and correlates with most of the thick andesitic successions of the  
127 subsurface geology of LHVC.

128

## 129 **2.2 Los Humeros Volcanic Complex**

130 The volcanic evolution of the LHVC consists of three main stages (Carrasco-Núñez et al., 2018): (i) pre-caldera  
131 stage; (ii) caldera stage; and (iii) post-caldera stage. The pre-caldera stage is represented by relatively  
132 abundant rhyolitic domes, which erupted mainly to the western side of Los Humeros caldera, with an isolated  
133 spot to the south, and some buried lavas identified in the geothermal well-logs (Carrasco-Núñez et al.,  
134 2017a). This volcanism has been recently dated by both U-Th and  $^{40}\text{Ar}/^{39}\text{Ar}$  methods (Carrasco-Núñez et al.,  
135 2018), providing ages spanning from  $693.0 \pm 1.9$  ( $^{40}\text{Ar}/^{39}\text{Ar}$ , plagioclase) to  $270 \pm 17$  ka (U/Th, zircon), which  
136 overlap with the age range obtained from other domes of the western sector outside the caldera, where K-  
137 Ar ages (sanidine) of  $360 \pm 100$  ka and  $220 \pm 40$  ka were obtained (Ferriz and Mahood, 1984). The Caldera stage  
138 consists of two major caldera-forming events, separated by a large Plinian eruptive episode. The first and  
139 largest caldera-forming eruption produced Los Humeros caldera (18 km in diameter) during the  
140 emplacement of the Xaltipan ignimbrite, a rhyolitic, welded to non-welded, ash-rich deposit, radially  
141 distributed around the caldera. The dense rock equivalent (DRE) volume of this event was estimated at 115  
142  $\text{km}^3$  by Ferriz and Mahood (1984). The age of the Xaltipan ignimbrite was established by whole-rock K-Ar  
143 dating at  $460 \pm 20$  ka (plagioclase) and  $460 \pm 130$  ka (biotite) (Ferriz and Mahood, 1984), however Carrasco-  
144 Núñez et al. (2018) based on coupled zircon U-Th dating and  $^{40}\text{Ar}/^{39}\text{Ar}$  method (plagioclase) geochronology  
145 provided a younger age of  $164.0 \pm 4.2$  ka.

146 Following this catastrophic event an eruptive pause occurred, resuming with a sequence of intermittent  
147 Plinian episodes at  $70 \pm 23$  ka ( $^{40}\text{Ar}/^{39}\text{Ar}$  method on plagioclase, Carrasco-Núñez et al., 2018), separated by  
148 short gaps marked by thin paleosoils. The deposits consist of thick (1-6 m) coarse pumice-rich, well-sorted,  
149 massive and diffuse-stratified layers, rhyodacitic in composition, which are grouped as the Faby Tuff (Ferriz  
150 and Mahood 1984; Willcox, 2011). The second caldera-forming episode produced the 9-10 km large Los

151 Potrereros caldera, which is associated with the emplacement of the compositionally-zoned andesitic-  
152 rhyodacitic-rhyolitic Zaragoza ignimbrite (Carrasco-Núñez et al., 2012b). This is an intraplinian pyroclastic  
153 flow deposit, with an estimated volume of ca. 15 km<sup>3</sup> DRE (Carrasco-Núñez and Branney, 2005). Previous  
154 ages of this unit were reported at 100 ka (K-Ar dating, plagioclase: Ferriz and Mahood, 1984) and at 140±24  
155 ka (<sup>40</sup>Ar/<sup>39</sup>Ar method, plagioclase: Willcox, 2011). However, a new <sup>40</sup>Ar/<sup>39</sup>Ar (on plagioclase) younger age of  
156 69±16 ka for the Zaragoza ignimbrite was recently obtained (Carrasco-Núñez et al., 2018), confirmed by the  
157 fact the Zaragoza ignimbrite overlies a rhyodacitic lava flow dated at 74.2±4.5 ka (zircon U-Th dating).  
158 According to Carrasco-Núñez et al. (2018) during the post-caldera stage (Fig. 1) two different eruptive phases  
159 occurred. The first one was a late Pleistocene resurgent phase characterized by the emplacement of felsic  
160 domes in the central area at about 44.8±1.7 ka (zircon U-Th ages; Carrasco-Núñez et al., 2018), which is  
161 slightly younger than the previously reported whole-rock K-Ar date (60±20 ka, glass: Ferriz and Mahood,  
162 1984). Outside of the caldera, to the north, a rhyolitic dome erupted at 50.7±4.4 ka (<sup>40</sup>Ar/<sup>39</sup>Ar, plagioclase;  
163 Carrasco-Núñez et al., 2018), which was followed by a sequence of explosive eruptions, producing dacitic  
164 pumice fall units (Xoxoctic Tuff, 0.6 km<sup>3</sup>) and interbedded breccia and pyroclastic flows deposits of the Llano  
165 Tuff (Ferriz and Mahood 1984; Willcox, 2011), with a maximum age of 28.3±1.1 ka (C-14, Cal BP 30630, Rojas-  
166 Ortega, 2016). The second eruptive phase of the post-caldera stage is a Holocene ring-fracture and bimodal  
167 phase that occurred towards the south, north and central part of Los Humeros caldera (Carrasco- Núñez et  
168 al., 2017). It is characterized by alternated episodes of effusive and explosive volcanism with a wide range of  
169 compositions, spanning from basaltic-andesitic, basaltic trachytic, trachyandesitic lava flows and dacitic,  
170 trachydacitic, andesitic and basaltic pumice and scoria fall deposits erupted by tens of monogenetic eruptive  
171 centers located in the LHVC (Ferriz and Mahood, 1984; Dávila-Harris and Carrasco-Núñez, 2014; Norini et al.,  
172 2015; Carrasco-Núñez et al., 2017b). Most of the effusive activity was firstly considered within a range of 40-  
173 20 ka (whole-rock K-Ar dating, Ferriz and Mahood, 1984), however, recent dating reveals that most of this  
174 activity is Holocene (Carrasco et al., 2017b). Trachyandesitic and andesitic basalts lavas erupted to the north  
175 of the LHVC at about 8.9±0.03 ka (C-14 age, Carrasco-Núñez et al, 2017b). A rhythmic alternation of  
176 contemporaneous bimodal explosive activity produced trachyandesitic and basaltic fall layers grouped as the  
177 Cuicuiltic Member erupted at 7.3±0.1 ka (C-14 age, Dávila-Harris and Carrasco-Núñez, 2014). This activity  
178 migrated towards the southern caldera rim to forms a well-defined lava field. This ring-fracture episode  
179 erupted trachyandesite and olivine-bearing basaltic lava flows, at 3.9±0.13 ka (C-14 age, Carrasco-Núñez et  
180 al, 2017b), and the most recent eruptions erupted trachytic lava flows near the SW caldera rim, at 2.8± 0.03  
181 ka (C-14 age, Carrasco-Núñez et al, 2017b).

182

### 183 **2.3 Los Humeros geothermal system**

184 The LHVC hosts one of the three most important geothermal fields in Mexico, with an installed 93 MW of  
185 electric power produced from 20 geothermal wells (Romo-Jones et al., 2017). The existing conceptual models

186 for the Los Humeros geothermal field (LHGF) (see Norini et al., 2015 for a review) stem upon the hypothesis  
187 of a unique, large and voluminous cooling magma chamber of 1000-1500 Km<sup>3</sup> in volume, at depth of 5 to 10  
188 km from the surface (Verma, 1984, 1985a, 1985b, 2000; Verma et al., 1990; Verma and Andaverde, 1995;  
189 Verma et al., 2011; Verma et al. 2013; Carrasco-Núñez et al. 2018), representing the heat source of the  
190 geothermal field (Martínez et al., 1983; Verma, 1983, 2000; Campos-Enríquez and Garduño-Monroy, 1987).  
191 However, the LHGF is characterized by a low number of productive geothermal wells (ca. 20 out of 50; Norini  
192 et al., 2015; Carrasco-Núñez et al., 2017a). The confined distribution of these productive wells along the  
193 NNW-SSE trending “Maxtaloya-Los Humeros-Loma Blanca” fault system (MHBfs in Fig. 1) cutting across the  
194 Los Potreros caldera (e.g., Norini et al., 2015; Carrasco-Núñez et al., 2017a) also corresponds to the almost  
195 unique, narrow and sharp surface thermal anomaly recognized within the caldera (Norini et al., 2015). These  
196 observations raise doubts on the existence of a voluminous superficial heat source feeding the LHGF and  
197 makes it important, for a better comprehension and exploitation of the geothermal resource, a revised  
198 assessment of the structure of the magmatic plumbing system beneath LHVC.

199

### 200 3. MATERIALS AND METHODS

201 In this work we focus on petrographical investigations, textural and chemical (mineral chemistry and major-  
202 elements bulk-rock) characterization of the Los Humeros post-caldera stage (LHPCS) (Carrasco-Núñez et al.  
203 2017b). Following the recently published geological map (Carrasco-Núñez et al. 2017b) and geochronology  
204 (Carrasco-Núñez et al. 2018) of the LHVC, **more than fifty samples of the LHPCS lavas were collected in the**  
205 **field** with the aim to describe all the compositional variability of erupted products during the post-caldera  
206 stage activity (Figs. 1, 2a-d). In the description of the volcanic units, abbreviations follow Carrasco et al.  
207 (2017b). **Petrographic characterization through polarized-light microscopy (PLM) was produced for near all**  
208 **collected samples. The most preserved and representative samples of every major LHPCS volcanic unit were**  
209 **than selected (Fig. 1) for bulk and mineral chemistry investigations.**

210 **With respect to the intra-caldera domain (Fig. 2a), we selected lava samples belonging to: (i) LH27-1 from the**  
211 **mafic lavas inside the Xalapasco Crater (Qb1), (ii) LH27-2 from the Maxtaloya trachyandesites (Qta4)**  
212 **constituting the rim-walls of Xalapasco craters, (iii) LH4 from San Antonio-Las Chapas lavas (Qta3)**  
213 **outcropping in the Los Humeros town, (iv) LH5-2 from mafic lavas (Qb1) outcropping west to Los Humeros**  
214 **town, (v) LH5-1 from Chicomiapa-Los Parajes felsic lavas (Qt2) outcropping in the north-western part of Los**  
215 **Potreros caldera, (vi) LH6-1 from El Pajaro unit (Qt1) outcropping in the north-western part of Los Potreros**  
216 **caldera. In addition to these units, we also selected three more samples (LH13, LH26-1 and LH26-2) from**  
217 **lavas and domes of intermediate compositions, outcropping (Fig. 2b-c) in the central part of Los Potreros**  
218 **caldera between Xalapasco crater and Los Humeros town, and not reported on the published geological map.**

219

220 Concerning the extra-caldera products (Fig. 2d), we selected one sample for each of the four major lava flows:  
221 (i) LH15 from El Limón lava flow (Qab), (ii) LH21-2 from Sarabia lava flow (Qta1), (iii) LH17 from Tepeyahualco  
222 lava flow (Qtab), and (iv) LH18 from Texcal lava flow (Qb1).

223 The samples were investigated first by optical microscopy and then through back scattered electron (BSE)  
224 imaging for the definition of magmatic fabrics, textures and constituent mineral assemblages. Mineral  
225 chemistry was then defined through electron microprobe analyses (EMPA). Whole rocks (major and trace  
226 element) composition of selected samples was obtained through ion coupled plasma – optical emission (ICP-  
227 OE) and X-ray fluorescence (XRF) analyses. Analytical protocols are described in the Appendix A.

228 In the following, mineral abbreviations follow Whitney and Evans (2010), whereas types of zoning and  
229 textures are after Ginibre et al. (2002), Streck (2008) and Renjith (2014).

230

#### 231 4. MAJOR ELEMENT BULK COMPOSITION

232 Studied samples show a continuous series from mafic to felsic compositions, with SiO<sub>2</sub> ranging 46.5-67.6 wt%,  
233 and Na<sub>2</sub>O + K<sub>2</sub>O ranging 3.4-9.2 wt% (with K<sub>2</sub>O/Na<sub>2</sub>O < 1) (Fig. 3a; Table 1). LHPCS mafic rocks (SiO<sub>2</sub> < 50 wt%;  
234 3 samples) show composition with SiO<sub>2</sub> 46.5-49.4 wt%, Al<sub>2</sub>O<sub>3</sub> 16.2-17.1 wt%, CaO 9.8-10.7 wt%, MgO 8.0-8.4  
235 wt% with Mg# (molar MgO/[MgO+FeO<sub>tot</sub>]) = 60-61 and Na<sub>2</sub>O+K<sub>2</sub>O ranging 3.4-3.5 wt%. LHPCS intermediate  
236 rocks (50 < SiO<sub>2</sub> < 63 wt%; 8 samples) contain 54.4-62.1 wt% SiO<sub>2</sub>, with Al<sub>2</sub>O<sub>3</sub> 15.7-20.7 wt%, Na<sub>2</sub>O+K<sub>2</sub>O 5.3-7.1  
237 wt%, MgO 2.2-3.6 wt% (Mg# 43-51), and low CaO 4.6-8.5 wt%. LHPCS felsic rocks (SiO<sub>2</sub> > 63 wt%; 2 samples)  
238 show SiO<sub>2</sub> ranging 64.9-67.6 wt%, associated with Al<sub>2</sub>O<sub>3</sub> 15.5-15.8 wt%, MgO 0.7-1.2 wt% (Mg#: 26-34), CaO  
239 2.1-2.8 wt%, and Na<sub>2</sub>O+K<sub>2</sub>O 8.2-9.2 wt%.

240 On the total alkali versus silica (TAS) diagram (Le Maitre et al., 2002) LHPCS lavas span from basalts to  
241 trachytes (Fig. 3b). Los Humeros mafic rocks fall in the “Basalt” field and, following the existing literature  
242 (e.g., Barberi et al., 1975, Bellieni et al., 1983; Le Maitre et al., 2002; White et al., 2009; Giordano et al., 2012),  
243 can be classified as mildly-alkaline (or transitional) basalts and alkali-basalts. The high TiO<sub>2</sub> contents (1.34-1.5  
244 wt%), together with MgO < 12 wt% and low Al<sub>2</sub>O<sub>3</sub>/TiO<sub>2</sub> values (average value 11.5) exclude the LH mafic rocks  
245 as high-Mg melts (picrites) or komatiites (e.g., Redman and Keays, 1985; Arndt and Jenner, 1986; Le Maitre  
246 et al., 2002; Gao and Zhou, 2013; Azizi et al., 2018a, 2018b).

247 Intermediate products fall in the “Basaltic trachyandesites” and “Trachyandesites” fields; these rocks will be  
248 referred hereafter as “trachyandesites”. The Los Humeros felsic (i.e., SiO<sub>2</sub> > 63 wt%) lava samples belonging  
249 to the post-caldera stage fall in the “Trachyte” field. Selected Harker diagrams for major elements are  
250 presented in Figure 3, using SiO<sub>2</sub> wt% as differentiation index. Negative correlations are observed for CaO  
251 (Fig. 3c) and Mg# (Fig. 3d), whereas positive correlations are observed for Na<sub>2</sub>O (Fig. 3c).

252

#### 253 5. PETROGRAPHY

##### 254 5.1 Basalts



255 LHPCS basalts show vesicle-rich (up to 35 vol%) highly-porphyritic (phenocrysts up to 50 vol%) textures (Fig.  
256 4a-d). Studied basalts do not show presence of fragments from host-rocks or from previous magmatic rocks,  
257 therefore can be defined as lithic-free (e.g., Geshi and Oikawa, 2014). The fabric is fluidal as defined by the  
258 alignment of plagioclase laths in the groundmass. Based on the presence of clinopyroxene (Cpx) in the  
259 mineral assemblage, basalts can be further subdivided into: (i) Cpx-free basalt of extra-caldera Texcal lava  
260 flow (LH18); and (ii) Cpx-bearing basalts of intra-caldera lavas at western Los Potreros and at Xalapasco crater  
261 (LH5-2 and LH27-1, respectively).

262 Cpx-free basalt (LH18) contains euhedral to subhedral olivine (ca. 20 vol%) and euhedral to anhedral  
263 plagioclase (ca. 25-30 vol%) phenocrysts in a holocrystalline groundmass consisting of plagioclases with  
264 swallow-tail morphology, dendritic to spinifex olivines and opaque oxides (Fig. 4a, b). Olivine and plagioclase  
265 phenocrysts are generally slightly chemically zoned (see below), showing homogeneous cores with normal  
266 concordant monotonous zoning texture at outer rim (Fig. 4a, b). Occasionally, major phenocrysts of olivine  
267 (up to 2.5 mm in size) with Cr-spinel inclusions are observed (Fig. 4a). It is worth notice that no pyroxenes  
268 are observed in this basalt.

269 Cpx-bearing intra-caldera basalts (LH5-2, LH27-1) show euhedral to subhedral plagioclase (ca. 25 vol%),  
270 euhedral olivine (ca. 10-15 vol%), subhedral to anhedral yellow to colorless clinopyroxene (ca. 10-15 vol%)  
271 and rare subhedral anorthoclase (< 2 vol%) phenocrysts (Fig. 4c) in a holocrystalline groundmass (Fig. 4d).  
272 The latter is made up of (in order of microlites abundance) elongated platy plagioclase, olivine, colorless to  
273 green clinopyroxene, opaque oxides and rare alkali-feldspar. All phenocrysts show core-rim zoning textures  
274 (Fig. 4c, d) and in particular: (i) olivine, plagioclase and clinopyroxene with homogeneous cores and normal  
275 concordant monotonous zoning at outer rims, (ii) plagioclase and clinopyroxene with homogeneous cores  
276 and low-amplitude euhedral oscillatory zoning at rims, (iii) rare plagioclase and clinopyroxene with  
277 homogeneous cores and normal concordant step zoning at rims, and (iv) very rare plagioclase with patchy  
278 cores and normal convolute monotonous zoning at rims. Large phenocrysts of olivine (up to 1.5 mm in size)  
279 and plagioclase (up to 3 mm in length) are commonly observed. Vesicle size is up to 5mm in diameter.

280

## 281 5.2 Trachyandesites

282 LHPCS intermediate volcanic products are lithic-free and show low- to medium-porphyritic textures  
283 (phenocrysts ranging 10-40 vol%), with a general fluidal fabric as indicated by orientation of plagioclase and  
284 clinopyroxene laths in the groundmass (Fig. 4e, f). Intermediate products vary from poorly vesiculated (< 10  
285 vol% in LH13) to vesicle-rich (ca. 30 vol% in LH4) lavas. In the highest vesiculated sample (LH4), size of vesicles  
286 (3-5 mm in diameter) is comparable to those of intra-caldera basalts (LH5-2, LH27-1). Based on the presence  
287 of orthopyroxene (Opx) in the mineral assemblage, rocks of intermediate compositions can be further  
288 subdivided into: (i) Opx-free (LH21, LH15); and (ii) Opx-bearing (LH4, LH13, LH17, LH26-1, LH26-2, LH27-2)  
289 trachyandesites.

290 Opx-free trachyandesites shows euhedral to subhedral plagioclase (ca. 15-20 vol%), euhedral to subhedral  
291 olivine (ca. 10 vol%), euhedral to anhedral yellow-to-colorless clinopyroxene (ca. 10-20 vol%), subhedral  
292 alkali-feldspars (ca. 10-15 vol%) phenocrysts, in a holocrystalline microcrystalline groundmass composed of  
293 elongated platy plagioclase, colorless clinopyroxene, olivine, alkali-feldspar and opaque oxides, in order of  
294 microlites abundance.

295 Opx-bearing trachyandesites are generally characterized by euhedral to subhedral plagioclase (ca. 15-20  
296 vol%), euhedral to subhedral clinopyroxene (ca. 10-20 vol%), euhedral colorless orthopyroxene (ca. 10-20  
297 vol%), euhedral to subhedral alkali-feldspars (ca. 10-15 vol%) and euhedral to subhedral olivine (< 10 vol%)  
298 phenocrysts in a holocrystalline to hypohyaline microcrystalline groundmass made of feldspar (plagioclase  
299 and alkali-feldspars) microlites, pyroxene (clinopyroxene and orthopyroxene) microlites, olivine microlites,  
300 opaque minerals and glass (Fig. 4f). To note it is the olivine absence in the trachyandesitic sample LH27-2.

301 Most of phenocrysts observed in these intermediate products show zoning textures characterized by  
302 homogeneous cores surrounded by (i) monotonous zoning at outer rims, (ii) low-amplitude euhedral  
303 oscillatory zoning at rims and (iii) normal concordant step zoning at rim. Homogeneous unzoned  
304 clinopyroxene phenocrysts are commonly observed. Major phenocrysts of clinopyroxene (up to 2 mm in size)  
305 and plagioclase (up to 2 mm in length) characterized by homogeneous cores and normal concordant  
306 monotonous zoning are reported in all studied trachyandesites. It is also reported the presence of (i) rare  
307 clinopyroxene phenocrystals with growth mantle textures, (ii) rare plagioclase phenocrysts with patchy  
308 rounded zone corners cores, (iii) very rare clinopyroxenes with homogeneous cores and growth mantle  
309 texture at rims are observed. Very rare large phenocrysts of olivine (1.5-2.0 mm in size) presenting resorption  
310 patterns at rim and characterized by spinel inclusion are reported in the LH26-1 sample.

311

### 312 5.3 Trachytes

313 LHPCS trachytes show lithic-free phyric textures, with low porphyritic index (phenocrysts ranging 10-25 vol%),  
314 and fluidal fabrics as shown by iso-orientation of plagioclase, alkali-feldspars and clinopyroxene laths in the  
315 groundmass (Fig. 4g, h). They range from vesicle-poor (< 5 vol%) to vesicle-free textures, with size of vesicles  
316 never exceeding 0.05 mm in diameter. The two analyzed trachytic samples (LH5-1 and LH6) are both  
317 characterized by the presence of orthopyroxene; however, the two mineral assemblages differ substantially.  
318 The low-SiO<sub>2</sub> (64.93 wt%) LH5-1 trachyte is characterized by euhedral to subhedral phenocrystals of  
319 plagioclase (ca. 10-15 vol%), clinopyroxene (ca. 10 vol%), orthopyroxene (ca. 10 vol%), olivine (ca. 5-10 vol%)  
320 and sanidine (< 10 vol%), in a hypohyaline microcrystalline groundmass made of (in order of abundance of  
321 microlites and microcrystals) sanidine, orthopyroxene, clinopyroxene, rare plagioclase, rare olivine, rare  
322 opaque minerals and very rare glass. All phenocrysts are generally unzoned. Mafic phenocrysts with  
323 homogeneous cores surrounded by normal concordant monotonous zoning are also observed. Rare major  
324 plagioclase (up to 1.5 mm in length) phenocrysts present patchy cores and normal concordant step zoning

325 textures at rims. Rare major clinopyroxene (up to 1.0 mm in length) unzoned homogeneous phenocrystals  
326 show inclusions of olivine + magnetite.

327 The high SiO<sub>2</sub> (67.58 wt%) LH6 trachyte is made up of sanidine (ca. 10 vol%), plagioclase (ca. 5-10 vol%) and  
328 orthopyroxene (ca. 10 vol%) phenocrystals in a fine grained trachytic mesostasis. Only major plagioclase and  
329 orthopyroxene phenocrysts show core-rim zoning textures with homogeneous cores associated either with  
330 normal monotonous zoning or normal low-amplitude oscillatory zoning at rims. Dimension of phenocrysts  
331 are comparable to those of LH5-1 trachyte.

332

## 333 6. MINERAL CHEMISTRY

334 Mineral compositions as obtained from electron microprobe analyses and mineral formulae for mineral  
335 assemblages of LHPCS lavas are presented in Supplementary Tables 1, 2, 3, 4 and 5 (for feldspar,  
336 clinopyroxene, olivine, orthopyroxene and spinel and opaque minerals, respectively).

337

### 338 6.1 Feldspar

339 In basaltic rocks (Fig. 5a), feldspars are predominantly plagioclase. Plagioclase phenocrysts show anorthitic  
340 (XAn = 59-81%, average 67%) cores and normally zoned (XAn = 42-59%, average 53%) rims. Orthoclase  
341 component (XOr) is always less than 2%. Plagioclase microlites in the groundmass show andesine (XAn = 19-  
342 60%) composition, with XOr ranging 1-7%. Alkali-feldspars occur as both rare anorthoclase phenocrysts  
343 (Ab<sub>60</sub>Or<sub>37</sub>), and microlites in groundmass (Ab<sub>62-79</sub>Or<sub>9-35</sub>An<sub>0-13</sub>).

344 Plagioclase from trachyandesites (Fig. 5b) have anorthite-rich (XAn = 45-87%, average 67%) cores and  
345 normally zoned (XAn = 27-69%, average 48%) rims. Cores with XAn in the range 72-87% are observed in all  
346 major phenocrysts. Plagioclase core compositions are comparable to those of basalts. The XOr ranges 1-8%.  
347 Plagioclase microlites in groundmass show andesine (XAn = 29-63%) composition with XOr always less than  
348 10%. Alkali-feldspars occur as (i) anorthoclase (Ab<sub>59-68</sub>Or<sub>11-30</sub>) and sanidine (Ab<sub>49-50</sub>Or<sub>43-48</sub>) phenocrysts, and (ii)  
349 anorthoclase (Ab<sub>49-70</sub>Or<sub>15-38</sub>) and sanidine (Ab<sub>38-48</sub>Or<sub>47-61</sub>) microlites in groundmass.

350 Trachytes (Fig. 5c) show generally unzoned plagioclase phenocrysts with oligoclase-andesine (XAn = 26-45%)  
351 composition. Rare An-rich (XAn = 52-70%) cores are reported from major plagioclase phenocrysts in the low-  
352 silica trachyte LH5-1. The XOr is always less than 8%. Plagioclase microlites in groundmass are rare, with Ab-  
353 rich (An<sub>21-30</sub>Ab<sub>66-69</sub>Or<sub>4-10</sub>) composition. Alkali-feldspars are represented by anorthoclase as phenocrysts (Ab<sub>65</sub>-  
354 <sub>66</sub>Or<sub>20-21</sub>) and groundmass microlites (Ab<sub>64-66</sub>Or<sub>21-24</sub>).

355

### 356 6.2 Clinopyroxene

357 Apart from the LH18 basalt and LH6 trachyte, clinopyroxene, is the most common mafic mineral recognized  
358 in studied samples. It occurs generally as single crystals (Fig. 4e). However rare crystals showing growth  
359 mantle textures are locally reported in trachyandesites. Very rare phenocrysts in trachyandesites show

360 **patchy cores.** Major clinopyroxene phenocrysts in trachyandesites and trachytes contain inclusions (Fig. 4e,  
361 g) of olivine, magnetite and plagioclase.

362 Polarized light microscopy coupled with BSE images and chemical investigations highlighted the presence of  
363 unzoned (Fig. 4g) and zoned (**homogeneous cores associated to low-amplitude oscillatory zoning or normal**  
364 **monotonous zoning or normal step zoning textures at rims; e.g., Fig. 4e)** clinopyroxene phenocrysts. **Very**  
365 **rare phenocrysts showing growth mantle textures at rim are reported. No evidence of resorption/dissolution**  
366 **textures are observed in studied samples.**

367 **The Cpx population, based on the integration of textural observations and mineral chemistry, (Fig. 6 a-f) can**  
368 **be classified** in five major categories: (i) **Cpx1 cluster is represented by homogeneous cores of all zoned**  
369 **phenocrysts in basalts; (ii) Cpx2 subpopulation is represented by homogeneous cores of all zoned**  
370 **phenocrysts from trachyandesites and trachytes; (iii) Cpx3 group represent both the unzoned phenocrysts in**  
371 **all studied samples and the rims (low-amplitude oscillatory, normal monotonous and normal step zoning) of**  
372 **cpx1 and cpx2 phenocrysts from all studied samples; (iv) Cpx4 population is constituted by microlites and**  
373 **microphenocrystals in groundmass from all analyzed samples; and (v) Cpx5 cluster collects together the**  
374 **emerald-green euhedral to subhedral microlites in groundmass of intra-caldera basalts (LH5-2, LH27-1) and**  
375 **rare normal monotonous zoning at outer rims of major clinopyroxene phenocrysts from few trachyandesites**  
376 **(LH15, LH17, LH26-2).**

377 The Cpx1 shows Mg# of 45-75, Ca 0.78-0.90 apfu, Q+J 1.84-1.94 and J/(J+Q) 0.03-0.06, and it can be classified  
378 as Ti-rich augite ( $\text{Wo}_{41-48}\text{En}_{25-42}\text{Fs}_{14-32}$ ).

379 The Cpx2 shows a Mg# of 59-84, Ca 0.20-0.92 apfu, Q+J 1.77-1.95 and J/(J+Q) 0.01-0.06, and it can be  
380 classified as diopside-rich augite ( $\text{Wo}_{11-48}\text{En}_{36-64}\text{Fs}_{9-32}$ ).

381 The Cpx3 shows Mg#: 20-86, Ca 0.27-0.97 apfu, Q+J 1.57-1.98 and J/(J+Q) 0.01-0.07, and it can be classified  
382 as diopside-rich augite ( $\text{Wo}_{12-49}\text{En}_{14-57}\text{Fs}_{8-62}$ ). **The composition of Cpx3 partially overlaps those of Cpx1 and**  
383 **Cpx2 groups, as it would be expected for phenocrysts with homogeneous cores (i.e. Cpx1 and Cpx2) and the**  
384 **respective low-amplitude oscillatory zoning or normal monotonous zoning rims (Cpx3) (e.g., Streck, 2008).**

385 The Cpx4 shows Mg# of 31-81, Ca 0.24-0.87 apfu, Q+J 1.87-1.97 and J/(J+Q) 0.01-0.06, corresponding to  
386 diopside-rich augite ( $\text{Wo}_{12-46}\text{En}_{18-60}\text{Fs}_{11-38}$ ). **The composition of Cpx4 partly overlaps that of Cpx3, however**  
387 **their textural characteristics are completely different.**

388 The Cpx5 differs from previous pyroxenes, with a large spread in Mg# ranging 5-73, Ca 0.03-0.83 apfu, Q+J  
389 1.51-2.07 and J/(J+Q) 0.07-0.89. The Cpx5 can be classified as Aegirine-Augite ( $\text{Na} < 0.3$  apfu,  $\text{XAeg} < 0.30$ ; with  
390  $\text{XAeg} = \text{Na}$  apfu if  $\text{Na} < \text{Fe}^{3+\text{Tot}}$ ,  $\text{XAeg} = \text{Fe}^{3+\text{Tot}}$  apfu if  $\text{Na} > \text{Fe}^{3+\text{Tot}}$ ) to Aegirines ( $\text{Na} = 0.68-0.88$  apfu,  $\text{XAeg} = 0.40-$   
391  $0.88$ ). Cpx5 clinopyroxenes are generally Ti-enriched ( $\text{TiO}_2$  up to 2.8 wt%, Ti up to 0.08 apfu) and straddle the  
392 Q+J=2 line defining the boundary for “normal” pyroxenes (Morimoto, 1989), thus indicating the presence of  
393 a  $\text{NaR}^{2+}_{0.5}\text{Ti}^{4+}_{0.5}\text{Si}_2\text{O}_6$  component (Morimoto, 1988, 1989; Huraiova et al., 2017) (Fig. 6c).

394 The compositional variation of clinopyroxenes can be summarized in the Na vs. Ti diagram (Fig. 6e-f).  
395 Interestingly, Augite-rich (Cpx1, Cpx2, Cpx3 and Cpx4) clinopyroxenes generally show positive correlation and  
396 linear distribution characterized by a progressive Ti- and Na-depletion, from Ti-Augite **cores (Cpx1)** in basalts  
397 to DiHd-rich Augite **(Cpx3, Cpx4) specimens in** trachytes. The Cpx5, belonging to Aegirine-Augite and Aegirine,  
398 moves away from this trend showing a negative correlation characterized by a progressive enrichment of Na  
399 content, with respect to a general Ti-depletion. Aegirine enrichment **could be** diagnostic of ferric iron (Fe<sup>3+</sup>)  
400 content increasing during the magmatic differentiation, whereas the diopside-hedenbergite enrichment  
401 testifies increasing of ferrous iron (Fe<sup>2+</sup>) in magma (e.g. Huraiova et al., 2017).

402

### 403 **6.3 Olivine**

404 Olivine is found in all analyzed samples, except for for LH27-2 trachyandesite and LH6 trachyte. It consists of  
405 idiomorphic (Fig. 4 a, c) to skeletal (e.g., Donaldson, 1974; Fowler et al., 2002; Faure et al., 2003; Welsch et  
406 al., 2013) (Fig. 4b) phenocrysts, and microlites in the groundmass (Fig. 4h). **Olivine crystals, both phenocrysts**  
407 **and microcrystals, show homogeneous cores with concordant normal monotonous zoning outer rims. In**  
408 **basalts, olivine** shows a continuous compositional range (Fig. 7a) from Fo<sub>86</sub>Fa<sub>14</sub>Mtc<sub>0</sub>Tep<sub>0</sub> (phenocryst in LH5-  
409 2 basalt) to Fo<sub>05</sub>Fa<sub>91</sub>Mtc<sub>1</sub>Tep<sub>3</sub> (groundmass microlites in LH27-1 basalt). Maximum MnO (up to 1.7 wt%)  
410 values are always found in Fe-rich olivine **microlites in basalts**. Low monticellite concentration (CaO always <  
411 1.0 wt%) in Los Humeros sample is typical for magmatic olivine (i.e., Melluso et al., 2014). CaO content  
412 positively correlates with the fayalite (FeO) compound (Fig. 5a). Together with the Mg#, the CaO content  
413 allows to discriminate olivine phenocrysts in three coherent compositional clusters: i) **olivine from basalts**,  
414 with Mg#= 79-87 and CaO= 0.21-0.73 wt%, ii) **olivine** from trachyandesites, with Mg#= 67-80 and CaO= 0.08-  
415 0.43 wt%, and iii) **olivine** from trachytes with Mg#= 58-63 and CaO= 0.16-0.42 wt%. A minor number of  
416 analyzed phenocrysts in basalts show **Cr<sub>2</sub>O<sub>3</sub> content in the range ca. 0.05-0.07 wt%. It is, instead, below**  
417 **detection limit for almost all analyzed olivine crystals in LHPCS lavas.** A minor cluster of **peridotite** Mg-olivine  
418 (Fo<sub>99</sub>Fa<sub>1</sub>) xenocrysts, characterized by disequilibrium textures (**resorption patterns**) at rim, have been  
419 identified in LH26-1 trachyandesite lava.

420

### 421 **6.4 Orthopyroxene**

422 Orthopyroxene occurs in most of the LHPCS trachyandesite (Fig. 4f) and trachyte samples (Fig. 4 g-h).  
423 **Orthopyroxene phenocrysts are generally unzoned with homogeneous textures. They** show intermediate  
424 (En<sub>41-83</sub>Fs<sub>14-55</sub>Wo<sub>2-10</sub>) compositions (Fig. 7b), with Mg# of 43-86, Al<sub>2</sub>O<sub>3</sub> up to 2.12 wt%, TiO<sub>2</sub> 0.08-1.33 wt%, and  
425 CaO 1.20-4.72 wt%. Similar compositions (En<sub>62-79</sub>Fs<sub>18-33</sub>Wo<sub>3-7</sub>) have been obtained for microlites in  
426 groundmass (Fig. 7b) with Mg# of 65-81, Al<sub>2</sub>O<sub>3</sub> 0.48-1.53 wt%, TiO<sub>2</sub> 0.21-0.60 wt% and CaO 1.35-3.49 wt%.  
427 In trachytes, orthopyroxene phenocrysts present Mg# ranging 59-65, with low Al<sub>2</sub>O<sub>3</sub> (0.18-0.73 wt%), low  
428 TiO<sub>2</sub> (0.11-0.32 wt%) and CaO (0.81-1.88 wt%), corresponding to Fe-rich composition (En<sub>56-63</sub>Fs<sub>34-39</sub>Wo<sub>2-4</sub>) with

429 a minor Ca-Cpx substitution (Fig. 7b). Orthopyroxene microlites in groundmass (Fig. 7b) show comparable  
430 hypersthene ( $\text{En}_{46-60}\text{Fs}_{35-45}\text{Wo}_{3-7}$ ) composition with Mg# of 50-63,  $\text{Al}_2\text{O}_3$  0.25-0.82 wt%,  $\text{TiO}_2$  0.19-0.31 wt%  
431 and CaO 1.32-3.27 wt%.

432 The compositional variation of orthopyroxene is summarized in  $\text{Al}^{\text{Tot}}$  vs. Mg# diagram (Fig. 7c). In general,  
433 orthopyroxene from trachyandesites is characterized by higher content of Al (apfu) and higher Mg#, whereas  
434 those from trachytes are richer in ferrous iron (lower Mg# values) and in manganese (Mn up to 0.04 apfu).

435

## 436 6.5 Spinel and Opaque Minerals

437 Basalts show a diversified set of opaque minerals. Phenocrysts are characterized by, in order of abundance,  
438 the presence of: i) Al-spinel ( $\text{TiO}_2$  0.58-1.00 wt%; Mg# 58-71; Cr# 21-30) (with  $[\text{Cr}\# = 100 \text{Cr}/(\text{Cr}+\text{Al})]$ ), ii) Ti-  
439 magnetite ( $\text{TiO}_2$  1.83-21.58 wt%; MgO 0.06-2.19 wt%; MnO 0.44-0.63 wt%) and ilmenite (MgO up to 2.18  
440 wt%). Groundmass is characterized by the only presence of Fe-Ti oxides (ca. 20-30  $\mu\text{m}$  in diameter; Fig. 4f) as  
441 ilmenite (MgO 0.27-1.50 wt%) and Ti-magnetite (MgO 0.18-1.89 wt%). Cr-spinels ( $\text{TiO}_2$  3.37-8.55 wt%; Mg#  
442 14-28; Cr# 62-72) are found just as inclusions, up to 200  $\mu\text{m}$  in diameter (Fig. 4a), in larger Mg-rich olivine  
443 phenocrysts.

444 Trachyandesites are characterized by phenocrysts of Ti-magnetite (MgO 0.07-3.84 wt%), ilmenite (MgO 1.11-  
445 4.79 wt%) and rare rutile (MgO 0.47 wt%). Groundmass crystals (ca. 20-30  $\mu\text{m}$  in diameter) show a  
446 comparable composition with Ti-magnetite (MgO 0.33-3.77 wt%), ilmenite (MgO 0.33-4.79 wt%) and rare  
447 rutile (MgO < 0.05 wt%). Comparable to basalts, Cr-spinels ( $\text{TiO}_2$  6.09-6.47 wt%; Mg# 19-21; Cr# 65-68) are  
448 identified only as inclusions (100-200  $\mu\text{m}$  in diameter) in major Mg-rich phenocrysts.

449 In Trachytes, Fe-Ti oxides show euhedral to subhedral habit and, based on chemistry, they are ilmenite (MgO  
450 2.06-3.31 wt%) and titanomagnetite (MgO 1.41-5.47 wt%). Phenocrystals (up to 50-100  $\mu\text{m}$  in diameter; Fig.  
451 4g) and groundmass (ca. 15-20  $\mu\text{m}$  in diameter) show same compositions.

452

## 453 7. MINERAL-LIQUID THERMOBAROMETRY

454 In order to define the thermo-baric (T-P) environmental conditions of the magmatic feeding system of the  
455 LHPCS, we integrate thermobarometry models based on olivine (Beattie, 1993; Putirka et al., 2007; Putirka,  
456 2008), orthopyroxene (Putirka, 2008), plagioclase (Putirka, 2005b; Putirka, 2008), alkali-feldspar (Putirka,  
457 2008) and clinopyroxene (Putirka et al., 1996, 2003; Putirka, 2008; Masotta et al., 2013) chemistry. Due to  
458 the paucity/absence of glasses, we assume the whole rock composition as representative of the original liquid  
459 (or nominal melt) in equilibrium with phenocrysts (Putirka, 1997, 2008; Mordick and Glazner, 2006; Aulinas  
460 et al., 2010; Dahren et al., 2012; Barker et al., 2015). We are aware that such a procedure put the focus on  
461 early steps of the crystallization history, characterized by high melt/crystal ratios. Relatively late melt  
462 compositions, related to the solidification of the groundmass, are not present or can simply not be analyzed.  
463 Thermobarometric calculations were developed after the application of mineral-melt equilibrium filters and

464 considering pre-eruptive  $H_2O^{liq}$  values calculated using the plagioclase-liquid hygrometer model (eq. 25b in  
465 Putirka, 2008). Plagioclase-liquid thermometry and barometry were calculated using eq. (24a) and eq. (25a),  
466 respectively, of Putirka (2008), mainly based on the Ca/Na distribution between melt and Pl. Alkali-feldspar-  
467 liquid thermometry was calculated considering the K-Na exchange, applying eq. (24b) in Putirka (2008).  
468 Olivine-liquid equilibrium thermometry was calculated integrating the models of Beattie (1993) and Herzberg  
469 and O'Hara (2002) with the thermometric eq. (2) in Putirka et al. (2007). Orthopyroxene-liquid thermometry  
470 was calculated by Fe-Mg partitioning following the model of Beattie (1993; in the revised form [eq. 28a] in  
471 Putirka, 2008). For barometry, based on the Na and Al content in Opx, the model of Wood (1974) in the  
472 revised form [eq. 29a] in Putirka (2008) was applied.

473 Clinopyroxene-liquid thermometry and barometry, for diopside-augite pyroxenes in basalts and  
474 trachyandesites (groups Cpx1, Cpx2, Cpx3, Cpx4), were calculated by the application of the Jd-DiHd exchange  
475 thermometer (Putirka et al, 1996, 2003) using [eq. 33] in Putirka (2008) and the Al-partitioning barometric  
476 model [eq. 32c] in Putirka (2008). Clinopyroxene-liquid thermometry and barometry, for diopside-augite  
477 pyroxenes in trachytes (groups Cpx3 and Cpx4), were calculated by the application of the Jd-DiHd exchange  
478 thermometer (Putirka et al, 1996, 2003; Putirka, 2008) recalibrated for alkaline differentiated magmas using  
479 [eqn. Talk33] and [Eqn. Palk 2012], respectively, in Masotta et al. (2013). Clinopyroxene-liquid thermometry  
480 and barometry, for augite-aegirine pyroxenes (Cpx5), were calculated integrating [eq. 33] and [eq. 32c] in  
481 Putirka (2008) with equations [Eqn. Talk2012] and [Eqn. Palk 2012] in Masotta et al. (2013). Results of  
482 mineral-melt equilibrium tests (Figs. 8, 9, 10), hygrometry calculations (Fig. 10) and geothermometric  
483 estimates are presented contextually in supplementary mineral chemistry tables. Summary of the  
484 thermobarometry estimates are reported in a Pressure-Temperature diagram (Fig. 11).

485

### 486 **7.1 Test for Mineral-Melt Equilibrium**

487 Prerequisite for the application of mineral-liquid thermobarometry models based on mineral-melt  
488 equilibrium conditions is to test and verify that mineral and the chosen liquid composition represent chemical  
489 equilibrium pairs (e.g., Putirka, 2008; Keiding and Sigmarsson, 2012). Petrographic investigations (i.e.,  
490 polarized light and BSE imaging) and calculation of mineral-liquid partition coefficients were integrated with  
491 the aim to select only mineral specimens showing equilibrium with the hosting melt (e.g., Putirka, 2008;  
492 Keiding and Sigmarsson, 2012).

493 The predominant euhedral to subhedral habit of crystals is generally considered as an evidence of equilibrium  
494 with the surrounding melt (e.g., Keiding and Sigmarsson, 2012). However, critical for mineral-liquid thermo-  
495 barometric model, it is the use of phenocrysts with strongly zoned textures (patchy-, sector-, reverse-, coarse  
496 banding oscillatory-zoning), or with disequilibrium textures (resorption patterns, dissolution surfaces,  
497 reaction rims and mineral mantles/clots) (e.g. Ginibre et al., 2002; Streck, 2008). These textures imply that  
498 core(s) and rim(s), or different portions of the same grain, crystallized and reacted in an evolving liquid with

499 progressively different compositions (e.g., Mordick and Glazner, 2006; Putirka, 2008; Keiding and Sigmarsson,  
500 2012). As defined by Streck (2008), when crystals are complexly zoned, it can be difficult to find criteria to be  
501 used for evaluation of crystal populations and their equilibrium with respective hosting melt. However, it is  
502 not the case of the studied samples, where phenocryst assemblages generally do not show disequilibrium  
503 patterns or complexly zoned textures (e.g., Ginibre et al., 2002; Streck, 2008). Moreover, all EMPA related to  
504 those rare crystals presenting morphological evidence of disequilibrium texture, such as patchy zoning, were  
505 discarded.

506 As second step, the mineral-liquid equilibria between liquid and previous selected minerals, were  
507 investigated using: (i) the Fe-Mg exchange coefficient, (ii) the An-Ab partitioning coefficient, and (iii) the  
508 comparison between observed and predicted normative components of minerals.

509 The partitioning of Fe-Mg between mineral and liquid is known as Fe-Mg exchange coefficient, or  $K_D^{min-liq}(Fe-Mg)$   
510 (defined as  $K_D^{min-liq}(Fe-Mg) = [MgO^{liq}FeO^{min}]/[MgO^{min}FeO^{liq}]$ , where *liq* is the liquid composition, *min* is  
511 the mineral composition and MgO and FeO are molar fractions; Roeder and Emslie, 1970; Langmuir and  
512 Hanson, 1981; Putirka, 2005a; Putirka, 2008). It is used here to test the equilibrium between mafic minerals  
513 (olivine, orthopyroxene and clinopyroxene) and liquid (e.g., MacLennan et al., 2001; Putirka, 2008; Stroncik  
514 et al., 2009; Aulinas et al., 2010; Keiding and Sigmarsson, 2012; Melluso et al., 2014; Feng and Zhu, 2018).

515 We calculated  $K_D^{min-liq}(Fe-Mg)$  values using (i) equation (17) in Putirka (2008) for Ol and Opx; (ii) temperature-  
516 dependent equation (35) in Putirka (2008) for diopsidic-augitic Cpx in basalts and trachyandesites; and (iii) the  
517 Na-corrected equation (35a) in Masotta et al. (2013) for Na-rich Cpx5 group and for all Cpx from LH5-1 and  
518 LH6-1 trachytes. The calculated  $K_D^{min-liq}(Fe-Mg)$  values for olivine and orthopyroxene are plotted in a Rhodes's  
519 diagram (Dungan et al., 1978; Rhodes et al., 1979; Putirka, 2005; Putirka, 2008) to graphically test the  
520 equilibrium between Ol (Fig. 8a) or Opx (Fig. 8b) and the melt (Liq). Furthermore, the Rhodes's diagram is  
521 useful to recognize: (i) presence of xenocrystals and/or antecrystals; (ii) late or groundmass crystallization;  
522 (iii) crystal removal (decrease of  $Mg\#^{liq}$  only); and (iv) closed system crystallization (decrease of  $Mg\#^{min}$  only)  
523 by deviations of the measured compositions from the expected ones (Rhodes et al., 1979; Putirka, 2008;  
524 Melluso et al., 2014).

525 The calculation of  $K_D^{cpx-liq}(Fe-Mg)$  does not consider variations of Ca and Al contents in Cpx (Rhodes et al.,  
526 1979; Putirka, 1999, 2005b, 2008). Therefore, a further equilibrium test was achieved through the  
527 comparison of analysed Cpx compositions (as expressed by the components EnFs, DiHd and Ca-Ts, where Ca-  
528 Ts stays for Ca-Tschermak) with component contents predicted from melt composition (e.g., Putirka, 2008;  
529 Mollo et al., 2010; Jeffery et al., 2013; Barker et al., 2015; Ellis et al., 2017). Normative components of Cpx  
530 were calculated following the scheme proposed in Putirka et al., (1996) and Putirka (2008); whereas  
531 calculation of Cpx components based on melt composition was performed using equations (eq 3.1a) for DiHd,  
532 (eq 3.2) for EnFs and (eq 3.4) for Ca-Ts in Putirka (1999). A graphical presentation (e.g., Jeffery et al., 2013;  
533 Barker et al., 2015) of this test is shown in Figure 9.



534 The partitioning of An-Ab between mineral and liquid is known as An-Ab exchange coefficient, or  $K_D^{pl-liq}(An-Ab)$   
535 (defined as  $K_D^{pl-liq}(An-Ab) = [XAb^{pl}XAlO_{1.5}^{liq}XCaO^{liq}]/[XAn^{pl}XNaO_{0.5}^{liq}XSiO_2^{liq}]$ , where *liq* is the liquid  
536 composition, *pl* is the plagioclase composition and all components are in molar fractions) (Carmichael et al.,  
537 1977; Holland and Powell, 1992; Putirka et al., 2007; Putirka, 2008; Lange et al., 2009; Keiding and  
538 Sigmarsson, 2012; Jeffery et al., 2013; Barker et al., 2015; Waters and Lange, 2015). Figure 10 presents a  
539 comparison of measured composition of plagioclase with the one calculated from the melt composition with  
540 the thermodynamic model eq (31) in Namur et al. (2012). A similar test can be applied for alkali-feldspars  
541 (Putirka, 2008).

542 In summary, we accept: (i) Ol with  $K_D^{ol-liq}(Fe-Mg) = 0.30 \pm 0.06$  (Roeder and Emslie, 1970; Putirka, 2005a;  
543 Putirka, 2008 and references therein) (Fig. 8a); (ii) Opx with  $K_D^{opx-liq}(Fe-Mg) = 0.29 \pm 0.06$  (Putirka, 2008 and  
544 references therein) (Fig. 8b); (iii) Cpx with  $K_D^{cpx-liq}(Fe-Mg) = 0.28 \pm 0.08$  (Putirka, 2008) and that verify the one-  
545 to-one ( $\pm 0.1$ ) relationship between predicted vs. observed normative components (EnFs, DiHd and Ca-Ts)  
546 for at least two of the monitored components (Fig. 9); (iv) Pl with  $K_D^{pl-liq}(An-Ab) = 0.27 \pm 0.11$  for  $T > 1050^\circ C$   
547 and  $K_D^{pl-liq}(An-Ab) = 0.10 \pm 0.05$  for  $T < 1050^\circ C$  (Putirka, 2008) or that fall within  $\pm 0.1$  of the one-to-one  
548 relationship between predicted vs observed An components (Fig. 10); and (v) Afs with  $K_D^{afs-liq}(An-Ab) = 0.27 \pm$   
549  $0.18$  (Putirka, 2008). All mineral-liquid pairs exceeding the accepted exchange coefficient values for Ol, Cpx,  
550 Opx and Fsp were discarded for thermobarometric analyses.

551

## 552 7.2 Pre-eruptive $H_2O^{liq}$ content estimates

553 Thermobarometric models for volcanic system require an initial estimate of the pre-eruptive water  
554 concentration (wt%) in melt ( $H_2O^{liq}$ ), which was determined in this work by using the plagioclase-liquid  
555 hygrometer model [eq. 25b] in Putirka (2008). Hygrometry calculations were produced after the application  
556 of plagioclase-liquid equilibrium filters. The calculated pre-eruptive  $H_2O^{liq}$  wt% values ( $\pm 1\sigma$  standard  
557 deviation of the weighted mean) are plotted as isolines in Fig. 10. The hygrometer of Putirka (2008) indicates  
558 (Fig. 10): (i)  $H_2O^{liq}$  negative values in basalts, from -0.20 to -0.40 wt%, with a weighted mean of  $-0.37 \pm 0.20$   
559 wt% (MSWD= 0.0026; n= 95); (ii) trachyandesites pre-eruptive water content in the range  $H_2O^{liq}$ : 0 – 1.40  
560 wt% (weighted mean of  $0.57 \pm 0.12$  wt%, MSWD= 0.12, n= 246); and (iii) trachytes with the highest water  
561 concentration ( $H_2O^{liq}$ : 1.40 – 1.90 wt%; weighted mean of  $1.46 \pm 0.32$  wt%, MSWD= 0.059, n= 37). Following  
562 the approach of Keiding and Sigmarsson (2012), negative values in basalts are interpreted as anhydrous melt  
563 compositions. Coherently with the existing literature (e.g., Webster et al., 1999), the anhydrous character is  
564 then assumed as a  $H_2O^{liq} < 1\text{wt\%}$  content.

565 Application of plagioclase-liquid hygrometer model (Putirka, 2008) define anhydrous environment for  
566 pressure-temperature calculations in basalts. Whereas hydrous conditions are required for evolved LHPCS  
567 melts and in particular for trachytic lavas, where the impact of 1 wt%  $H_2O$  is expected to generate a

568 temperature decrease of ca. -40 °C and a pressure increase of ca. + 1.0 kbar in geothermometers and  
569 geobarometers, respectively (Putirka, 2008; Keiding and Sigmarrsson, 2012).

570 On contrary, existing studies (e.g., Kushiro, 1969; Sisson and Grove, 1993; Yang et al., 1996; Putirka, 2005a,  
571 2005b, 2008; Kelley and Barton, 2008; Keiding and Sigmarrsson, 2012) demonstrated a negligible effect of  
572 water for basaltic and intermediate melts with H<sub>2</sub>O<sup>liq</sup> 0 – 1 wt%.

573

### 574 **7.3 Thermobarometry Results**

#### 575 **7.3.1 Basalts**

576 When applied to phenocryst cores, the Pl-liq thermobarometry (Fig. 11a-c) show that all basaltic materials  
577 have magmatic anhydrous T in the range 1230-1266 °C (weighted mean of 1250 ± 5 °C, ±1σ standard  
578 deviation of the weighted mean, MSWD= 0.112, n= 95). Pressure estimates are in the range 6.5-8.7 kbar  
579 (weighted mean of 7.9 ± 1.1 kbar, ±1σ standard deviation of the weighted mean, MSWD= 0.024, n= 28) for  
580 LH18 Ol-basalts, and 7.2-10.3 kbar (weighted mean of 9.2 ± 0.7 kbar (±1σ), MSWD= 0.064, n= 67) for LH5.2  
581 and LH27.1 Ol-Cpx-basalt. Olivine-melt equilibrium (Fig. 11a-c), for the olivine compositional range of Fo 80-  
582 85%, yields T window of 1240-1297 ± 27 °C (±1σ), consistent with the results obtained with Pl-liq  
583 thermometry. The Cpx-thermobarometry (Fig. 11a, c), for both Cpx1 (phenocryst cores) and Cpx3  
584 (phenocryst rims and unzoned phenocrysts), provides temperature of 1006-1209 °C (weighted mean of 1124  
585 ± 12 °C (±1σ), MSWD= 3.4, n= 82). , for P in the range 3.1-11.5 kbar (weighted mean of 7.6 ± 0.8 kbar (±1σ),  
586 MSWD= 2.7, n= 36) for Cpx1, and 2.5-7.7 kbar (weighted mean of 4.0 ± 0.8 kbar (±1σ), MSWD= 0.63, n= 14)  
587 for Cpx3. Thermobaric estimates for Cpx4 (microlites in groundmass) indicate shallow conditions (0.3 – 3.0;  
588 weighted mean of 1.6 ± 1.2 kbar (±1σ), MSWD= 0.38, n= 6) for temperatures (1006-1123 °C; weighted mean  
589 of 1060 ± 54 °C (±1σ), MSWD= 2.9, n= 6) comparable to those obtained for Cpx1 and Cpx3. Higher  
590 temperature estimates (1067-1221 °C; weighted mean of 1157 ± 53 °C (±1σ), MSWD= 2.4, n= 7) at low-  
591 pressure (0.4-4.7; weighted mean of 2.9 ± 1.1 kbar (±1σ), MSWD= 0.83, n= 7) are instead obtained for a  
592 limited number of Cpx5 (aegirine-rich) compositions (Fig. 11a, c).

593

#### 594 **7.3.2 Trachyandesites**

595 Based on the Opx- presence/absence criterion, two populations of trachyandesites have been discriminated  
596 in this study.

597 Opx-free trachyandesites LH15 and LH21-2 (El Limón and Sarabia lava flows, respectively) are characterized  
598 by i) plagioclase phenocryst cores crystallized at T of 1190-1263 °C (weighted mean of 1248 ± 7 °C (±1σ),  
599 MSWD= 1.09, n= 39) and P of 4.8-9.4 kbar (weighted mean of 7.7 ± 0.9 kbar (±1σ), MSWD= 0.14, n= 39); ii)  
600 comparable temperature (1193-1263 °C; weighted mean of 1227 ± 37 °C (±1σ), MSWD= 2.3, n= 6) and  
601 pressure (6.7-9.6 kbar, mean value of 7.8 ± 2.4 kbar (±1σ), MSWD= 0.101, n= 6) obtained for rare phenocryst  
602 rims and microlites at equilibrium; iii) olivine-melt equilibrium (with Fo: 75-80%) showing a T window of 1030-

603 1055 ± 27 °C (±1σ); iv) rare Cpx2 (clinopyroxene phenocryst cores) showing equilibrium with melt and yielding  
604 T 1061-1239 °C (weighted mean of 1116 ± 29 °C (±1σ), MSWD= 2.3, n= 12) and P ca. 2.9 -8.3 kbar (weighted  
605 mean of 5.2 ± 1.2 kbar (±1σ), MSWD= 1.5, n= 12); v) Cpx3 (rims of and unzoned phenocrysts) showing  
606 equilibrium with melt and yielding thermobarometric results (T 938-1139 °C, with weighted mean of 1074 ±  
607 15 °C (±1σ), MSWD= 1.9, n= 32; and P 1.0-4.4 kbar with weighted mean of 2.8 ± 0.5 kbar (±1σ), MSWD= 0.22,  
608 n= 32); vi) Cpx4 (groundmass microcrystals) compositions indicating, with respect to Cpx3, comparable  
609 temperatures (1026-1127 °C, with weighted mean of 1059 ± 16 °C (±1σ), MSWD= 0.71, n= 14) at lower  
610 pressure conditions (0.3 – 3.6 kbar with weighted mean of 1.4 ± 0.8 kbar (±1σ), MSWD= 0.35, n= 14). The  
611 unique Cpx5-liquid pair at equilibrium yielded P-T conditions of 5.6 ± 1.5 kbar and 1122 ± 30 °C.  
612 Thermobarometric estimates (Fig. 11a, d) for Opx-bearing trachyandesites (LH4, LH13, LH17; LH26-1; LH26-  
613 2; LH27-2) show overlapping P-T conditions for plagioclase populations with: i) phenocryst cores crystallizing  
614 at T: 1145-1228 °C (weighted mean of 1187 ± 4 °C (±1σ), MSWD= 1.17, n= 166) and P: 4.1-7.7 kbar (weighted  
615 mean of 5.8 ± 0.5 kbar (±1σ), MSWD= 0.059, n= 166), and ii) phenocryst rims and microcrystals forming at T:  
616 1140-1224 °C (weighted mean of 1168 ± 8 °C (±1σ), MSWD= 0.90, n= 35) and P: 4.4-8.5 kbar (weighted mean  
617 of 6.4 ± 1.0 kbar (±1σ), MSWD= 0.14, n= 35). Lower temperatures (1050-1090 ± 27 °C (±1σ)) are obtained  
618 using olivine (Fo 70-80%) – liquid equilibrium model.  
619 Thermobarometers applied to pyroxenes indicate: i) Cpx2 (phenocryst cores) crystallizing at T: 979-1204 °C  
620 (weighted mean of 1060 ± 8 °C (±1σ), MSWD= 1.7, n= 106) and P: 3.4 -11.65 kbar (weighted mean of 7.0 ±  
621 0.3 kbar (±1σ), MSWD= 0.91, n= 106), ii) Cpx3 crystallizing at T: 958-1106 °C (weighted mean of 1026 ± 6 °C  
622 (±1σ), MSWD= 1.3, n= 147) and P: 1.2 -6.9 kbar (weighted mean of 4.3 ± 0.2 kbar (±1σ), MSWD= 0.72, n=  
623 147), iii) rare Cpx4 showing general equilibrium with melt and forming at P-T conditions of : 920-1123 °C  
624 (weighted mean of 1020 ± 21 °C (±1σ), MSWD= 2.7, n= 24) and P: 0.1-3.4 kbar (weighted mean of 1.8 ± 0.6  
625 kbar (±1σ), MSWD= 0.56, n= 24), and iv) Opx yielding crystallization conditions, for both phenocrysts and  
626 microlites, of T 1048-1123 °C (weighted mean of 1078 ± 5 °C (±1σ), MSWD= 0.24, n= 129) and P: 0 -2.8 kbar  
627 (weighted mean of 1.1 ± 0.6 kbar (±1σ), MSWD= 0.057, n= 84). In all trachyandesites samples, temperatures  
628 obtained through Ol-Liq model and Cpx-Liq model are comparable (Fig. 11a, d), whereas the Pl-Liq model  
629 shows higher T values. These can be interpreted as an earlier plagioclase crystallization with respect to the  
630 olivine and clinopyroxene. Orthopyroxene (Opx) can be considered a tracer of trachyandesitic magma  
631 stagnations at shallow depth since the invariably lower pressure values obtained by Opx-liquid barometer.

### 632 633 **7.3.3 Trachytes**

634 Magmatic P-T conditions (Fig. 11a, e) of trachytes (LH5.1 and LH6) melts are defined by: i) plagioclase  
635 crystallization at T: 1050-1094 °C (weighted mean of 1069 ± 6 °C (±1σ), MSWD= 0.39, n= 37) and P: 4.7-9.0  
636 kbar (weighted mean of 6.5 ± 1.0 kbar (±1σ), MSWD= 0.20, n= 37), ii) olivine (Fo55-65%) – liquid regression

637 indicating olivine crystallization at  $900-920 \pm 27 \text{ }^\circ\text{C}$  ( $\pm 1\sigma$ ), iii) clinopyroxenes crystallization, both phenocrysts  
638 (Cpx3) and groundmass(Cpx4), at temperature of ca.  $955 \text{ }^\circ\text{C}$  (weighted mean of  $956 \pm 14 \text{ }^\circ\text{C}$  ( $\pm 1\sigma$ ), MSWD=  
639 0.00056, n= 17) and very shallow-depth conditions (P weighted means of  $2.3 \pm 0.9 \text{ kbar}$  ( $\pm 1\sigma$ ), MSWD=  
640 0.047, n= 10 and  $1.6 \pm 1.1 \text{ kbar}$  ( $\pm 1\sigma$ ), MSWD= 0.04, n= 7; for Cpx3 and Cpx4, respectively). Shallow-depth  
641 conditions are obtained also for orthopyroxene crystallization with temperature in the range  $960-1006 \text{ }^\circ\text{C}$   
642 (weighted mean of  $990 \pm 7 \text{ }^\circ\text{C}$  ( $\pm 1\sigma$ ), MSWD= 0.28, n= 49) and P:  $0.2-3.6 \text{ kbar}$  (weighted mean of  $1.6 \pm 0.9$   
643  $\text{ kbar}$  ( $\pm 1\sigma$ ), MSWD= 0.101, n= 35). Alkali-feldspar-liquid thermometer provided temperature estimates  
644 always  $<500^\circ\text{C}$ , here interpreted as feldspar re-equilibration of groundmass after eruption in  
645 subsolvus/subsolidus conditions (Nekvasil, 1992; Brown and Parsons, 1994; Plumper and Putnis, 2009;  
646 Kontonikas-Charos et al., 2017; Latutrie et al., 2017). Interestingly, temperatures obtained through Pl-Liq  
647 model are higher than those obtained with Ol-Liq, Cpx-Liq and Opx-Liq, suggesting an earlier crystallization  
648 of plagioclase with respect to mafic minerals. Moreover, the Pl-Liq models indicate thermobaric estimates  
649 comparable to those obtained for trachyandesitic rocks.  
650  
651

## 652 8. DISCUSSION

### 653 8.1 Major-elements mass balance modeling

654 Based on the textural evidence documenting: (i) cpx-bearing basalts being mainly characterized by euhedral  
655 olivine and plagioclase and subhedral-anhedral clinopyroxene, indicating crystallization of olivine and  
656 plagioclase prior to clinopyroxene (e.g., Bindeman and Bailey, 1999); and (ii) all LHPCS volcanic rocks do not  
657 show disequilibrium textures (such as fine-sieve textures, resorption surface, crystal clots, disequilibrium  
658 growth-mantel, reverse zoning, reaction-rims, breakdown mantle and dissolution; e.g., Streck, 2008) typical  
659 of AFC-mixing processes, we suggest that the studied LHPCS volcanic rocks represent cogenetic melts,  
660 belonging to the same line of descent, excluding major mass-change due to assimilation and mixing (AFC-  
661 mixing) processes. In order to test this hypothesis, we applied fractional crystallization (FC) modelling (e.g.,  
662 White et al., 2009; Moghadam et al., 2016; Lucci et al., 2016) to test and demonstrate the hypothesis the  
663 LHPCS volcanic rocks belong to a unique line of descent. The FC-modeling is focused on these hypotheses: (i)  
664 direct cogenetic relationship between all LHPCS basalts, and (ii) common genesis for all LHPCS  
665 trachyandesites and trachytes through differentiation via fractional crystallization starting from the same  
666 basaltic parental melt.

667 Major-element mass balance models (e.g., Bryan et al., 1969) can be used to test and define relative  
668 proportion of phases involved in Rayleigh fractional crystallization (RFC, Daughter = Parent - fractionating  
669 assemblage) and crystal accumulation (Cumulate = Melt + accumulated assemblage) hypotheses (e.g., White  
670 et al., 2009; Moghadam et al., 2016; Lucci et al., 2016).

671 If Parent melt (for RFC) or Cumulate (for crystal accumulation) compositions are assumed as matrix **b**, and  
672 the FC-model is solved for **b**, then **b** = Liquid (Daughter or Melt) + Minerals (fractionating or accumulated  
673 assemblage). If compositions of Liquid and Minerals are known (matrix **A**), it is possible to estimate, by least  
674 squares approximation, their proportion (in matrix **c**). The similarity of **b'** (matrix **c** multiplied with matrix **A**)  
675 to **b** (real value) is quantified with the sum of the square of the residuals ( $\Sigma r^2$ ) as:

$$676 \Sigma r^2 = \sum_{i=1}^n (b'_i - b_i)^2 \quad (\text{Eq. 1})$$

677 RFC and Cumulate model results are considered acceptable when  $\Sigma r^2 < 1.0$ . Proportion of Liquid (Daughter  
678 or Melt) is expressed with **F** in matrix **c**.

679 Major-element mass balance models are calculated in the system SiO<sub>2</sub>-TiO<sub>2</sub>-Al<sub>2</sub>O<sub>3</sub>-FeO\*-MnO-MgO-CaO-  
680 Na<sub>2</sub>O-K<sub>2</sub>O. The LH5-2 cpx-bearing basalt, with the lowest SiO<sub>2</sub> and the highest MgO contents, was selected  
681 as possible source for all pyroxene-bearing trachyandesites and trachytes. The fractional crystallization  
682 hypothesis is then tested for all the LHPCS studied rocks and, considering the magmatic mineralogy made of  
683 An-rich plagioclase, Ti-rich clinopyroxene, Mg-rich olivine, Spinel. The same mineral assemblage was used to  
684 verify the cogenetic relationship between studied LHPCS basalts through progressive crystal accumulation.  
685 All calculations were managed with Microsoft Office Excel2019, results of FC-models are presented in  
686 Supplementary Table 6.

687 The RFC model has been applied to all studied trachyandesites and trachytes. It was verified that a  
688 fractionation of the Pl+Cpx+Ol+Sp assemblage in the range of: (i) 45-63 wt% ( $\Sigma r_2$  0.37-0.92) is necessary to  
689 produce Opx-free trachyandesites, (ii) 59-69 wt% ( $\Sigma r_2$  0.38-0.92) is capable to produce Opx-bearing  
690 trachyandesites, and (iii) 73-74 wt% ( $\Sigma r_2$  0.88-0.91) is requested to produce trachytes. The crystal  
691 accumulation has been tested to verify the linkage between Cpx-free basalt (LH18-1) and cpx-bearing basalts  
692 (LH5-2, LH27-1). It was verified that a crystal accumulation of the Pl+Cpx+Ol+Sp assemblage in the range of  
693 16-17 wt% ( $\Sigma r_2$  0.05-0.15), with Cpx in the range 5-7 wt%, is able to produce LHPCS cpx-bearing basalts.  
694 The results obtained from FC-models indicate that the LHPCS volcanic rocks are genetically linked melts, due  
695 to crystal accumulation (basalt) and fractional crystallization (intermediate and felsic rocks) of a  
696 Pl+Cpx+Ol+Sp mineral assemblage. Trachyandesites and trachytes represent different degrees of  
697 fractionation (RFC values in the range 45-74%) starting from a cpx-bearing basaltic source. Cpx-bearing  
698 basalts are interpreted as resulting from crystallization and accumulation of cpx, together with Pl+Ol+Sp, in  
699 a pristine cpx-free basaltic melt. Results from FC-models also confirm the possibility to produce hydrous felsic  
700 melts starting from a nominal anhydrous ( $H_2O < 1$  wt%; e.g., Webster et al., 1999) mafic parental melt.  
701 Integrating FC-model and hygrometer (Putirka, 2008) results, LHPCS trachytes show  $H_2O$  ca. 1.4-2.0 wt% and  
702 represent the ca. 25 wt% fractionated residual melt from a parental basaltic source characterized by  $H_2O$  in  
703 the range 0.3-0.5 wt%.

704

## 705 **8.2 Magma evolution beneath Los Humeros**

706 The conceptual model of the present-day LHPCS magmatic plumbing system beneath the Los Humeros  
707 caldera is presented in Fig. 12. Based on textural observations, mineral chemistry and thermobaric estimates  
708 the early HT (1230-1270 °C) stage of LHPCS magma evolution is represented by high-anorthite plagioclase  
709 phenocrysts and Mg-rich olivine ( $X_{Fo} = 80-85\%$ ) crystallizing in the deep (ca. 8 kbar) basaltic reservoir. Where  
710 these magmas erupted directly, they formed **Cpx-free Ol-basalt** lava flows such as Texcal Lava flow (LH18).  
711 This scenario, **for LH18 basalt sample**, is confirmed by (i) **olivine and plagioclase with homogeneous cores**  
712 **and normal monotonous zoning textures at rims**, indicating a fast growth during ascent of magma (e.g.,  
713 **Streck, 2008**); (ii) olivine with spinifex, dendritic and skeletal textures, interpreted as supercooling mineral  
714 texture largely resulting from rapid olivine-supersaturated magma rise from deeper level during the eruption  
715 (e.g., Donaldson, 1974; Nakagawa et al., 1998; Fowler et al., 2002; Dahren et al., 2012; Welsch et al., 2013),  
716 **and (iii) plagioclase specimens with swallow-tailed crystal morphology**, interpreted as rapid plagioclase  
717 **growth due to undercooling related to eruption process** (e.g., Renjith, 2014).

718 A permanence of these basaltic melts in the deep reservoir together with a temperature decrease of ca.  
719 100°C can lead to clinopyroxene appearance/crystallization in the system (e.g., Groove, 2000) and its  
720 progressive accumulation in the phenocryst assemblage. This hypothesis is supported by Cpx-Liq  
721 thermometry models for Cpx1 (Ti-rich augites in basalts) indicating Cpx appearance at ca. 7-8 Kbar and 1150

722 °C (mean values), and by FC-models indicating a Pl+Cpx+Ol+Sp crystal accumulation up to 15-17 wt% in the  
723 pristine basaltic melt to produce the Cpx-bearing basalts.

724 Where these magmas erupted as intra-caldera basalts (LH5-2, LH27-1), they are characterized by the further  
725 crystallization of (i) progressively Fe-rich olivine (up to X<sub>Fo</sub>= 17-20%), (ii) Ab-rich plagioclase (X<sub>An</sub>= 25-30%),  
726 (iii) Cpx<sub>3</sub> unzoned homogeneous phenocrysts and overgrowth (normal monotonous and normal low-  
727 amplitude oscillatory zoning) on Cpx<sub>1</sub>-cores, (iv) Cpx<sub>5</sub> (Aeg-Aug) Na-clinopyroxenes and (v) Cpx<sub>4</sub> (Di-rich)  
728 microcrystals and microlites. This mineral assemblage (mineral chemistry and textures) together with the  
729 thermobarometric results obtained, describes a near-isothermal magma uprising within a narrow  
730 temperature window of ca. 1070-1150 °C. Such crystal-bearing magmas ascend from the deeper reservoir to  
731 intermediates and shallower stagnation levels, where different phases would crystallize, before the eruption  
732 (e.g., Feng and Zhu, 2018). In particular, (i) the homogeneous unzoned cores of phenocrysts represent the  
733 early crystallization at equilibrium with the melt, (ii) the normal low-amplitude oscillatory zoning from Pl and  
734 Cpx phenocrysts indicates a kinetically driven crystallization (e.g., Ginibre et al., 2002; Streck, 2008; Renjith,  
735 2014), whereas the normal monotonous zoning observed in many Pl, Cpx and Ol phenocrysts indicates a fast  
736 growth during ascent of the magma (e.g., Streck, 2008); (iii) microlites formation indicates water exsolution  
737 driven crystallization (e.g., Rutherford, 2008; Renjith, 2014) during a relative rapid ascent or eruption  
738 processes (e.g. Renjith, 2014); and (iv) the similarity of compositions between Pl and Cpx phenocrysts rims  
739 and microlites confirms that there were essentially no major changes in the temperature of any of these  
740 basaltic magmas during the ascent (e.g., Rutherford, 2008). The scenario of rapid ascent of LHPCS basaltic  
741 magmas is supported also by the observed high-vesicularity textures, interpreted as bubble-growth  
742 processes during a relative fast magma rise precluding exsolved volatile to escape (e.g. Sparks, 1978; Sparks  
743 et al., 1998; Rutherford and Gardner, 2000; Rutherford, 2008; Costa et al., 2013; Feng and Zhu, 2018).

744 Fractional crystallization of An-rich plagioclase, Fo-rich olivine, Ti-rich augite and spinel (Pl+Ol+Cpx+Sp in RFC-  
745 models) in the primary cpx-bearing basaltic magmas produces residual melts (ca. 30-55 wt%) of  
746 trachyandesitic compositions. These evolved buoyant melts will be prone to leave the basaltic reservoir to  
747 produce shallower intrusions in a vertically extensive magmatic system (e.g., Jackson et al., 2018), carrying  
748 early-formed phenocrysts (i.e., anorthitic plagioclase antecrystals) to the intermediate reservoir and stall.  
749 Within this intermediate vertically-distributed layered storage system in the middle crust, Cpx<sub>2</sub>  
750 clinopyroxene and all the rest of plagioclase phenocrysts start to crystallize producing progressively evolved  
751 felsic residual melts able to migrate upward in the feeding system or erupt (e.g., Freundt and Schminke, 1995;  
752 Patané et al., 2003; Klugel et al., 2005; Stroncik et al., 2009; Aulinas et al., 2010; Dahren et al., 2012; Keiding  
753 and Sigmarsson, 2012; Scott et al., 2012; Jeffery et al., 2013; Coombs and Gardner, 2001; Barker et al., 2015;  
754 Feng and Zhu, 2018). Similarly to LHPCS basalts, the phenocryst morphologies and textures, together with  
755 the microlites compositions and the vesicle-rich textures decived in trachyandesitic melts suggests a nearly

756 isothermal rapid ascent precluding exsolved volatiles to escape and producing water exsolution driven  
757 crystallization (e.g., Rutherford, 2008; Renjith, 2014).

758 The shallowest magma stagnation level (< 3kbar; mean 1.5 kbar) has been here interpreted as a complex  
759 magma plexus constituted by a system of small magma volumes, distributed in locally interconnected pockets  
760 and batches where (i) mafic and intermediate magmas shortly stall prior to erupt and (ii) more evolved melts  
761 reside for a relatively longer time, enough to crystallize orthopyroxene and to enabling the escape of part of  
762 the exsolved volatiles (e.g., Sparks et al., 1998; Feng and Zhu, 2018; Clarke et al., 2007), as suggested by  
763 phenocryst textures and compositions and by poor-vesicle textures observed in Opx-trachyte samples (LH5-  
764 1, LH6-1).

765 Compositional reverse zoning associated with disequilibrium textures and dissolution/resorption patterns in  
766 phenocrysts, are widely considered indicators of both magma-replenishment or assimilation processes (e.g.,  
767 Wright and Fiske, 1972; Duda and Schminkcke, 1985; Clague et al., 1995; Yang et al., 1999; Klugel et al., 2000;  
768 Zhu and Ogasawara, 2004; Stroncik et al., 2009; Ubide et al., 2014; Viccaro et al., 2015; Gernon et al., 2016;  
769 Feng and Zhu, 2018). In the case of Los Humeros, almost all investigated LHPCS samples, from basalts to  
770 trachytes, contain mainly phenocrysts with homogeneous cores and low-amplitude oscillatory or normal  
771 monotonous zoned rims (Pl+Ol+Cpx) or unzoned homogeneous phenocrysts (as in case of Cpx<sub>3</sub> and Opx).  
772 Rare specimens not suitable for mineral-liquid thermobarometry such as plagioclase and clinopyroxene with  
773 patchy cores or olivine xenocrysts are reported. The general absence of disequilibrium textures and patterns  
774 in LHPCS studied samples, is therefore interpreted as a lack of evidence of major mixing/recharge and/or  
775 assimilation processes acting in the plumbing system (e.g., Cashman et al., 2017 and references therein). This  
776 hypothesis is in line with the results obtained from tests for mineral-melt equilibria. Rhodes's diagram  
777 (Rhodes et al., 1979; Putirka, 2008) for olivine compositions (Fig. 8a) highlights a progressive decrease in  
778 Mg<sup>#liq</sup> from basalts to trachytes coupled with general absence of xenocrysts/antecrystals cargo. This  
779 behavior is compatible with a complete removal from the melt of previously crystallized Mg-olivine (Roeder  
780 and Emslie, 1970; Dungan et al., 1978; Rhodes et al., 1979; Putirka, 2008; Melluso et al., 2014). All melts  
781 (from basalts to trachytes) show invariably suites of olivines with maximum forsterite (Fo) contents in  
782 equilibrium with the respective whole rocks, and vertical trends consistent with closed-system melt  
783 differentiation (Roeder and Emslie, 1970; Rhodes et al., 1979; Putirka, 2008; Melluso et al., 2014). Similar  
784 behavior is obtained for orthopyroxene (Fig. 8b), where again Rhodes's test highlights (i) absence of  
785 antecrystals, and (ii) Opx-suites progressively and normally Fe-enriched from trachyandesites to trachytes.  
786 The absence of clinopyroxene clots and overgrowth mantle textures on orthopyroxene crystals, again  
787 excludes the occurrence of magma mixing/recharge processes (Laumonier et al., 2014; Neave et al., 2014;  
788 Zhang et al., 2015; Feng and Zhu, 2018). Such interpretation is supported also by field observations, where  
789 the interbedded basaltic andesite and trachydacite fall deposits of the ca. 7 ka Cuicuiltic Member show no  
790 evidence of magma-mixing (Dávila-Harris and Carrasco-Núñez, 2014).



791 An-Ab partition coefficients (e.g., Putirka, 2008; Jeffery et al., 2013) show a comparable scenario (Fig. 10) in  
792 which: (i) basalts are characterized by suites of plagioclases with maximum anorthite (An) contents in  
793 equilibrium with the respective whole rocks, and progressive  $An^{Pl}$  decrease consistent with closed-system  
794 differentiation; and (ii) progressive decrease in predicted  $An^{liq}$  from basalt to trachyte compatible with  
795 evolved melts **differentiation via fractional crystallization**. Intermediate and evolved products are  
796 characterized by plagioclase phenocrysts characterized by An-rich homogeneous cores (An 70-85%), **with**  
797 **compositions comparable to those of basalts**. These An-rich cores can be crystallized in two possible  
798 **scenarios**. The first one is related to the H<sub>2</sub>O content in magma. Increasing the water content in melt strongly  
799 **favors crystallization of An-richer plagioclase**. A water content rise from 0.5 to 2.0 wt% could lead to an  
800 **increase of the An component up to 6-8 mol% (Bindeman and Bailey, 1999; Sano e Yamashita, 2004; Ushioda**  
801 **et al., 2014)**. In this view, the An-rich plagioclase in intermediate and felsic rocks can be interpreted as the  
802 **response to the increasing water-content in the fractionated melt**. The second scenario implies that An-rich  
803 **plagioclase taps a more primitive stage of basalt segregations**. Since plagioclase phenocrystals with An in the  
804 **range 65-81% are commonly found in LHPCS basalts, the An-rich plagioclase cores in trachyandesites and**  
805 **trachytes could represent either antecrysts derived from crystallization of early sills in the magmatic reservoir**  
806 **system (sensu Jackson et al., 2018) or crystallization products in an earlier stage of the trachyandesite and**  
807 **trachyte segregation from the basaltic reservoir (e.g., Bindeman and Bailey, 1999; Kinman and Neal, 2006)**.  
808 **We suggest that both scenarios concurred to the genesis of An-rich phenocrysts in trachyandesites and**  
809 **trachytes**. Noteworthy, when An-rich plagioclase crystals are found (in mafic and intermediate rocks with  
810 **Pl+Ol+Cpx assemblages**), it implies that no significant clinopyroxene crystallization has occurred prior to the  
811 **anorthitic plagioclase (Bindman and Bailey, 1999)**.  
812 **With respect to plagioclase, a similar behavior is observed also for clinopyroxene and in particular for Cpx1**  
813 **and Cpx2 (clinopyroxene cores in basalts and in trachyandesites+trachytes, respectively) populations**. Since  
814 these mineral cores (Pl, Cpx1 and Cpx2) generally present normal growth rims (i.e., Ab-rich Pl and Cpx3), we  
815 suggest that stagnation levels at both intermediate and shallower depths underwent crystallization in a  
816 closed system. Otherwise, features such as: i) diffused reverse zoning, ii) high-temperature crystal-clots,  
817 mantling and overgrowth, iii) disequilibrium and dissolution textures (e.g., Stroncik et al., 2009; Cashman et  
818 al., 2017; Feng and Zhu, 2018 and references therein), should be widely observed, but this is not the case in  
819 the LHPCS studied lavas.

820

### 821 **8.3 The magma plumbing system**

822 The petrological archive constituted by LHPCS lavas, spanning from **transitional- and alkali-basalts** to  
823 trachytes, describes the Holocene activity of Los Humeros volcanic complex. **Major element bulk**  
824 **compositions of LHPCS lavas are characterized, in selected Harker diagrams (Fig. 3 b-d) by linear trends**  
825 **comparable to those expected for cogenetic melts (e.g., Giordano et al., 2012)**. Major-element FC-modeling

826 confirms the hypothesis of a common genesis for LHPCS volcanic rocks through crystal  
827 fractionation/accumulation processes of the same mineral assemblage (Pl+Cpx+Ol+Sp). Furthermore,  
828 textural observations and results from FC-models permit to exclude at this stage mass-change or mass-  
829 addition phenomena driven by AFC-Mixing processes.

830 Results obtained from the application of different and independent thermobarometry models (Fig. 11)  
831 confirm the working hypothesis of a complex magmatic plumbing system rather than a single “standard”  
832 magma chamber (e.g., Keiding and Sigmarsson, 2012; Cashman and Giordano, 2014; Cashman et al., 2017;  
833 Feng and Zhu, 2018) developed beneath the active Los Humeros caldera and feeding the LHPCS volcanism.  
834 With the aim to propose an updated and realistic conceptual model of the present-day main storage zones  
835 and magma plumbing system within the crust below Los Humeros caldera, we integrate pressure-  
836 temperature estimates acquired in this work, with the existing data related to crustal structure and  
837 properties of the study area. The resulted model is shown in Figure 12.

838 The density of TMVB crust shows a large range between 1800 Kg/m<sup>3</sup> for unconsolidated sediments to about  
839 3000 kg/m<sup>3</sup> for the lower crust and 3300 kg/m<sup>3</sup> for the upper mantle (Dziewonski and Anderson, 1981;  
840 Campos-Enríquez and Sánchez-Zamora, 2000; Davies, 2013). A reasonable available up today compilation of  
841 crust data for Los Humeros volcanic complex is recovered by the measure N°10 of the Crust 1.0 global model  
842 (Dziewonski and Anderson, 1981; Davies, 2013). The measure N°10 (yellow star in Fig. 1) is located within the  
843 study area at the southern termination of the Tepeyahualco Lava Flow and describes a crust (Fig. 12) made  
844 of five main seismic layers: i) upper sediments (thickness: 1km, density 2110 km/m<sup>3</sup>), ii) middle sediments  
845 (thickness: 0.5 km, density 2370 km/m<sup>3</sup>), iii) upper crust (thickness: 13.58 km, density 2740 km/m<sup>3</sup>), iv) middle  
846 crust (thickness: 15.27 km, density 2830 km/m<sup>3</sup>), and v) lower crust (thickness: 13.58 km, density 2920  
847 km/m<sup>3</sup>). Inferred (seismic) Moho depth is reported at -41.67 km with an upper mantle density of 3310 km/m<sup>3</sup>  
848 (Dziewonski and Anderson, 1981; Davies, 2013). Here we use a five-tiered density model, as derived from the  
849 Crust 1.0 global model, for the 41.67 Km continental crust beneath Los Humeros caldera, to convert obtained  
850 pressure estimates to depths.

851 The thermobarometry models applied to the LHPCS lavas define a broad region of crystallization between 0  
852 and ca. 30 km in depth that can be described with a quadrimodal distribution of pressure values (Fig. 12),  
853 which allow us to propose a complex polybaric continuous heterogenous multilayered transport and storage  
854 magmatic system.

855 A deep-seated anhydrous Ol-basalt reservoir at depths of ca. 28-33 km (7.6-9.2 kbar), at the boundary  
856 between lower and middle crust, below the caldera is recorded by (a) An-rich plagioclase cores (XAn = 50-70  
857 %), and (b) Ti-rich augitic clinopyroxene Cpx1 cores (Mg# up to 75, TiO<sub>2</sub> up to 4.57 wt%) of Cpx1. Overlapping  
858 the calculated anhydrous temperature values from plagioclase-liquid, Cpx1 clinopyroxene-liquid and olivine-  
859 liquid pairs provide a total range of ca. 1000 – 1300 °C for this mafic reservoir. Highest anhydrous  
860 temperature values are achieved for Cpx-free Ol-basalt Texcal lava flow (LH18) where the convergence of

861 plagioclase-liquid thermobarometry and olivine-liquid thermometry models indicate conditions of ca. 1230-  
862 1270°C at ca. 8 kbar. Lower anhydrous temperatures of ca. 1000-1210 °C, are obtained at a comparable  
863 average pressure value of 7.6 kbar for Cpx-bearing intra caldera Ol-basalts (LH5-2; LH 27-1). These results are  
864 in agreement with existing literature on the near-liquidus melting behavior of high-Al basaltic magmas (Mg#  
865 ca. 60-70 and Al<sub>2</sub>O<sub>3</sub>: 17-19 wt%) under dry conditions (e.g., Thompson, 1974; Grove et al., 1982; Crawford et  
866 al., 1987; Bartels et al., 1991; Grove, 2000). At 1250-1300 °C and ca. 10 kbar (Point A in Fig. 11) the basaltic  
867 melt is in equilibrium with a mantle peridotite mineral assemblage of olivine + clinopyroxene (Kushiro and  
868 Yoder, 1966; Presnall et al., 1978; Grove et al., 1982; Fuji and Scarfe, 1985; Takahashi, 1986; Fallon and Green,  
869 1987; Bartels et al., 1991; Sisson and Layne, 1993; Wagner et al., 1995; Grove et al., 1997; Grove, 2000; Kinzler  
870 et al., 2000). Following the models proposed by Thompson (1974), Bartels et al. (1991) and Grove (2000), a  
871 temperature decrease would lead primary melts to pass the “dry basaltic liquidus” and start the  
872 crystallization of Ol+Pl (higher temperatures) or Ol+Cpx+Pl (lower temperatures) assemblages (see stability  
873 fields in Fig. 11). Given the ubiquitous presence in all LHPCS basalts of well-developed euhedral to subhedral  
874 olivine crystals (both phenocrystals and microlites) at equilibrium with anorthitic plagioclase, it is possible to  
875 exclude that crystallization history started at depth > ca. 10-12 kbar where olivine is not a stable phase and  
876 the primary assemblage would be characterized only by Cpx+Pl+Sp in equilibrium with melt (Kushiro and  
877 Yoder, 1966; Thompson, 1974; Presnall et al., 1978; Bartels et al., 1991; Grove, 2000).

878 A second magma transport and storage systems can be recognized at depths of 15-30 km (ca. 4.5 – 7.8 kbar),  
879 in continuity with the deeper basaltic reservoir and distributed along the whole middle crust thickness, as  
880 recorded by the wide range of pressure estimates obtained from plagioclase (XAn= 40-70%) and Cpx2  
881 clinopyroxene cores (Mg#: 59-84; TiO<sub>2</sub> mean value 0.99 wt%). Thermometry models based on plagioclase,  
882 Cpx2 clinopyroxene and olivine show convergence for hydrous temperature values in the range of 979 – 1263  
883 °C. Thermobarometry models, together with textures and petrographic relations in all analyzed  
884 trachyandesite and trachyte samples suggest that all plagioclase, all Cpx2 clinopyroxene phenocrysts, and  
885 part of microlites, grew in this second storage system. In particular, it is possible to observe two main  
886 crystallization temperature conditions: (a) at ca. 1190°C (weighted mean value, MSWD= 2.2, n= 205)  
887 plagioclase phenocrysts crystallization in trachyandesite melts is observed, whereas (b) at the lower  
888 temperature of ca. 1070 °C (weighted mean value, MSWD= 1.7, n= 155) is reported the crystallization of all  
889 olivine, all Cpx2 phenocrysts, and plagioclase phenocryst in trachytes. We interpret the common Pl+Cpx2  
890 phenocryst-forming barometric conditions as evidence of a growth-dominated regime within this second  
891 magma storage zone (e.g., Barclay et al., 1998; Humphreys et al., 2006; Scott et al., 2012), whereas the  
892 smaller crystals (microcrystals and microlites) represent the nucleation-dominated regime (Scott et al., 2012)  
893 that can be associated with ascent-related decompression of melts at shallower levels (e.g., Cashman, 1992;  
894 Cashman and Blundy, 2000; Humphreys et al., 2009).

895 The third melt storage zone occurs at shallower depths of ca. 10-15 km, possibly corresponding to the  
896 transition between middle- and upper-crust, as indicated by convergence of barometric estimates (weighted  
897 mean value of  $3.9 \pm 0.2$  kbar ( $\pm 1\sigma$ ), MSWD= 0.80, n= 203; P ranging ca. 1-7 kbar) obtained from Cpx3  
898 clinopyroxene (i.e., unzoned phenocrysts and overgrowth/rims around earlier formed Cpx1- and Cpx2-cores)  
899 population. Cpx3 clinopyroxene-liquid thermometry model indicates, for this third storage zone a mean  
900 temperature of 1040 °C (weighted mean value, MSWD= 2.6, n= 203; T ranging ca. 940-1210 °C) comparable  
901 to those calculated for Ol+Cpx2 assemblages in the previous described second and deeper stagnation system.  
902 The obtained pressure estimates for the second and the third storage systems are compatible with multiple  
903 magma storage pockets, in which melts of comparable compositions ascend slowly enough for phenocrysts  
904 to form (e.g. Scott et al., 2012), and start cooling before the final ascent to shallower conditions (e.g., Dahren  
905 et al., 2012; Chadwick et al., 2013; Gardner et al., 2013; Jeffery et al., 2013; Preece et al., 2013; Troll et al.,  
906 2013). Taking into account the textures and the chemistry of Cpx3 clinopyroxene phenocrysts, the obtained  
907 thermobarometric estimates could be interpreted as the pressure-temperature environment of last major  
908 levels of magma stagnation and fractionation (Putirka, 1997; Klugel et al., 2005; Galipp et al., 2006; Stroncik  
909 et al., 2009).

910 The fourth shallowest storage zone located at depths of ca. 3-7 km (weighted mean value of  $1.5 \pm 0.2$  kbar  
911 ( $\pm 1\sigma$ ), MSWD= 0.24, n= 177; P ranging ca. 0.1-4.5 kbar), is required to explain the presence of i) Cpx4  
912 clinopyroxene (microcrystals and microlites) in all LHPCS lavas, ii) Aeg-rich Cpx5 clinopyroxene in basalts, and  
913 iii) Fe-olivine ( $Fo = 55-65\%$ ) and orthopyroxene in Opx-bearing evolved LHPCS lavas. Magmas in this shallow  
914 storage system show a wide range of temperature values calculated for hydrous melts: a) ca. 1060 °C  
915 (weighted mean value, MSWD= 2.4, n= 7) for Aeg-rich Cpx5 crystallization in basalts, b) ca. 1070 °C (weighted  
916 mean value, MSWD= 1.09, n= 168) for Cpx4 and Opx crystallization in trachyandesites, and c) ca. 965 °C  
917 (weighted mean value, MSWD= 2.2, n= 78) for olivine, Cpx4 and Opx crystallization in trachytes. Thermobaric  
918 estimates obtained for Aeg-rich Cpx5 agree with those calculated for transitional basalts at Pantelleria (White  
919 et al., 2009 and references therein), whereas orthopyroxene crystallization conditions overlap with the  
920 existing literature for intermediate rocks (e.g., Rutherford et al., 1985; Wallace and Anderson, 2000; Reubi  
921 and Nicholls, 2004; Allan et al., 2013; Jeffery et al., 2013). The broad distribution of melt chemistry from  
922 basalt to trachyte, together with the obtained thermobaric estimates, define a shallow magma storage  
923 environment characterized by progressive accumulation of small locally interconnected magma pockets and  
924 batches (e.g., Reubi and Nicholls, 2004; Jeffery et al., 2013) dispersed in the upper crust (<10 km) with a  
925 possible magma plexus at a depth of 2-4 km under the caldera (e.g., Armienti et al., 1989; Freundt and  
926 Schminke, 1995; Pietruszka and Garcia, 1999; Patanè et al., 2003; Klugel et al., 2005; Stroncik et al., 2009;  
927 Dahren et al., 2012; Jeffery et al., 2013; Coombs and Gardner,, 2001, 2004).

928

#### 929 **8.4 "Standard" versus multilayered magmatic plumbing system**

930 Existing conceptual models for LHVC are based on the “Standard Model” (*sensu* Gualda and Ghiorso, 2013),  
931 hypothesizing a single, bowl-shaped, long-lived, melt-dominated huge classical magma chamber of 1000-  
932 1500 Km<sup>3</sup> in volume, at depth of 5 to 10 km from the surface (Verma, 1983, 1984, 1985a, 1985b; Verma and  
933 Lopez, 1982; Verma et al., 1990; Verma and Andaverde, 1995; Verma et al., 2011; Verma et al. 2013;  
934 Carrasco-Núñez et al., 2018). However, these models mainly refer to the Los Humeros Caldera stage activity  
935 (Carrasco-Núñez et al., 2018 and references therein), lasted ca. 130 ky, where the major caldera-forming  
936 events (Xaltipan and Zaragoza ignimbrites, 115Km<sup>3</sup> and 15Km<sup>3</sup> DRE, respectively) and the large Plinian  
937 eruptive episode (Faby Tuff, 10km<sup>3</sup> DRE) necessitated feeding from a huge, voluminous magma chamber  
938 (Carrasco-Núñez and Branney, 2005; Carrasco-Núñez et al., 2018).

939 On the other hand, the Holocene eruptive phase of the LHPCS is a characterised by bimodal volcanism  
940 (Carrasco- Núñez et al., 2017a; Carrasco-Núñez et al., 2017b; Carrasco-Núñez et al., 2018), typified by  
941 alternating episodes of effusive and explosive volcanism with a wide range of compositions, spanning from  
942 basaltic to trachytic lava flows and mafic to felsic pumice and scoria fall deposits, erupted by tens of  
943 monogenetic eruptive centers located in the LHVC (e.g., Norini et al., 2015; Carrasco- Núñez et al., 2017a;  
944 Carrasco-Núñez et al., 2017b; Carrasco-Núñez et al., 2018 ). This volcanic activity is characterized by  
945 patially distributed, small volumes of erupted material (ca. 6 km<sup>3</sup> of mafic lavas, 10 km<sup>3</sup> of intermediate and  
946 felsic lava, and 1 km<sup>3</sup> of mafic and felsic tephra; Carrasco-Núñez and Branney, 2005). Furthermore, elements  
947 such as the lithic-free character of the LHPCS volcanic products, their overall textures and chemistry of  
948 mineral assemblages, coupled with the results from RFC-models, suggest that LHPCS magmatism is  
949 characterized by batches of magma evolving in a nearly closed system, unaffected by magmatic assimilation  
950 and mixing/recharge processes. In particular, the almost complete lack of magma mixing/recharge events  
951 (e.g., Lee et al., 2014) is confirmed by the absence of the typical expected minerals textures (e.g., Streck,  
952 2008; Renjith, 2014) such as: (i) fine-sieve textures and resorption surfaces due to reaction with a more  
953 primitive magma; (ii) glomerocryst-forming due to the recrystallization/suturing at rim of resorbed crystals;  
954 (iii) reverse zoning due to compositional inversion in open/recharged system; and (iv) reaction rims,  
955 breakdown mantle and crystal clots due to the disequilibrium-triggered recrystallization into a new set of  
956 minerals instead of dissolution.

957 The existing literature focused on magma recharge (e.g., De Paolo, 1981; Hofmann, 2012; O’Neill and Jenner,  
958 2012; Lee et al., 2014) highlights that a high evacuation/eruption efficiency will shorten the residence-time  
959 of magma in the storage chamber and will reduce the effect of crystallization in modifying the magma  
960 composition (Lee et al., 2014). Moreover, in case of eruption/evacuation rates higher than the recharge rates  
961 (e.g., Lee et al., 2014), it is possible to hypothesize a magmatic system dominated by ephemeral closed-  
962 system magma batches not affected by major mixing processes prior their evacuation/eruption (e.g., De  
963 Paolo, 1981; Hofmann, 2012; O’Neill and Jenner, 2012; Lee et al., 2014). This scenario best approximates the  
964 characteristics observed for all the Holocene LHPCS magmatic products. In addition, the absence of liquid-

965 dominated zone(s) (e.g., Bachmann and Bergantz, 2008) where mixing could occur (e.g., Cashman and  
966 Giordano, 2014), moreover suggests that the remnants of the huge magma chamber of the LH caldera stage  
967 are now completely solidified and crosscut by the uprising LHPCS mafic and felsic magmas. Once more, this  
968 scenario points out the incompatibility of the LHPCS magmatic activity with a feeding system dominated by  
969 the single voluminous magma chamber. This scenario is also coherent with the post-caldera eruption  
970 behavior observed in other volcanic complexes, such Ischia (e.g., Casalini et al., 2017), and it is consistent  
971 with the recent literature proposing complex magma chamber reservoirs made up of multiple discrete melt  
972 pockets with no mass-exchange and reactivated shortly before eruption (e.g., Cashman and Giordano, 2014;  
973 Cashman et al., 2017; Casalini et al., 2017).

974 Thermobarometric estimates obtained in this work, combined with the previous observations, with the  
975 existing literature and integrated with information from the crustal structure beneath Los Humeros caldera,  
976 therefore permit us to discard the “standard model” of the huge voluminous chamber in favor of a more  
977 reliable conceptual model characterized by a polybaric magmatic plumbing system of multiple, more or less  
978 interconnected magma transport and storage layers, transient batches and ponds of different magmas,  
979 localized beneath Los Humeros nested caldera and feeding the Holocene activity of the Los Humeros volcanic  
980 complex. Our results indicate that magma transport and storage levels, beneath Los Humeros caldera, are  
981 vertically distributed across the whole crust from ca. 30 to 3 km (from the lower- to the very upper-crust)  
982 with density contrasts between different crustal layers acting as a controlling parameter for ascending or  
983 stalling magmas (e.g., Dahren et al., 2012), reflecting the buoyant magma compositions and the melt  
984 fractions (e.g., Cashman et al., 2017; Jackson et al., 2018). Moreover, it is possible to propose that each of  
985 these crust/density boundaries will determine lateral transport and grow of magma stagnation pockets (e.g.,  
986 Dahren et al., 2012; Jackson et al., 2018). At depths <5km, buoyant magmas and fractionated melts (from  
987 mafic to felsic) ascending from all the lower storage zones, are stalled once more. The shallowest complex  
988 multi-storage system is interpreted as a plexus of scattered, more or less interconnected, ephemeral small-  
989 volume batches and pockets of melts, without any defined spatial distribution as ruled out by field-locations  
990 of the LHPCS studied lavas eruptive centers.

991 A shallow storage zone presenting magmas with heterogenous compositions (from mafic to felsic) has been  
992 already proposed by Dávila-Harris and Carrasco-Núñez (2014) to explain the eruptive history of the intra-  
993 caldera Cuicuiltic Member that was produced by the coeval eruption of compositionally contrasting unmixed  
994 magmas. However, a shallow ponding system characterized by heterogeneous composition of magmas  
995 involved beneath Los Humeros caldera is not an exceptional case. Examples of shallow heterogeneous  
996 reservoirs beneath active volcanic complexes are widely reported (e.g., Nairn et al., 1998; Kratzmann et al.,  
997 2009; Sigmarsson et al., 2011; Keiding and Sigmarsson, 2012).

998 Our results also agree with the work of Creon et al. (2018) where calculated fluid saturation depths derived  
999 for melt inclusions in post-caldera lavas indicate different magma-ponding levels within a range of depths

1000 between 5 and 13 km, coupled with a possible deeper reservoir/origin (26-32 km) and a final shallow  
1001 stagnation level (ca. 1.5-3.0 km).

1002

### 1003 **8.5 Implications for the active geothermal systems**

1004 The geothermal activity of a volcanic complex is expected to be the result of stagnation and cooling of  
1005 magmas in the shallower storage zone (e.g., Gunnarsson and Aradóttir, 2015), where classic conductive  
1006 models are mainly controlled by age and volume of the magmatic system representing the heat source (Smith  
1007 and Shaw, 1975; Cathles et al., 1997; Duffield and Sass, 2003; Gunnarsson and Aradóttir, 2015; Carrasco-  
1008 Núñez et al., 2018).

1009 As widely demonstrated (e.g., Smith and Shaw, 1975; Cathles et al., 1997), a very large intrusion will produce  
1010 a long-lived hydrothermal/geothermal system. Many numerical models (e.g., Cathles et al., 1997) suggest  
1011 that, in the most favorable conditions, a voluminous ( $>2000\text{km}^3$ ) intrusion/chamber of mafic melt could be  
1012 able to sustain a convective geothermal system up to 800 Ky. Opposite, very small mafic sills and dikes  
1013 intrusions ( $<10\text{ km}^3$ ) produce very localized thermal anomalies and could cool down to the solidus  
1014 temperature in lesser than 0.1 ky (Nabelek et al., 2012), and definitively cool in ca. 1 ky (e.g. Cathles et al.,  
1015 1997). Convection due to hydrothermal fluids circulation, increase the cooling rate of a magmatic intrusion  
1016 (Cathles et al., 1997). Concerning Los Humeros caldera, in the shallower magmatic plexus, every LHPCS  
1017 magma pocket and cryptodome (see. Urbani et al., submitted to SE) could be interpreted as a scattered and  
1018 localized short-living (ca. 0.1-1 ky; Cathles et al., 1997) heat source, whereas the cooling and solidified  
1019 remnants of the huge magma chamber of the caldera stage could still represent a background positive  
1020 thermal anomaly.

1021 The present geothermal activity of LHVC is characterized by a limited NNW-SSE non-homogeneous areal  
1022 distribution within the Los Potreros nested caldera (e.g., Norini et al., 2015; Urbani et al., submitted  
1023 manuscript). Based on (i) the young age (Upper Pleistocene-Holocene) of most of LHPCS volcanic activity, (ii)  
1024 the relatively small erupted volumes of LHPCS lavas, in particular of those erupted within the Los Potreros  
1025 caldera, and (iii) a shallow-crust plexus involving heterogeneous unmixed magmas, as derived by results  
1026 obtained in this work, we therefore discard the hypothesis of a single, large and voluminous shallow  
1027 magmatic chamber homogeneously distributed beneath the caldera, in favor of a more reliable scenario  
1028 characterized by a superficial plexus made of small single-charge ephemeral pockets of different magmas  
1029 localized beneath Los Humeros nested caldera, very close or within the Los Humeros exploited geothermal  
1030 field. In this view, within the Los Humeros caldera every LHPCS magma pocket and cryptodome (see. Urbani  
1031 et al., submitted manuscript) could be interpreted as a scattered and localized short-living (ca. 0.1-1 ky;  
1032 Cathles et al., 1997) heat source, whereas the cooling and solidified remnants of the huge magma chamber  
1033 of the caldera stage could still represent a background positive thermal anomaly affecting the volcanic field.

1034 Our reconstruction of the Los Humeros heat source therefore suggests the possible existence of a wide  
1035 background positive thermal anomaly associated to the cooling solidified remnants of the voluminous  
1036 magma chamber of the caldera stage, with juxtaposition of scattered high-frequency heat sources related to  
1037 the very shallow intrusive complex constituting the superficial plexus of the LHPCS magmatic plumbing  
1038 system.

1039 In the light of our results, a revision/update of the heat source, feeding the Los Humeros geothermal system  
1040 is needed to produce correct and up-to-date geothermal potential estimates of the geothermal field and to  
1041 develop efficient geothermal exploration and exploitation strategies.

1042

## 1043 9.CONCLUSIONS

1044 In this study we propose an integrated field-based petrographic-mineralogical approach to unravel the  
1045 evolution and configuration of the present-day magmatic plumbing system that is feeding the post-Caldera  
1046 stage activity of Los Humeros volcanic complex. The main results of this study can be summarized as follows.

- 1047 • The Rayleigh fractional crystallization (RFC) models demonstrate that all LHPCS magmas, from basalts  
1048 to trachytes, belong to the same line of descent and evolve through a progressive fractionation of  
1049 the Pl+Cpx+Ol+Sp mineral assemblage.
- 1050 • A polybaric complex transport and storage system, characterized by multiple magma levels more or  
1051 less interconnected in time, has been recognized based on application of mineral-melt  
1052 thermobarometry models.
- 1053 • A deep mafic reservoir (ca. 30km) is identified by Pl+Ol assemblage in basalts. Intermediate magma  
1054 storage systems (in the whole middle crust) are described by the progressive evolution of  
1055 clinopyroxene phenocryst-compositions and a shallow magmatic stagnation system (ca. 1.5kbar, 3-  
1056 5km) has been defined by crystallization of clinopyroxene microlites, aegirine clinopyroxenes in  
1057 basalt, and in particular by orthopyroxene formation in most evolved melts. All cpx-bearing lavas are  
1058 produced by progressive differentiation via polybaric fractional crystallization during magmas ascend  
1059 through the plumbing system.
- 1060 • The compositional behavior of the main phases (olivine, plagioclase, clinopyroxene, orthopyroxene),  
1061 together with their preserved textures and results from FC-modelling, permits to exclude, at this  
1062 stage, a magmatic feeding system dominated by magma mixing and magma replenishment, in favor  
1063 of a plumbing system dominated by levels, pockets and batches of melt underwent single charge.
- 1064 • The thermobarometric results obtained in this work indicate that, unlike previously believed, the  
1065 present configuration of the plumbing system is vertically extensive across the entire crust with a  
1066 deeper residence zone for basalts at 8 kbar (ca. 30-33 km) and a complex middle to very upper crust  
1067 zone (0.5 kbar) where basalts rapidly ascend and stall prior to erupt and where smaller batches of



1068 magma differentiate to trachyandesites and trachytes at times interconnected with the lower  
1069 feeding zone.

- 1070 • The main outcome for the modeling of the magmatic heat source of the geothermal system is the  
1071 inadequacy of conservative conceptual models based on the classical melt-dominated, single,  
1072 voluminous, long-lived magma chamber (i.e., “Standard Model”), in favor of an innovative and more  
1073 realistic vision of magmatic plumbing systems made of multiple, more or less interconnected magma  
1074 transport and storage layers within the crust, feeding small (ephemeral) magma pockets at shallow-  
1075 crust conditions.
- 1076 • The proposed model for the magmatic plumbing system at LHVC provides a new configuration of the  
1077 heat source feeding the present geothermal reservoir, and therefore, must be consider it for  
1078 geothermal **exploration and exploitation** purposes.
- 1079 • **Our study demonstrate that petrology represents a consistent method able to unravel the anatomy**  
1080 **of complex magmatic plumbing system.**

1081

## 1082 **APPENDIX A: Analytical details**

### 1083 **A.1 Petrography of volcanic samples**

1084 Rock magmatic fabrics, textures and mineral assemblages were studied on polished thin sections, using a  
1085 Nikon Eclipse 50iPol polarized light microscope (PLM) equipped with Nikon Ds-Fi2 CCD camera (Nikon, Tokyo,  
1086 Japan) and Nikon Nis-Elements software (Ver4.30.01), at Laboratorio di Microtettonica, Dip. Science,  
1087 Università Roma Tre (Roma, Italia). Mineral abbreviations follow Whitney and Evans (2010).

1088

### 1089 **A.2 Bulk major element geochemistry**

1090 After washing in distilled water, samples were grounded in an agate mill, pre-contaminated with an aliquot  
1091 of sample. Whole-rock major element concentrations (4 samples) were measured at the Activation  
1092 Laboratories (Ontario, Canada), through ion coupled plasma (ICP)- optical emission (OE). **For major elements**  
1093 **the uncertainty (1 sigma) is estimated better than 2% for values higher than 5 wt %, and better than 5% in**  
1094 **the range 0.1-5 wt %.** Additional samples (9) were analyzed by X-ray fluorescence (XRF) using a ZSX Primus II  
1095 (Rigaku Co., Japan) at Nagoya University, Japan. Loss on ignition (LOI) was measured from the sample powder  
1096 weight in a quartz glass beaker in the oven at 950°C for five hours. XRF-analyses were carried out following  
1097 the procedure presented in Azizi et al., (2015; 2018a; 2018b). **For major elements the uncertainty (1 sigma)**  
1098 **is estimated better than 1% for values higher than 10 wt %, and better than 5% in the range 0.1-10 wt %.**

1099

### 1100 **A.3 Mineral chemistry**

1101 Polished thin sections (13 samples) selected for petrography investigations, were then studied for mineral  
1102 chemistry and ca. 2400 analyses of mineral phases were obtained with a Cameca SX100 electron microprobe  
1103 (EMP) at the Institut für Anorganische Chemie, Universität Stuttgart. Operating conditions were 15 kV and  
1104 10 to 15 nA, counting times of 20 s both for peak and background. Compositions were determined relative  
1105 to natural and synthetic standards. Spot sizes were 1-10 µm depending on the phases analyzed. **For major**  
1106 **elements the uncertainty (1 sigma) is estimated better than 2% for SiO<sub>2</sub> content, and better than 1% for the**  
1107 **other measured elements.** Back Scattered Electron (BSE) imaging was obtained by using the same electron  
1108 microprobe with operating conditions of 15 kV, 50 nA. Mineral structural formulae of feldspar, olivine and  
1109 spinel were calculated through the software CalcMin\_32 (Brandelik, 2009). Mineral structural formulae of  
1110 orthopyroxene were calculated following Putirka et al. (1996) and Putirka (2008). Clinopyroxene formula has  
1111 been calculated following procedures reported in Putirka et al. (1996), Putirka (2008), Masotta et al. (2013).  
1112 Clinopyroxenes were then classified integrating the Wo-En-Fs scheme (Morimoto, 1989) and J vs. Q scheme  
1113 (Morimoto, 1988, 1989) with J= 2Na apfu and Q= (Ca+Mg+Fe<sup>2+</sup>) apfu. Aegirine (XAeg) component correction,  
1114 for Na-rich Cpx (Aegirine-Augite series), followed the scheme (XAeg= Na apfu if Na < Fe<sup>3+</sup> Tot, XAeg= Fe<sup>3+</sup> Tot  
1115 apfu if Na > Fe<sup>3+</sup>Tot) proposed by Putirka et al. (1996), Putirka (2008) and based on Fe<sup>2+</sup> - Fe<sup>3+</sup> correction of  
1116 Lindsley (1983).

1117

1118 **ACKNOWLEDGMENTS**

1119 **The authors are grateful to Dr. C.M. Petrone and to an anonymous reviewer for their helpful and constructive**  
1120 **comments that deeply contributed to improve the manuscript.** The authors wish to thank the Comisión  
1121 Federal de Electricidad (CFE, Mexico) for their assistance and support. This paper presents results of the  
1122 GEMex Project, funded by the European Union's Horizon 2020 programme for Research and Innovation  
1123 under grant agreement No. 727550 (scientific responsibility Guido Giordano), and by the Mexican Energy  
1124 Sustainability Fund CONACYT-SENER, Project 2015-04-268074 (WP 4.5, scientific responsibility Gerardo  
1125 Carrasco-Núñez). More information can be found on the GEMex Website: <http://www.gemex-h2020.eu>.  
1126 Authors would like to thank G. Norini for usefull discussions in the field. Special thanks to Javier Hernández,  
1127 Jaime Cavazos, Francisco Fernández and Alessandra Pensa for their support in the fieldwork and logistics.  
1128 The Grant to Department of Science, Roma Tre University (MIUR-Italy Dipartimenti di Eccellenza, ARTICOLO  
1129 1, COMMI 314-337 LEGGE 232/2016) is gratefully acknowledged.

1130

1131

1132 **REFERENCES**

1133

1134 Allan, A. S., Morgan, D. J., Wilson, C. J., and Millet, M. A.: From mush to eruption in centuries: assembly of  
1135 the super-sized Oruanui magma body. *Contrib. Mineral. Petr.*, 166, 143-164, 2013.

1136

1137 Annen, C.: From plutons to magma chambers: Thermal constraints on the accumulation of eruptible silicic  
1138 magma in the upper crust. *Earth Planet. Sc. Lett.*, 284, 409-416, 2009.

1139

1140 Armienti, P., Innocenti, F., Petrini, R., Pompilio, M., and Villari, L.: Petrology and Sr-Nd isotope geochemistry  
1141 of recent lavas from Mt. Etna: bearing on the volcano feeding system. *J. Volcanol. Geoth. Res.*, 39,  
1142 315-327, 1989.

1143

1144 Arndt, N. T., and Jenner, G. A.: Crustally contaminated komatiites and basalts from Kambalda, Western  
1145 Australia. *Chem. Geol.*, 56, 229-255, 1986.

1146

1147 Aulinas, M., Gimeno, D., Fernandez-Turiel, J. L., Perez-Torrado, F. J., Rodriguez-Gonzalez, A., and Gasperini,  
1148 D.: The Plio-Quaternary magmatic feeding system beneath Gran Canaria (Canary Islands, Spain):  
1149 constraints from thermobarometric studies. *J. Geol. Soc. London*, 167, 785-801, 2010.

1150

1151 Azizi, H., Najari, M., Asahara, Y., Catlos, E. J., Shimizu, M., and Yamamoto, K.: U–Pb zircon ages and  
1152 geochemistry of Kangareh and Taghiabad mafic bodies in northern Sanandaj–Sirjan Zone, Iran:  
1153 Evidence for intra-oceanic arc and back-arc tectonic regime in Late Jurassic. *Tectonophysics*, 660, 47-  
1154 64, 2015.

1155

1156 Azizi, H., Lucci, F., Stern, R. J., Hasannejad, S., and Asahara, Y.: The Late Jurassic Panjeh submarine volcano in  
1157 the northern Sanandaj-Sirjan Zone, northwest Iran: Mantle plume or active margin? *Lithos*, 308, 364-  
1158 380, 2018a.

1159

1160 Azizi, H., Nouri, F., Stern, R. J., Azizi, M., Lucci, F., Asahara, Y., Zarinkoub, M. H., and Chung, S. L.: New evidence  
1161 for Jurassic continental rifting in the northern Sanandaj Sirjan Zone, western Iran: the Ghalaylan  
1162 seamount, southwest Ghorveh. *Int. Geol. Rev.*, DOI: 10.1080/00206814.2018.1535913, 2018b.

1163

1164 Bachmann, O., and Bergantz, G.W.: On the origin of crystal-poor rhyolites: extracted from batholithic crystal  
1165 mushes, *J. Petrol.*, 45, 1565-1582, 2004.

1166

1167 Bachmann, O., and Bergantz, G.W.: Rhyolites and their source mushes across tectonic settings, *J. Petrol.*, 49,  
1168 2277-2285, 2008.

1169

1170 Barberi, F., Ferrara, G., Santacrose, R., Treuil, M., and Varet, J.: A transitional basalt-pantellerite sequence of  
1171 fractional crystallization, the Boina Centre (Afar Rift, Ethiopia), *J. Petrol.*, 16(1), 22-56, 1975.

1172

1173 Barclay, J., Rutherford, M. J., Carroll, M. R., Murphy, M. D., Devine, J. D., Gardner, J., and Sparks, R. S. J.:  
1174 Experimental phase equilibria constraints on pre-eruptive storage conditions of the Soufrière Hills  
1175 magma. *Geophys. Res. Lett.*, 25, 3437-3440, 1998.

1176

1177 Barker, A. K., Troll, V. R., Carracedo, J. C., and Nicholls, P. A.: The magma plumbing system for the 1971  
1178 Teneguía eruption on La Palma, Canary Islands. *Contrib. Mineral. Petr.*, 170, 54, 2015.

1179

1180 Bartels, K. S., Kinzler, R. J., and Grove, T. L.: High pressure phase relations of primitive high-alumina basalts  
1181 from Medicine Lake volcano, northern California. *Contrib. Mineral. Petr.*, 108, 253-270, 1991.

1182

1183 Beattie, P.: Olivine-melt and orthopyroxene-melt equilibria. *Contrib. Mineral. Petr.*, 115, 103-111, 1993.

1184  
1185 Bégué, F., Deering, C. D., Gravley, D. M., Kennedy, B. M., Chambefort, I., Gualda, G. A. R., and Bachmann, O.:  
1186 Extraction, storage and eruption of multiple isolated magma batches in the paired Mamaku and Ohakuri  
1187 eruption, Taupo Volcanic Zone, New Zealand. *J. Petrol.*, 55, 1653-1684, 2014.  
1188  
1189 Bellieni, G., Justin Visentin, E., Le Maitre, R. W., Piccirillo, E., and Mand Zanettin, B.: Proposal for a division of  
1190 the basaltic (B) field of the TAS diagram. IUGS subcommission on the Systematics of Igneous Rocks.  
1191 Circular no.38, Contribution no.102, 1983.  
1192  
1193 Bindeman, I. N., and Bailey, J. C.: Trace elements in anorthite megacrysts from the Kurile Island Arc: a window  
1194 to across-arc geochemical variations in magma compositions. *Earth Planet. Sc. Lett.*, 169(3-4), 209-226,  
1195 1999.  
1196  
1197 Brandelik, A.: CALCMIN—an EXCEL™ Visual Basic application for calculating mineral structural formulae from  
1198 electron microprobe analyses. *Comput. Geosci-UK*, 35, 1540-1551, 2009.  
1199  
1200 Brown, W. L., and Parsons, I.: Feldspars in igneous rocks. In Parsons I. (Ed): “Feldspars and their reactions”  
1201 (pp. 449-499). Springer, Dordrecht, 1994.  
1202  
1203 Bryan, W. B., Finger, L. T., and Chayes, F.: Estimating proportions in petrographic mixing equations by least-  
1204 squares approximation. *Science*, 163(3870), 926-927, 1969.  
1205  
1206 Campos-Enríquez, J. O., Garduño-Monroy, V. H.: The shallow structure of Los Humeros and Las Derrumbadas  
1207 geothermal fields, Mexico. *Geothermics*, 16, 539-554, 1987.  
1208  
1209 Campos-Enriquez, J. O., and Sánchez-Zamora, O.: Crustal structure across southern Mexico inferred from  
1210 gravity data. *J. S. Am. Earth Sci.*, 13, 479-489, 2000.  
1211  
1212 Carmichael, I. S. E., Nicholls, J., Spera, F. J., Wood, B. J., and Nelson, S. A.: High-temperature properties of  
1213 silicate liquids: applications to the equilibration and ascent of basic magma. *Philos. Tr. R. Soc. S-A*, 286,  
1214 373-431, 1977.  
1215  
1216 Carrasco-Núñez, G., and Branney, M.: Progressive assembly of a massive layer of ignimbrite with normal-to-  
1217 reverse compositional zoning: the Zaragoza ignimbrite of central Mexico. *B. Volcanol.*, 68, 3-20, 2005.  
1218  
1219 Carrasco-Núñez, G., Gómez-Tuena, A., and Lozano, L.: Geologic map of Cerro Grande volcano and  
1220 surrounding area, Central México. Geological Society of America Maps and Charts series MCH 081, pp.  
1221 10, 1997.  
1222  
1223 Carrasco-Núñez, G., Siebert, L., Díaz-Castellón, R., Vázquez-Selem, L., Capra, L.: Evolution and hazards of a  
1224 long-quiet compound shield-like volcano: Cofre de Perote, Eastern Trans-Mexican Volcanic Belt. *J.*  
1225 *Volcanol. Geoth. Res.*, 197, 209-224, <http://dx.doi.org/10.1016/j.jvolgeores.2009.08.010>, 2010.  
1226  
1227 Carrasco-Núñez, G., Dávila-Harris, P., Riggs, N. R., Ort, M. H., Zimmer, B. W., Willcox, C. P., and Branney, M.  
1228 J.: Recent explosive volcanism at the Eastern Trans-Mexican Volcanic Belt, in: Aranda-Gómez, J. J.,  
1229 Tolson, G., and Molina-Garza, R. S. (eds.), *The Southern Cordillera and Beyond*. Geological Society of  
1230 America Field Guide 25, p. 83–113, doi:10.1130/2012.0025(05), 2012a.  
1231  
1232 Carrasco-Núñez, G., McCurry, M., Branney, M. J., Norry, M., and Willcox, C.: Complex magma mixing,  
1233 mingling, and withdrawal associated with an intra-Plinian ignimbrite eruption at a large silicic caldera  
1234 volcano: Los Humeros of central Mexico. *Geol. Soc. Am. Bull.*, 124(11-12), 1793-1809, 2012b.  
1235

- 1236 Carrasco-Núñez, G., López-Martínez, M., Hernández, J., and Vargas, V.: Subsurface stratigraphy and its  
1237 correlation with the surficial geology at Los Humeros geothermal field, eastern Trans-Mexican Volcanic  
1238 Belt. *Geothermics*, 67, 1-17, 2017a.
- 1239
- 1240 Carrasco-Núñez, G., Hernández, J., De León, L., Dávila, P., Norini, G., Bernal, J. P., Jicha, B., Navarro, M., and  
1241 López-Quiroz, P.: Geologic Map of Los Humeros volcanic complex and geothermal field, eastern Trans-  
1242 Mexican Volcanic Belt/Mapa geológico del complejo volcánico Los Humeros y campo geotérmico, sector  
1243 oriental del Cinturón Volcánico Trans-Mexicano. *Terradigitalis*, 1, 1-11. DOI:  
1244 10.22201/igg.terrardigitalis.2017.2.24.78, 2017b.
- 1245
- 1246 Carrasco-Núñez, G., Bernal, J. P., Davila, P., Jicha, B., Giordano, G., and Hernández, J.: Reappraisal of Los  
1247 Humeros volcanic complex by new U/Th zircon and  $^{40}\text{Ar}/^{39}\text{Ar}$  dating: Implications for greater geothermal  
1248 potential. *Geochem. Geophys. Geosy.*, 19, 132-149, 2018.
- 1249
- 1250 **Casalini, M., Avanzinelli, R., Heumann, A., de Vita, S., Sansivero, F., Conticelli, S., and Tommasini, S.:**  
1251 **Geochemical and radiogenic isotope probes of Ischia volcano, Southern Italy: Constraints on magma**  
1252 **chamber dynamics and residence time. *Am. Mineral.*, 102(2), 262-274, 2017.**
- 1253
- 1254 Cashman, K. V.: Groundmass crystallization of Mount St. Helens dacite, 1980–1986: a tool for interpreting  
1255 shallow magmatic processes. *Contrib. Mineral. Petr.*, 109, 431-449, 1992.
- 1256
- 1257 Cashman, K., and Blundy, J.: Degassing and crystallization of ascending andesite and dacite. *Philos. T. Roy.*  
1258 *Soc. A*, 358, 1487-1513, 2000.
- 1259
- 1260 Cashman, K. V., and Giordano, G.: Calderas and magma reservoirs. *J. Volcanol. Geoth. Res.*, 288, 28-45, 2014.
- 1261
- 1262 Cashman, K. V., Sparks, R. S. J., and Blundy, J. D.: Vertically extensive and unstable magmatic systems: a  
1263 unified view of igneous processes. *Science*, 355, eaag3055, 2017.
- 1264
- 1265 **Cathles, L. M., Erendi, A. H. J., and Barrie, T.: How long can a hydrothermal system be sustained by a single**  
1266 **intrusive event? *Econ. Geol.*, 92(7-8), 766-771, 1997.**
- 1267
- 1268 Chadwick, J. P., Troll, V. R., Waight, T. E., van der Zwan, F. M., and Schwarzkopf, L. M.: Petrology and  
1269 geochemistry of igneous inclusions in recent Merapi deposits: a window into the sub-volcanic plumbing  
1270 system. *Contrib. Mineral. Petr.*, 165, 259-282, 2013.
- 1271
- 1272 Charlier, B. L. A., Bachmann, O., Davidson, J. P., Dungan, M. A., and Morgan, D. J.: The upper crustal evolution  
1273 of a large silicic magma body: evidence from crystal-scale Rb–Sr isotopic heterogeneities in the Fish  
1274 Canyon magmatic system, Colorado. *J. Petrol.*, 48, 1875-1894, 2007.
- 1275
- 1276 Clague, D. A., Moore, J. G., Dixon, J. E., and Friesen, W. B.: Petrology of submarine lavas from Kilauea's Puna  
1277 Ridge, Hawaii. *Oceanogr. Lit. Rev.*, 10, 857-858, 1995.
- 1278
- 1279 Clarke, A. B., Stephens, S., Teasdale, R., Sparks, R. S. J., and Diller, K.: Petrologic constraints on the  
1280 decompression history of magma prior to Vulcanian explosions at the Soufrière Hills volcano,  
1281 Montserrat. *J. Volcanol. Geoth. Res.*, 161, 261-274, 2007.
- 1282
- 1283 Coombs, M. L., and Gardner, J. E.: Shallow-storage conditions for the rhyolite of the 1912 eruption at  
1284 Novarupta, Alaska. *Geology*, 29, 775-778, 2001.
- 1285
- 1286 Coombs, M. L., and Gardner, J. E.: Reaction rim growth on olivine in silicic melts: Implications for magma  
1287 mixing. *Am. Mineral.*, 89, 748-758, 2004.

1288  
1289 Costa, F., Andreastuti, S., de Maisonneuve, C. B., and Pallister, J. S.: Petrological insights into the storage  
1290 conditions, and magmatic processes that yielded the centennial 2010 Merapi explosive eruption. *J.*  
1291 *Volcanol. Geoth. Res.*, 261, 209-235, 2013.  
1292  
1293 Crawford, A. J., Falloon, T. J., and Eggins, S.: The origin of island arc high-alumina basalts. *Contrib. Mineral.*  
1294 *Petr.*, 97, 417-430, 1987.  
1295  
1296 Créon, L., Levresse, G., Carrasco-Nuñez, G., and Remusat, L.: Evidence of a shallow magma reservoir below  
1297 Los Humeros volcanic complex: Insights from the geochemistry of silicate melt inclusions. *J. S. Am. Earth*  
1298 *Sci.*, 88, 446-458, 2018.  
1299  
1300 Dahren, B., Troll, V. R., Andersson, U. B., Chadwick, J. P., Gardner, M. F., Jaxybulatov, K., and Koulakov, I.:  
1301 Magma plumbing beneath Anak Krakatau volcano, Indonesia: evidence for multiple magma storage  
1302 regions. *Contrib. Mineral. Petr.*, 163, 631-651, 2012.  
1303  
1304 Daubeny, C. G. B.: Some account of the eruption of Vesuvius, which occurred in the month of August, 1834,  
1305 extracted from the manuscript notes of the cavaliere monticelli, foreign associate of the Geological  
1306 Society, and from other sources; together with a statement of the products of the eruption, and of the  
1307 condition of the volcano subsequently to it. In: *Abstracts of the Papers Printed in the Philosophical*  
1308 *Transactions of the Royal Society of London*, London: The Royal Society, 3, 326-327, 1837.  
1309  
1310 Davies, J. H.: Global map of solid Earth surface heat flow. *Geochem. Geophys. Geosy.*, 14, 4608-4622, 2013.  
1311  
1312 Dávila-Harris, P., and Carrasco-Núñez, G.: An unusual syn-eruptive bimodal eruption: the Holocene Cuicuiltic  
1313 Member at Los Humeros caldera, Mexico. *J. Volcanol. Geoth. Res.*, 271, 24-42, 2014.  
1314  
1315 Demant, A.: Características del Eje Neovolcánico Transmexicano y sus problemas de interpretación. *Rev. Mex.*  
1316 *Cienc. Geol.*, 2, 172-187, 1978.  
1317  
1318 DePaolo, D. J.: Trace element and isotopic effects of combined wallrock assimilation and fractional  
1319 crystallization. *Earth Planet. Sc. Lett.*, 53(2), 189-202, 1981.  
1320  
1321 Di Renzo, V., Wohletz, K., Civetta, L., Moretti, R., Orsi, G., and Gasparini, P.: The thermal regime of the Campi  
1322 Flegrei magmatic system reconstructed through 3D numerical simulations. *J. Volcanol. Geoth. Res.*, 328,  
1323 210-221, 2016.  
1324  
1325 Donaldson, C. H.: Olivine crystal types in harrisitic rocks of the Rhum pluton and in Archean spinifex rocks.  
1326 *Geol. Soc. Am. Bull.*, 85, 1721-1726, 1974.  
1327  
1328 Duda, A., and Schmincke, H. U.: Polybaric differentiation of alkali basaltic magmas: evidence from green-core  
1329 clinopyroxenes (Eifel, FRG). *Contrib. Mineral. Petr.*, 91, 340-353, 1985.  
1330  
1331 Duffield, W. A., and Sass, J. H.: Geothermal energy: Clean power from the earth's heat (Vol. 1249, p. 34).  
1332 Reston, VA: U.S. Geothermal Development, US Geological Survey, 2003.  
1333  
1334 Dungan, M. A., Long, P. E., and Rhodes, J. M.: Magma mixing at mid-ocean ridges: Evidence from legs 45 and  
1335 46-DSDP. *Geophys. Res. Lett.*, 5, 423-425, 1978.  
1336  
1337 Dziewonski, A. M., and Anderson, D. L.: Preliminary reference Earth model. *Phys. Earth Planet. In.*, 25, 297-  
1338 356, 1981.  
1339

1340 Elardo, S. M., and Shearer, C. K.: Magma chamber dynamics recorded by oscillatory zoning in pyroxene and  
1341 olivine phenocrysts in basaltic lunar meteorite Northwest Africa 032. *Am. Mineral.*, 99, 355-368, 2014.  
1342

1343 Ellis, B. S., Szymanowski, D., Wotzlaw, J. F., Schmitt, A. K., Bindeman, I. N., Troch, J., Harris, C., Bachmann, O.,  
1344 and Guillong, M.: Post-caldera volcanism at the Heise volcanic field: implications for petrogenetic  
1345 models. *J. Petrol.*, 58, 115-136, 2017.  
1346

1347 Eskandari, A., Amini, S., De Rosa, R., and Donato, P.: Nature of the magma storage system beneath the  
1348 Damavand volcano (N. Iran): An integrated study. *Lithos*, 300, 154-176, 2018.  
1349

1350 Falloon, T. J., and Green, D. H.: Anhydrous partial melting of MORB pyroxene and other peridotite compositions  
1351 at 10 kbar: implications for the origin of primitive MORB glasses. *Miner. Petrol.*, 37(3-4), 181-219, 1987.  
1352

1353 Faure, F., Trolliard, G., Nicollet, C., and Montel, J. M.: A developmental model of olivine morphology as a  
1354 function of the cooling rate and the degree of undercooling. *Contrib. Mineral. Petr.*, 145(2), 251-263,  
1355 2003.  
1356

1357 Feng, W., and Zhu, Y.: Decoding magma storage and pre-eruptive processes in the plumbing system beneath  
1358 early Carboniferous arc volcanoes of southwestern Tianshan, Northwest China. *Lithos*, 322, 362-375,  
1359 2018.  
1360

1361 Ferrari, L., López-Martínez, M., Aguirre-Díaz, G., and Carrasco-Núñez, G.: Space-time patterns of Cenozoic arc  
1362 volcanism in Central Mexico: from the Sierra Madre Occidental to the Mexican Volcanic Belt. *Geology*,  
1363 27, 303-306, 1999.  
1364

1365 Ferrari, L., Orozco-Esquivel, T., Manea, V., Manea, M.: The dynamic history of the Trans-Mexican Volcanic  
1366 Belt and the Mexico subduction zone. *Tectonophysics*, 522, 122-149, 2012.  
1367

1368 Ferriz, H., and Mahood, G. A.: Eruption rates and compositional trends at Los Humeros volcanic center,  
1369 Puebla, Mexico. *J. Geophys. Res-Sol. Ea.*, 89(B10), 8511-8524, 1984.  
1370

1371 Ferriz, H., and Mahood, G. A.: Strong compositional zonation in a silicic magmatic system: Los Humeros,  
1372 Mexican Neovolcanic Belt. *J. Petrol.*, 28, 171-209, 1987.  
1373

1374 Fitz-Díaz, E., Lawton, T. F., Juárez-Arriaga, E., and Chávez-Cabello, G.: The Cretaceous-Paleogene Mexican  
1375 orogen: Structure, basin development, magmatism and tectonics. *Earth-Sci. Rev.*, 183, 56-84, 2018.  
1376

1377 Fowler, A. D., Berger, B., Shore, M., Jones, M. I., and Ropchan, J.: Supercooled rocks: development and  
1378 significance of varioles, spherulites, dendrites and spinifex in Archaean volcanic rocks, Abitibi  
1379 Greenstone belt, Canada. *Precambrian Res.*, 115, 311-328, 2002.  
1380

1381 Freundt, A., and Schmincke, H. U.: Petrogenesis of rhyolite-trachyte-basalt composite ignimbrite P1, Gran  
1382 Canada, Canary Islands. *J. Geophys. Res-Sol. Ea.*, 100(B1), 455-474, 1995.  
1383

1384 Fujii, T., and Scarfe, C. M.: Composition of liquids coexisting with spinel lherzolite at 10 kbar and the genesis  
1385 of MORBs. *Contrib. Mineral. Petr.*, 90, 18-28, 1985.  
1386

1387 Galipp, K., Klügel, A., and Hansteen, T. H.: Changing depths of magma fractionation and stagnation during the  
1388 evolution of an oceanic island volcano: La Palma (Canary Islands). *J. Volcanol. Geoth. Res.*, 155, 285-306,  
1389 2006.  
1390



1391 Gao, J. F., and Zhou, M. F.: Generation and evolution of siliceous high magnesium basaltic magmas in the  
1392 formation of the Permian Huangshandong intrusion (Xinjiang, NW China). *Lithos*, 162, 128-139, 2013.  
1393

1394 Gardner, M. F., Troll, V. R., Gamble, J. A., Gertisser, R., Hart, G. L., Ellam, R. M., Harris, C., and Wolf, J. A.:  
1395 Shallow level differentiation processes at Krakatau: evidence for late-stage crustal contamination. *J.*  
1396 *Petrol.*, 54, 149-182, 2013.  
1397

1398 Gernon, T. M., Upton, B. G. J., Ugra, R., Yücel, C., Taylor, R. N., and Elliott, H.: Complex subvolcanic magma  
1399 plumbing system of an alkali basaltic maar-diatreme volcano (Elie Ness, Fife, Scotland). *Lithos*, 264, 70-  
1400 85, 2016.  
1401

1402 Geshi, N., and Oikawa, T.: The spectrum of basaltic feeder systems from effusive lava eruption to explosive  
1403 eruption at Miyakejima volcano, Japan. *B. Volcanol.*, 76(3), 797, 2014.  
1404

1405 Ginibre, C., Kronz, A., and Wörner, G.: High-resolution quantitative imaging of plagioclase composition using  
1406 accumulated backscattered electron images: new constraints on oscillatory zoning. *Contrib. Mineral.*  
1407 *Petr.*, 142(4), 436-448, 2002.  
1408

1409 Ginibre, C., Wörner, G., and Kronz, A.: Crystal zoning as an archive for magma evolution. *Elements*, 3, 261-  
1410 266, 2007.  
1411

1412 Giordano, G., Lucci, F., Phillips, D., Cozzupoli, D., and Runci, V.: Stratigraphy, geochronology and evolution of  
1413 the Mt. Melbourne volcanic field (North Victoria Land, Antarctica). *B. Volcanol.*, 74, 1985-2005, 2012.  
1414

1415 Giuffrida, M., and Viccaro, M.: Three years (2011–2013) of eruptive activity at Mt. Etna: working modes and  
1416 timescales of the modern volcano plumbing system from micro-analytical studies of crystals. *Earth-Sci.*  
1417 *Rev.*, 171, 289-322, 2017.  
1418

1419 Glazner, A. F., Bartley, J. M., Coleman, D. S., Gray, W., and Taylor, R. Z.: Are plutons assembled over millions  
1420 of years by amalgamation from small magma chambers? *GSA today*, 14, 4-12, 2004.  
1421

1422 Gómez-Tuena, A., and Carrasco-Núñez, G.: Cerro Grande volcano: the evolution of a Miocene stratocone in  
1423 the early Trans-Mexican Volcanic Belt, *Tectonophysics*, 318, 249-280, 2000.  
1424

1425 Gómez-Tuena, A., LaGatta, A.B., Langmuir, C.H., Goldstein, S.L., Ortega-Gutiérrez, F., Carrasco-Núñez, G.:  
1426 Temporal control of subduction magmatism in the eastern Trans-Mexican Volcanic Belt: mantle sources,  
1427 slab contributions, and crustal contamination. *Geochem. Geophys. Geosy.*, 4. [http://dx.doi.org/10.](http://dx.doi.org/10.1029/2003GC000524)  
1428 [1029/2003GC000524](http://dx.doi.org/10.1029/2003GC000524), 2003.  
1429

1430 Gómez-Tuena, A., Langmuir, C.H., Goldstein, S.L., Straub, S., Ortega-Gutiérrez, F.: Geochemical evidence for  
1431 slab melting in the Trans-Mexican Volcanic Belt. *J. Petrol.*, 48, 537–562, 2007a.  
1432

1433 Gómez-Tuena, A., Orozco-Esquivel, M.T., Ferrari, L.: Igneous petrogenesis of the Transmexican Volcanic Belt.  
1434 In: Alaniz-Álvarez, S.A., Nieto-Samaniego, A.F. (Eds.), *Geology of México: Celebrating the Centenary of*  
1435 *the Geological Society of México*. *Geol. S. Am. S.*, 422, 129–181, 2007b.  
1436

1437 Gómez-Tuena, A., Mori, L., Straub, S.: Geochemical and petrological insights into the tectonic origin of the  
1438 Transmexican Volcanic Belt, *Earth-Sci. Rev.* 183, 153-181.  
1439 <http://dx.doi.org/10.1016/j.earscirev.2016.12.006>, 2018.  
1440

1441 Gregg, P. M., De Silva, S. L., Grosfils, E. B., and Parmigiani, J. P.: Catastrophic caldera-forming eruptions:  
1442 Thermomechanics and implications for eruption triggering and maximum caldera dimensions on Earth.  
1443 J. Volcanol. Geoth. Res., 241, 1-12, 2012.  
1444

1445 Grove, T. L.: Origin of Magmas, Encyclopedia of Volcanoes, 133-148, 2000.  
1446

1447 Grove, T. L., Gerlach, D. C., and Sando, T. W.: Origin of calc-alkaline series lavas at Medicine Lake volcano by  
1448 fractionation, assimilation and mixing. Contrib. Mineral. Petr., 80, 160-182, 1982.  
1449

1450 Grove, T. L., Donnelly-Nolan, J. M., and Housh, T.: Magmatic processes that generated the rhyolite of Glass  
1451 Mountain, Medicine Lake volcano, N. California. Contrib. Mineral. Petr., 127, 205-223, 1997.  
1452

1453 Gualda, G. A., and Ghiorso, M. S.: The Bishop Tuff giant magma body: an alternative to the Standard Model.  
1454 Contrib. Mineral. Petr., 166, 755-775, 2013.  
1455

1456 Gunnarsson, G., and Aradóttir, E. S.: The deep roots of geothermal systems in volcanic areas: boundary  
1457 conditions and heat sources in reservoir modeling. Transport in Porous Media, 108, 43-59, 2015.  
1458

1459 Herzberg, C., and O'Hara, M. J.: Plume-associated ultramafic magmas of Phanerozoic age. J. Petrol., 43, 1857-  
1460 1883, 2002.  
1461

1462 Hildreth, W.: The Bishop Tuff: Evidence for the origin of compositional zonation in silicic magma chambers.  
1463 Geol. S. Am. S., 180, 43-75, 1979.  
1464

1465 Hildreth, W.: Gradients in silicic magma chambers: implications for lithospheric magmatism. J. Geophys. Res-  
1466 Sol. Ea., 86(B11), 10153-10192, 1981.  
1467

1468 Hildreth, W., and Wilson, C. J.: Compositional zoning of the Bishop Tuff. J. Petrol., 48, 951-999, 2007.  
1469

1470 **Hofmann, A. W.: Magma chambers on a slow burner. Nature 49, 677–678, 2012.**  
1471

1472 Holland, T., and Powell, R.: Plagioclase feldspars: activity-composition relations based upon Darken's  
1473 quadratic formalism and Landau theory. Am. Mineral., 77, 53-61, 1992.  
1474

1475 Humphreys, M. C., Blundy, J. D., and Sparks, R. S. J.: Magma evolution and open-system processes at  
1476 Shiveluch Volcano: Insights from phenocryst zoning. J. Petrol., 47, 2303-2334, 2006.  
1477

1478 Humphreys, M. C., Christopher, T., and Hards, V.: Microlite transfer by disaggregation of mafic inclusions  
1479 following magma mixing at Soufrière Hills volcano, Montserrat. Contrib. Mineral. Petr., 157, 609-624,  
1480 2009.  
1481

1482 Huraiová, M., Konečný, P., Holický, I., Milovská, S., Nemeč, O., and Hurai, V.: Mineralogy and origin of  
1483 peralkaline granite-syenite nodules ejected in Pleistocene basalt from Bulhary, southern Slovakia.  
1484 Period. Mineral., 86, 1-17, 2017.  
1485

1486 **Jackson, M. D., Blundy, J., and Sparks, R. S. J.: Chemical differentiation, cold storage and remobilization of  
1487 magma in the Earth's crust. Nature, 564(7736), 405, 2018.**  
1488

1489 Jeffery, A. J., Gertisser, R., Troll, V. R., Jolis, E. M., Dahren, B., Harris, C., Tindle, A. G., Preece, K., O'Driscoll,  
1490 B., Humaida, H., and Chadwick, J. P.: The pre-eruptive magma plumbing system of the 2007–2008 dome-  
1491 forming eruption of Kelut volcano, East Java, Indonesia. Contrib. Mineral. Petr., 166, 275-308, 2013.  
1492

1493 Jellinek, A. M., and DePaolo, D. J.: A model for the origin of large silicic magma chambers: precursors of  
1494 caldera-forming eruptions. *B. Volcanol.*, 65, 363-381, 2003.  
1495

1496 Keiding, J. K., and Sigmarsson, O.: Geothermobarometry of the 2010 Eyjafjallajökull eruption: New  
1497 constraints on Icelandic magma plumbing systems. *J. Geophys. Res-Sol. Ea.*, 117(B9),  
1498 doi:10.1029/2011JB008829, 2012.  
1499

1500 Kelley, D. F., and Barton, M.: Pressures of crystallization of Icelandic magmas. *J. Petrol.*, 49, 465-492, 2008.  
1501

1502 **Kinman, W. S., and Neal, C. R.: Magma evolution revealed by anorthite-rich plagioclase cumulate xenoliths**  
1503 **from the Ontong Java Plateau: insights into LIP magma dynamics and melt evolution. *J. Volcanol. Geoth.***  
1504 ***Res.*, 154(1-2), 131-157, 2006.**  
1505

1506 Kinzler, R. J., Donnelly-Nolan, J. M., and Grove, T. L.: Late Holocene hydrous mafic magmatism at the Paint  
1507 Pot Crater and Callahan flows, Medicine Lake Volcano, N. California and the influence of H<sub>2</sub>O in the  
1508 generation of silicic magmas. *Contrib. Mineral. Petr.*, 138, 1-16, 2000.  
1509

1510 Klügel, A., Hoernle, K. A., Schmincke, H. U., and White, J. D.: The chemically zoned 1949 eruption on La Palma  
1511 (Canary Islands): Petrologic evolution and magma supply dynamics of a rift zone eruption. *J. Geophys.*  
1512 *Res-Sol. Ea.*, 105(B3), 5997-6016, 2000.  
1513

1514 Klügel, A., Hansteen, T. H., and Galipp, K.: Magma storage and underplating beneath Cumbre Vieja volcano,  
1515 la Palma (Canary Islands). *Earth Planet. Sc. Lett.*, 236, 211-226, 2005.  
1516

1517 **Kontonikas-Charos, A., Ciobanu, C. L., Cook, N. J., Ehrig, K., Krneta, S., and Kamenetsky, V. S.: Feldspar**  
1518 **evolution in the Roxby Downs Granite, host to Fe-oxide Cu-Au-(U) mineralisation at Olympic Dam, South**  
1519 **Australia. *Ore Geol. Rev.*, 80, 838-859, 2017.**  
1520

1521 Kratzmann, D. J., Carey, S., Scasso, R., and Naranjo, J. A.: Compositional variations and magma mixing in the  
1522 1991 eruptions of Hudson volcano, Chile. *B. Volcanol.*, 71, 419-439, DOI:10.1007/s00445-008-0234-x,  
1523 2009.  
1524

1525 Kushiro, I.: The system forsterite-diopside-silica with and without water at high pressures. *Am. J. Sci.*, 267(A),  
1526 269-294, 1969.  
1527

1528 Kushiro, I., and Yoder, H. S., Jr.: Melting of forsterite and enstatite at high pressures and hydrous conditions.  
1529 *Carnegie Inst. Wash. Yrbk.*, 67, 153-158, 1969.  
1530

1531 Lange, R. A., Frey, H. M., and Hector, J.: A thermodynamic model for the plagioclase-liquid  
1532 hygrometer/thermometer. *Am. Mineral.*, 94, 494-506, 2009.  
1533

1534 Langmuir, C. H., and Hanson, G. N.: An evaluation of major element heterogeneity in the mantle sources of  
1535 basalts. *Philos. Tr. R. Soc. S-A*, 297(1431), 383-407, 1980.  
1536

1537 **Latutrie, B., Harris, A., Médard, E., and Gurioli, L.: Eruption and emplacement dynamics of a thick trachytic**  
1538 **lava flow of the Sancy volcano (France). *Bulletin of Volcanology*, 79(1), 4, 2017.**  
1539

1540 Laumonier, M., Scaillet, B., Arbaret, L., and Champallier, R.: Experimental simulation of magma mixing at high  
1541 pressure. *Lithos*, 196, 281-300, 2014.  
1542

1543 Le Maitre, R. W., Streckeisen, A., Zanettin, B., Le Bas, M. J., Bonin, B., Bateman, P., Bellieni, G., Dudek, A.,  
1544 Efremova, S., Keller, J., Lameyre, J., Sabine, P. A., Schmid, R., Sørensen, H., Woolley, A. R.: *Igneous Rocks.*

- 1545 A Classification and Glossary of terms. Recommendations of the IUGS Subcommittee on the  
 1546 Systematics of Igneous Rocks, Cambridge University Press, pp. 236, 2002.  
 1547
- 1548 Lee, C. T. A., Lee, T. C., and Wu, C. T.: Modeling the compositional evolution of recharging, evacuating, and  
 1549 fractionating (REFC) magma chambers: Implications for differentiation of arc magmas. *Geochim.*  
 1550 *Cosmochim. Ac.*, 143, 8-22, 2014.  
 1551
- 1552 Lindsley, D. H.: Pyroxene thermometry. *Am. Mineral.*, 68, 477-493, 1983.  
 1553
- 1554 Lucci, F., Rossetti, F., White, J. C., Moghadam, H. S., Shirzadi, A., and Nasrabad, M.: Tschermak fractionation  
 1555 in calc-alkaline magmas: the Eocene Sabzevar volcanism (NE Iran). *Arab. J. Geosci.*, 9(10), 573, 2016.  
 1556
- 1557 Lucci, F., Rossetti, F., Becchio, R., Theye, T., Gerdes, A., Opitz, J., Baez, W., Bardelli, L., De Astis, G., Viramonte,  
 1558 J., and Giordano, G.: Magmatic Mn-rich garnets in volcanic settings: Age and longevity of the magmatic  
 1559 plumbing system of the Miocene Ramadas volcanism (NW Argentina). *Lithos*, 322, 238-249, 2018.  
 1560
- 1561 MacLennan, J., McKenzie, D., Gronvöld, K., and Slater, L.: Crustal accretion under northern Iceland. *Earth*  
 1562 *Planet. Sc. Lett.*, 191, 295-310, 2001.  
 1563
- 1564 Martinez, M., Fernandez, R., Viquez, R., Vega, R., Reyes, S. A.: Asimilacion del metodo magnetotelurico para  
 1565 la exploracion geotermica. Quinto informe tecnico CICESE-IIE, Mexico, 1983.  
 1566
- 1567 Masotta, M., Mollo, S., Freda, C., Gaeta, M., and Moore, G.: Clinopyroxene–liquid thermometers and  
 1568 barometers specific to alkaline differentiated magmas. *Contrib. Mineral. Petr.*, 166, 1545-1561, 2013.  
 1569
- 1570 Matthews, N. E., Vazquez, J. A., Calvert, A. T.: Age of the Lava Creek supereruption and magma chamber  
 1571 assembly at Yellowstone based on  $^{40}\text{Ar}/^{39}\text{Ar}$  and U-Pb dating of sanidine and zircon crystals. *Geochem.*  
 1572 *Geophys. Geosy.*, 16, 2508–2528, 2015.
- 1573 Melluso, L., Morra, V., Guarino, V., De’Gennaro, R., Franciosi, L., and Grifa, C.: The crystallization of  
 1574 shoshonitic to peralkaline trachyphonolitic magmas in a H<sub>2</sub>O–Cl–F-rich environment at Ischia (Italy), with  
 1575 implications for the feeder system of the Campania Plain volcanoes. *Lithos*, 210, 242-259, 2014.  
 1576
- 1577 Moghadam, H. S., Rossetti, F., Lucci, F., Chiaradia, M., Gerdes, A., Martinez, M. L., Ghorbani, G., and  
 1578 Nasrabad, M.: The calc-alkaline and adakitic volcanism of the Sabzevar structural zone (NE Iran):  
 1579 implications for the Eocene magmatic flare-up in Central Iran. *Lithos*, 248, 517-535, 2016.  
 1580
- 1581 Mollo, S., Del Gaudio, P., Ventura, G., Iezzi, G., and Scarlato, P.: Dependence of clinopyroxene composition  
 1582 on cooling rate in basaltic magmas: implications for thermobarometry. *Lithos*, 118, 302-312, 2010.  
 1583
- 1584 Mordick, B. E., and Glazner, A. F.: Clinopyroxene thermobarometry of basalts from the Coso and Big Pine  
 1585 volcanic fields, California. *Contrib. Mineral. Petr.*, 152, 111-124, 2006.  
 1586
- 1587 Morimoto, N.: Nomenclature of pyroxenes. *Am. Mineral.*, 73, 1123-1133, 1988.  
 1588
- 1589 Morimoto, N.: Nomenclature of pyroxenes. *Mineral. J.*, 14, 198-221, 1989.  
 1590
- 1591 Mutch, E. J. F., Blundy, J. D., Tattitch, B. C., Cooper, F. J., and Brooker, R. A.: An experimental study of  
 1592 amphibole stability in low-pressure granitic magmas and a revised Al-in-hornblende geobarometer.  
 1593 *Contrib. Mineral. Petr.*, 171:85, 1-27, <https://doi.org/10.1007/s00410-016-1298-9>, 2016.  
 1594

1595 Nabelek, P. I., Hofmeister, A. M., and Whittington, A. G.: The influence of temperature-dependent thermal  
1596 diffusivity on the conductive cooling rates of plutons and temperature-time paths in contact aureoles.  
1597 *Earth Planet. Sc. Lett.*, 317, 157-164, 2012.

1598

1599 Nairn, I. A., Kobayashi, T., and Nakagawa, M.: The ~10 ka multiple vent pyroclastic eruption sequence at  
1600 Tongariro Volcanic Centre, Taupo Volcanic Zone, New Zealand: Part 1. Eruptive processes during regional  
1601 extension. *J. Volcanol. Geoth. Res.*, 86, 19-44, 1998.

1602

1603 Nakagawa, M., Nairn, I. A., and Kobayashi, T.: The similar to 10 ka multiple vent pyroclastic eruption sequence  
1604 at Tongariro Volcanic Centre, Taupo Volcanic Zone, New Zealand: Part 2. Petrological insights into  
1605 magma storage and transport during regional extension. *J. Volcanol. Geoth. Res.*, 86, 45-65, 1998.

1606

1607 Namur, O., Charlier, B., Toplis, M. J., and Vander Auwera, J.: Prediction of plagioclase-melt equilibria in  
1608 anhydrous silicate melts at 1-atm. *Contrib. Mineral. Petr.*, 163, 133-150, 2012.

1609

1610 Neave, D. A., Maclennan, J., Hartley, M. E., Edmonds, M., and Thordarson, T.: Crystal storage and transfer in  
1611 basaltic systems: the Skuggafjöll eruption, Iceland. *J. Petrol.*, 55, 2311-2346, 2014.

1612

1613 Negendak, J. F. W., Emmermann, R., Krawczyk, R., Mooser, F., Tobschall, H., and Werle, D.: Geological and  
1614 geochemical investigations on the eastern trans mexican volcanic belt. *Geofis. Int.*, 24, 477-575, 1985.

1615

1616 Nekvasil, H.: Feldspar crystallisation in felsic magmas: a review. *Earth Env. Sci. Tr. So.*, 83(1-2), 399-407, 1992

1617

1618 Norini, G., GropPELLI, G., Sulpizio, R., Carrasco-Núñez, G., Dávila-Harris, P., Pelliccioli, C., Zucca, F., and De  
1619 Franco, R.: Structural analysis and thermal remote sensing of the Los Humeros Volcanic Complex:  
1620 Implications for volcano structure and geothermal exploration. *J. Volcanol. Geoth. Res.*, 301, 221-237,  
1621 2015.

1622

1623 O'Neill, H. S. C. and Jenner, F.: The global pattern of trace element distributions in ocean floor basalts. *Nature*  
1624 491, 698-705, 2012.

1625

1626 Pamukcu, A. S., Gualda, G. A., Bégué, F., and Gravley, D. M.: Melt inclusion shapes: Timekeepers of short-  
1627 lived giant magma bodies. *Geology*, 43, 947-950, 2015.

1628

1629 Patanè, D., De Gori, P., Chiarabba, C., and Bonaccorso, A.: Magma ascent and the pressurization of Mount  
1630 Etna's volcanic system. *Science*, 299, 2061-2063, 2003.

1631

1632 Petrone, C. M., Bugatti, G., Braschi, E., and Tommasini, S.: Pre-eruptive magmatic processes re-timed using a  
1633 non-isothermal approach to magma chamber dynamics. *Nat. Commun.*, 7, 12946, 2016.

1634

1635 Pietruszka, A. J., and Garcia, M. O.: The size and shape of Kilauea Volcano's summit magma storage reservoir:  
1636 a geochemical probe. *Earth Planet. Sc. Lett.*, 167, 311-320, 1999.

1637

1638 Plümpner, O., and Putnis, A.: The complex hydrothermal history of granitic rocks: multiple feldspar  
1639 replacement reactions under subsolidus conditions. *J. Petrol.*, 50(5), 967-987, 2009

1640

1641 Preece, K., Barclay, J., Gertisser, R., and Herd, R. A.: Textural and micro-petrological variations in the eruptive  
1642 products of the 2006 dome-forming eruption of Merapi volcano, Indonesia: implications for sub-surface  
1643 processes. *J. Volcanol. Geoth. Res.*, 261, 98-120, 2013.

1644

1645 Presnall, D. C., Dixon, S. A., Dixon, J. R., O'Donnell, T. H., Brenner, N. L., Schrock, R. L., and Dycus, D. W.:  
 1646 Liquidus phase relations on the join diopside-forsterite-anorthite from 1 atm to 20 kbar: their bearing  
 1647 on the generation and crystallization of basaltic magma. *Contrib. Mineral. Petr.*, 66, 203-220, 1978.  
 1648

1649 Putirka, K.: Magma transport at Hawaii: Inferences based on igneous thermobarometry. *Geology*, 25, 69-72,  
 1650 1997.  
 1651

1652 Putirka, K.: Clinopyroxene+liquid equilibria to 100 kbar and 2450 K. *Contrib. Mineral. Petr.*, 135, 151-163,  
 1653 1999.  
 1654

1655 Putirka, K. D.: Mantle potential temperatures at Hawaii, Iceland, and the mid-ocean ridge system, as inferred  
 1656 from olivine phenocrysts: Evidence for thermally driven mantle plumes. *Geochem. Geophys. Geosy.*, 6,  
 1657 doi:10.1029/2005GC000915, 2005a.  
 1658

1659 Putirka, K. D.: Igneous thermometers and barometers based on plagioclase+ liquid equilibria: Tests of some  
 1660 existing models and new calibrations. *Am. Mineral.*, 90, 336-346, 2005b.  
 1661

1662 Putirka, K. D.: Thermometers and barometers for volcanic systems. *Rev. Mineral. Geochem.*, 69, 61-120,  
 1663 2008.  
 1664

1665 Putirka, K., Johnson, M., Kinzler, R., Longhi, J., and Walker, D.: Thermobarometry of mafic igneous rocks based  
 1666 on clinopyroxene-liquid equilibria, 0–30 kbar. *Contrib. Mineral. Petr.*, 123, 92-108, 1996.  
 1667

1668 Putirka, K., Ryerson, F. J., and Mikaelian, H.: New igneous thermobarometers for mafic and evolved lava  
 1669 compositions, based on clinopyroxene+ liquid equilibria. *Am. Mineral.*, 88, 1542-1554, 2003.  
 1670

1671 Putirka, K. D., Perfit, M., Ryerson, F. J., and Jackson, M. G.: Ambient and excess mantle temperatures, olivine  
 1672 thermometry, and active vs. passive upwelling. *Chem. Geol.*, 241, 177-206, 2007.  
 1673

1674 Redman, B. A., and Keays, R. R.: Archaean basic volcanism in the eastern Goldfields province, Yilgarn Block,  
 1675 western Australia. *Precambrian Res.*, 30, 113-152, 1985.  
 1676

1677 **Renjith, M. L.: Micro-textures in plagioclase from 1994–1995 eruption, Barren Island Volcano: evidence of**  
 1678 **dynamic magma plumbing system in the Andaman subduction zone. *Geosci. Front.*, 5(1), 113-126, 2014.**  
 1679

1680 Reubi, O., and Nicholls, I. A.: Magmatic evolution at Batur volcanic field, Bali, Indonesia: petrological evidence  
 1681 for polybaric fractional crystallization and implications for caldera-forming eruptions. *J. Volcanol. Geoth.*  
 1682 *Res.*, 138, 345-369, 2004.  
 1683

1684 Rhodes, J. M., Dungan, M. A., Blanchard, D. P., and Long, P. E.: Magma mixing at mid-ocean ridges: evidence  
 1685 from basalts drilled near 22 N on the Mid-Atlantic Ridge. *Tectonophysics*, 55, 35-61, 1979.  
 1686

1687 Rivera, T. A., Schmitz, M. D., Crowley, J. L., and Storey, M.: Rapid magma evolution constrained by zircon  
 1688 petrochronology and <sup>40</sup>Ar/<sup>39</sup>Ar sanidine ages for the Huckleberry Ridge Tuff, Yellowstone, USA, *Geology*,  
 1689 42, 643-646, 2014.  
 1690

1691 Roeder, P. L., and Emslie, R.: Olivine-liquid equilibrium. *Contrib. Mineral. Petr.*, 29, 275-289, 1970.  
 1692

1693 Rojas-Ortega, E.: Litoestratigrafía, petrografía y geoquímica de la toba Llano, y su relación con el cráter el  
 1694 Xalapazco, Caldera de LosHumeros, Puebla. MS Thesis, IPICYT, San Luis Potosí, México, pp. 129, 2016.  
 1695

1696 Romo-Jones, J. M., Gutiérrez-Negrín, L. C. A., Flores-Armenta, M., Del Valle, J. L., and García, A: Mexico, in:  
1697 2017 Annual Report, IEA Geothermal, 66–72, available at:  
1698 <https://drive.google.com/file/d/1ztLIE5MFdLwSndR7iLmAkMXnQth4c86T/view>, 2017.  
1699

1700 Rutherford, M. J.: Magma ascent rates. *Rev. Mineral. Geochem.*, 69(1), 241-271, 2008.  
1701

1702 Rutherford, M. J., and Gardner, J. E.: Rates of magma ascent. *Encyclopedia of Volcanoes*, 207-217, 2000.  
1703

1704 Rutherford, M. J., Sigurdsson, H., Carey, S., and Davis, A.: The May 18, 1980, eruption of Mount St. Helens: 1.  
1705 Melt composition and experimental phase equilibria. *J. Geophys. Res-Sol. Ea.*, 90(B4), 2929-2947, 1985.  
1706

1707 Sano, T., and Yamashita, S.: Experimental petrology of basement lavas from Ocean Drilling Program Leg 192:  
1708 implications for differentiation processes in Ontong Java Plateau magmas. *Geol. Soc. Spec. Publ.*, 229(1),  
1709 185-218, 2004.  
1710

1711 Scott, J. A., Mather, T. A., Pyle, D. M., Rose, W. I., and Chigna, G.: The magmatic plumbing system beneath  
1712 Santiaguito Volcano, Guatemala. *J. Volcanol. Geoth. Res.*, 237, 54-68, 2012.  
1713

1714 Shane, P., and Coote, A.: Thermobarometry of Whangarei volcanic field lavas, New Zealand: Constraints on  
1715 plumbing systems of small monogenetic basalt volcanoes. *J. Volcanol. Geoth. Res.*, 354, 130-139, 2018.  
1716

1717 Sigmarsson, O., Vlastélic, I., Andreasen, R., Bindeman, I., Devidal, J. L., Moune, S., Keiding, J. K., Larsen, G.,  
1718 Hoskuldsson, A., and Thordarson, T.: Dynamic magma mixing revealed by the 2010 Eyjafjallajökull  
1719 eruption. *Solid Earth Discussions*, 3, 591-613, 2011.  
1720

1721 Sisson, T. W., and Grove, T. L.: Temperatures and H<sub>2</sub>O contents of low-MgO high-alumina basalts. *Contrib.*  
1722 *Mineral. Petr.*, 113, 167-184, 1993.  
1723

1724 Sisson, T. W., and Layne, G. D.: H<sub>2</sub>O in basalt and basaltic andesite glass inclusions from four subduction-  
1725 related volcanoes. *Earth Planet. Sc. Lett.*, 117, 619-635, 1993.  
1726

1727 Smith, R. L., and Shaw, H. R.: Igneous-related geothermal systems. US Geological Survey Circular 726, 58-83,  
1728 1975.  
1729

1730 Solano, J. M. S., Jackson, M. D., Sparks, R. S. J., and Blundy, J.: Evolution of major and trace element  
1731 composition during melt migration through crystalline mush: implications for chemical differentiation  
1732 in the crust. *Am. J. Sci.*, 314(5), 895-939, 2014.  
1733

1734 Sparks, R. S. J.: The dynamics of bubble formation and growth in magmas: a review and analysis. *J. Volcanol.*  
1735 *Geoth. Res.*, 3(1-2), 1-37, 1978.  
1736

1737 Sparks, R. S. J., Young, S. R., Barclay, J., Calder, E. S., Cole, P., Darroux, B., Davies, M. A., Druitt, T. H., Harford,  
1738 C., Herd, R., James, M., Lejeune, A. M., Loughliun, S., Norton, G., Skerrit, G., Stasiuk, M. V., Stevens, N.  
1739 S., Toothill, J., Wadge, G., and Watts, R.: Magma production and growth of the lava dome of the  
1740 Soufriere Hills Volcano, Montserrat, West Indies: November 1995 to December 1997. *Geophys. Res.*  
1741 *Lett.*, 25(18), 3421-3424, 1998.  
1742

1743 Streck, M. J.: Mineral textures and zoning as evidence for open system processes. *Rev. Mineral. Geochem.*,  
1744 69(1), 595-622, 2008  
1745

1746 Stroncik, N. A., Klügel, A., and Hansteen, T. H.: The magmatic plumbing system beneath El Hierro (Canary  
1747 Islands): constraints from phenocrysts and naturally quenched basaltic glasses in submarine rocks.  
1748 Contrib. Mineral. Petr., 157, 593-607, DOI:10.1007/s00410-008-0354-5, 2009.  
1749

1750 Suter, M.: Structural traverse across the Sierra Madre Oriental fold-thrust belt in east-central Mexico. Geol.  
1751 Soc. Am. Bull., 98(3), 249-264, 1987.  
1752

1753 Takahashi, E.: Melting of a dry peridotite KLB-1 up to 14 GPa: Implications on the origin of peridotitic upper  
1754 mantle. J. Geophys. Res-Sol. Ea., 91(B9), 9367-9382, 1986.  
1755

1756 Thompson, R. N.: Primary basalts and magma genesis. Contrib. Mineral. Petr., 45, 317-341, 1974.  
1757

1758 Troll, V. R., Deegan, F. M., Jolis, E. M., Harris, C., Chadwick, J. P., Gertisser, R., Schwarzkopf, L. M., Borisova,  
1759 A., Bindeman, I. N., Sumarti, S., and Preece, K.: Magmatic differentiation processes at Merapi Volcano:  
1760 inclusion petrology and oxygen isotopes. J. Volcanol. Geoth. Res., 261, 38-49, 2013.  
1761

1762 Ubide, T., Gale, C., Arranz, E., Lago, M., and Larrea, P.: Clinopyroxene and amphibole crystal populations in a  
1763 lamprophyre sill from the Catalonian Coastal Ranges (NE Spain): a record of magma history and a  
1764 window to mineral-melt partitioning. Lithos, 184, 225-242, 2014.  
1765

1766 Urbani, S., Giordano, G., Lucci, F., Rossetti, F., Acocella, V., and Carrasco-Núñez, G.: Estimating the depth and  
1767 evolution of intrusions at resurgent calderas: Los Humeros (Mexico), Solid Earth Discuss.,  
1768 <https://doi.org/10.5194/se-2019-100>, in review, 2019.  
1769

1770 Ushioda, M., Takahashi, E., Hamada, M., and Suzuki, T.: Water content in arc basaltic magma in the Northeast  
1771 Japan and Izu arcs: an estimate from Ca/Na partitioning between plagioclase and melt. Earth Planets  
1772 Space, 66(1), 127, 2014.  
1773

1774 Verma, S. P.: Magma genesis and chamber processes at Los Humeros caldera, Mexico—Nd and Sr isotope  
1775 data. Nature, 302(5903), 52, 1983.  
1776

1777 Verma, S. P.: Alkali and alkaline earth element geochemistry of Los Humeros caldera, Puebla, Mexico. J.  
1778 Volcanol. Geoth. Res., 20, 21–40, 1984.  
1779

1780 Verma, S. P.: Heat source in Los Humeros geothermal area, Puebla, Mexico. Geoth. Res. T., 9, 521-525, 1985a.  
1781

1782 Verma, S. P.: On the magma chamber characteristics as inferred from surface geology and geochemistry:  
1783 examples from Mexican geothermal areas. Phys. Earth Planet. In., 41, 207-214, 1985b.  
1784

1785 Verma, S. P.: Geochemical evidence for a lithospheric source for magmas from Los Humeros caldera, Puebla,  
1786 Mexico. Chem. Geol., 164, 35-60, 2000.  
1787

1788 Verma, S. P., and López, M.: Geochemistry of Los Humeros caldera, Puebla, Mexico. B. Volcanol., 45, 63-79,  
1789 1982.  
1790

1791 Verma M. P., Verma, S. P. and Sanvincente, H.: Temperature field simulation with stratification model of  
1792 magma chamber under Los Humeros caldera, Puebla, Mexico. Geothermics, 19, 187-197, 1990.  
1793

1794 Verma, S. P., and Andaverde, J.: Temperature field distribution from cooling of a magma chamber. Proceeding  
1795 World Geothermal Congress, 1119-1121, 1995.  
1796



- 1797 Verma, S. P., Gomez-Arias, E. and Andaverde J.: Thermal sensitivity analysis of emplacement of the magma  
1798 chamber in Los Humeros caldera, Puebla, Mexico. *Int. Geol. Rev.*, 53, 905-925, 2011.  
1799
- 1800 Verma, S. P. and Gomez-Arias, E.: Three-dimensional temperature field simulation of magma chamber in the  
1801 Los Humeros geothermal field, Puebla, Mexico. *Appl. Therm. Eng.*, 52, 512-515, 2013.  
1802
- 1803 Viccaro, M., Calcagno, R., Garozzo, I., Giuffrida, M., and Nicotra, E.: Continuous magma recharge at Mt. Etna  
1804 during the 2011–2013 period controls the style of volcanic activity and compositions of erupted lavas.  
1805 *Miner. Petrol.*, 109, 67-83, 2015.  
1806
- 1807 Viccaro, M., Barca, D., Bohrsen, W. A., D'Oriano, C., Giuffrida, M., Nicotra, E., and Pitcher, B. W.: Crystal  
1808 residence times from trace element zoning in plagioclase reveal changes in magma transfer dynamics at  
1809 Mt. Etna during the last 400 years. *Lithos*, 248, 309-323, 2016.  
1810
- 1811 Viniegra-Osorio, F.: Geología del Macizo de Teziutlán y la Cuenca Cenozoica de Veracruz. *Asoc. Mex. Geólogos*  
1812 *Petroleros Bol.*, 17, 101-163, 1965.  
1813
- 1814 Wagner, T. P., Donnelly-Nolan, J. M., and Grove, T. L.: Evidence of hydrous differentiation and crystal  
1815 accumulation in the low-MgO, high-Al<sub>2</sub>O<sub>3</sub> lake basalt from Medicine Lake volcano, California. *Contrib.*  
1816 *Mineral. Petr.*, 121, 201-216, 1995.  
1817
- 1818 Wallace, P., and Anderson, A. T. Jr.: Volatiles in Magmas. *Encyclopedia of Volcanoes*, 149–170, 2000.  
1819
- 1820 Waters, L. E., and Lange, R. A.: An updated calibration of the plagioclase-liquid hygrometer-thermometer  
1821 applicable to basalts through rhyolites. *Am. Mineral.*, 100, 2172-2184, 2015.  
1822
- 1823 Webster, J. D., Kinzler, R. J., and Mathez, E. A.: Chloride and water solubility in basalt and andesite melts and  
1824 implications for magmatic degassing. *Geochim. Cosmochim. Ac.*, 63(5), 729-738, 1999.  
1825
- 1826 Welsch, B., Faure, F., Famin, V., Baronnet, A., and Bachèlery, P.: Dendritic crystallization: A single process for  
1827 all the textures of olivine in basalts? *J. Petrol.*, 54, 539-574, 2013.  
1828
- 1829 White, J. C., Parker, D. F., and Ren, M.: The origin of trachyte and pantellerite from Pantelleria, Italy: insights  
1830 from major element, trace element, and thermodynamic modelling. *J. Volcanol. Geoth. Res.*, 179, 33-  
1831 55, 2009.  
1832
- 1833 Whitney, D. L., and Evans, B. W.: Abbreviations for names of rock-forming minerals. *Am. Mineral.*, 95(1), 185-  
1834 187, 2010.  
1835
- 1836 Wilcox, C.: Eruptive, Magmatic and Structural Evolution of a Large Explosive Caldera Volcano: Los Humeros  
1837 México. PhD Thesis. University of Leicester, UK, pp. 485, 2011.  
1838
- 1839 Wohletz, K., Civetta, L., and Orsi, G.: Thermal evolution of the Phlegraean magmatic system. *J. Volcanol.*  
1840 *Geoth. Res.*, 91, 381-414, 1999.  
1841
- 1842 Wood, B. J.: The solubility of alumina in orthopyroxene coexisting with garnet. *Contrib. Mineral. Petr.*, 46(1),  
1843 1-15, 1974.  
1844
- 1845 Wotzlaw, J. R.-F., Bindeman, I. N., Watts, K. E., Schmitt, A. K., Caricchi, L. and Schaltegger, U.: Linking rapid  
1846 magma reservoir assembly and eruption trigger mechanisms at evolved Yellowstone type  
1847 supervolcanoes. *Geology*, 42, 807–810, 2014.  
1848

- 1849 Wright, T. L., and Fiske, R. S.: Origin of the differentiated and hybrid lavas of Kilauea volcano, Hawaii. *J. Petrol.*,  
1850 12, 1-65, 1971.  
1851
- 1852 Yáñez, C., and García, S.: Exploración de la región geotérmica Los Humeros-Las Derrumbadas, Estados de  
1853 Puebla y Veracruz, C.F.E. Mexico, Internal Report, 1-96, 1982.
- 1854 Yang, H. J., Kinzler, R. J., and Grove, T. L.: Experiments and models of anhydrous, basaltic olivine-plagioclase-  
1855 augite saturated melts from 0.001 to 10 kbar. *Contrib. Mineral. Petr.*, 124, 1-18, 1996.  
1856
- 1857 Yang, H. J., Frey, F. A., Clague, D. A., and Garcia, M. O.: Mineral chemistry of submarine lavas from Hilo Ridge,  
1858 Hawaii: implications for magmatic processes within Hawaiian rift zones. *Contrib. Mineral. Petr.*, 135,  
1859 355-372, 1999.  
1860
- 1861 Zhang, J., Davidson, J. P., Humphreys, M. C. S., Macpherson, C. G., and Neill, I.: Magmatic enclaves and  
1862 andesitic lavas from Mt. Lamington, Papua New Guinea: implications for recycling of earlier-fractionated  
1863 minerals through magma recharge. *J. Petrol.*, 56, 2223-2256, 2015.  
1864
- 1865 Zheng, J., Mao, J., Chai, F., and Yang, F.: Petrogenesis of Permian A-type granitoids in the Cihai iron ore district,  
1866 Eastern Tianshan, NW China: Constraints on the timing of iron mineralization and implications for a non-  
1867 plume tectonic setting. *Lithos*, 260, 371-383, 2016.  
1868
- 1869 Zhu, Y., and Ogasawara, Y.: Clinopyroxene phenocrysts (with green salite cores) in trachybasalts: implications  
1870 for two magma chambers under the Kokchetav UHP massif, North Kazakhstan. *J. Asian Earth Sci.*, 22,  
1871 517-527, 2004.  
1872  
1873

1874 **SUPPLEMENTARY MATERIALS**

1875 *Supplementary Tables S1: Feldspar, EMPA complete dataset.*

1876 *Supplementary Table S2: Clinopyroxene, EMPA complete dataset.*

1877 *Supplementary Table S3: Olivine, EMPA complete dataset.*

1878 *Supplementary Table S4: Orthopyroxene, EMPA complete dataset.*

1879 *Supplementary Table S5: Opaque Minerals and Spinel, EMPA complete dataset.*

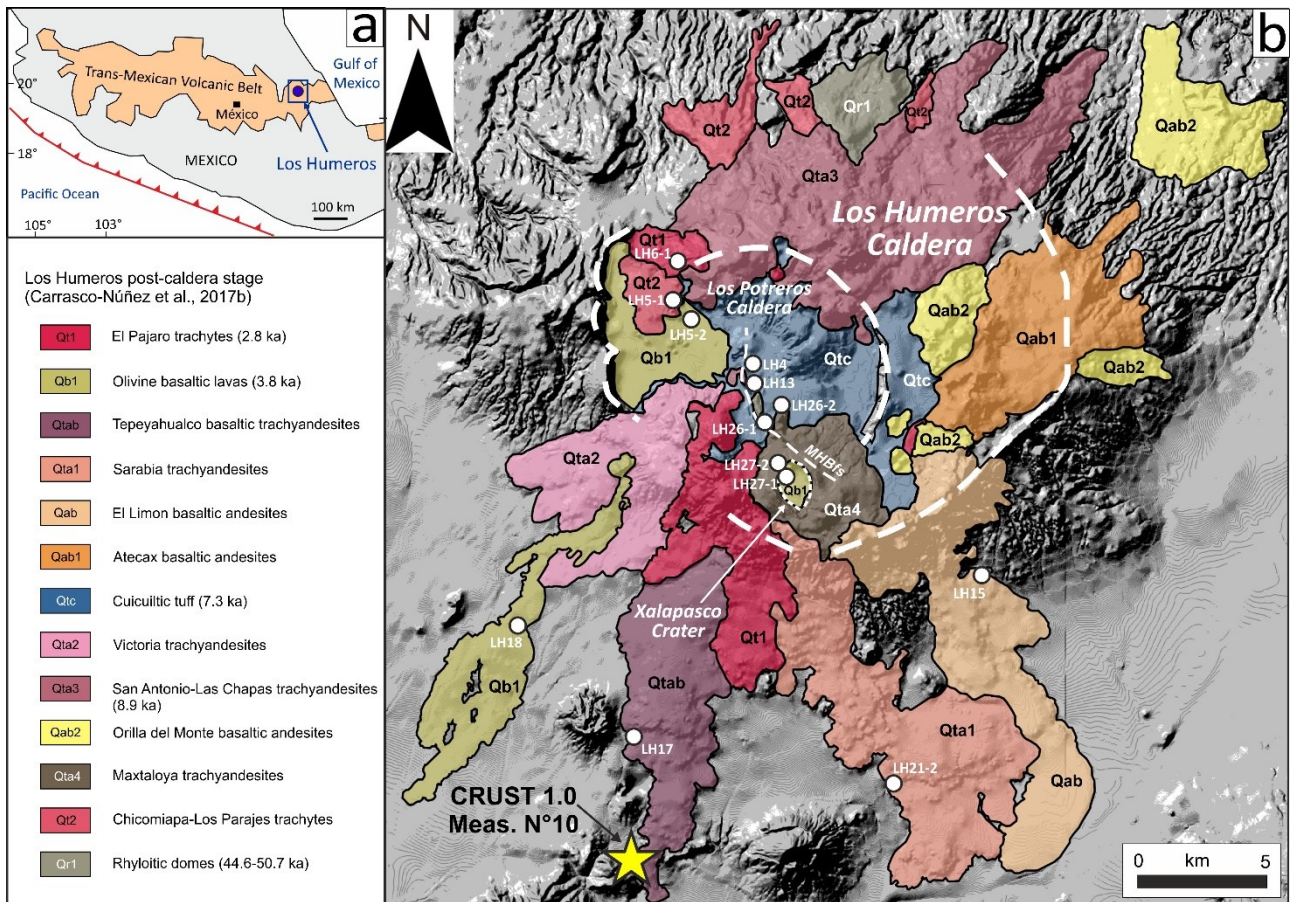
1880 *Supplementary Table S6: Major-Elements Mass-Balance Models.*

1881

1882

1883 FIGURES

1884 Figure 1



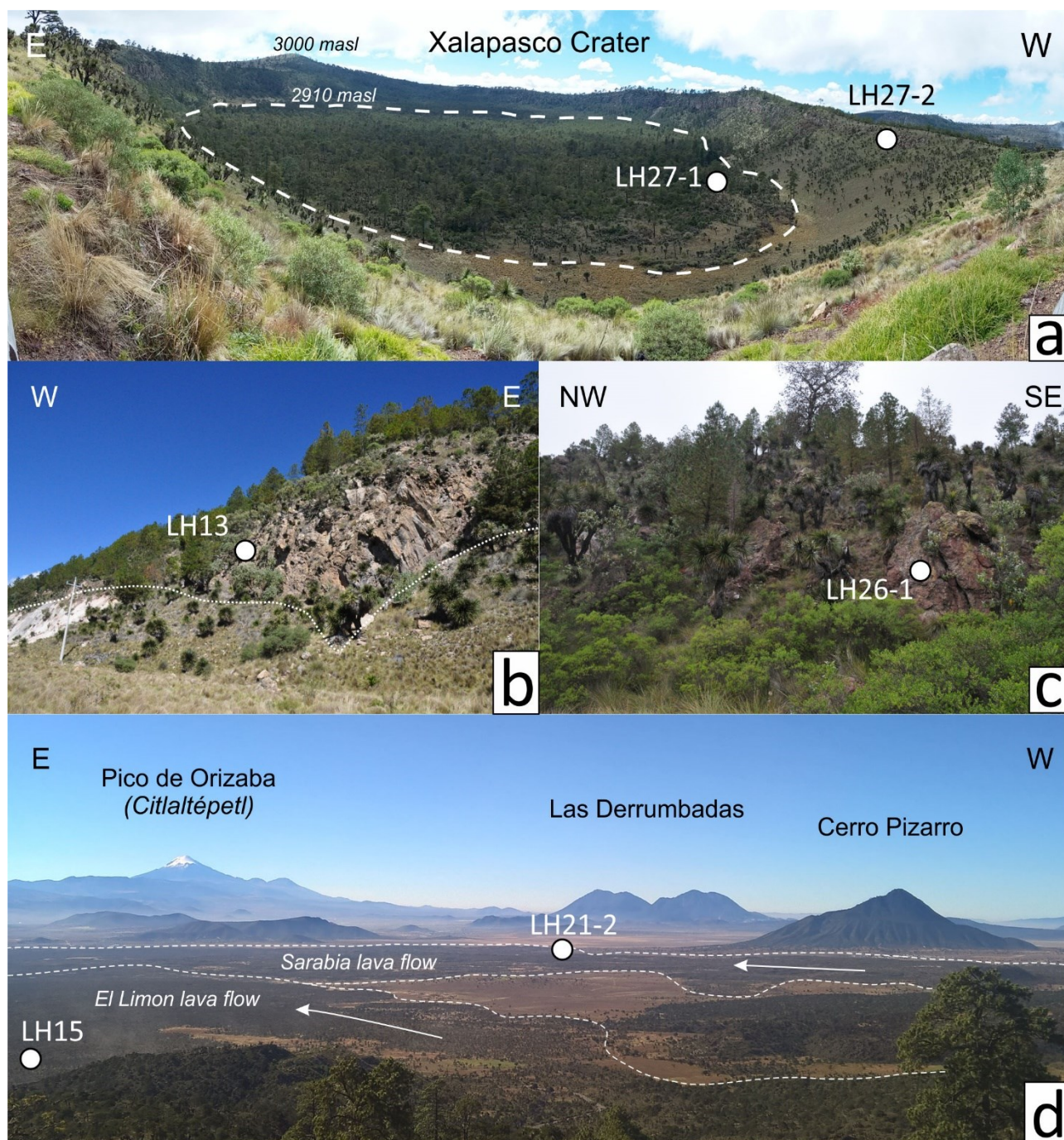
1885

1886 **Figure-1.** Geological Context. (a) The Los Humeros volcanic complex (LHVC, blue dot) with respect to the  
1887 Trans-Mexican Volcanic Belt (TMVB). (b) Shaded relief image obtained from 15 m resolution digital elevation  
1888 model (DEM) of the LHVC. Volcanic products of the Los Humeros post-caldera stage are redrawn from  
1889 Carrasco-Núñez et al. (2017b). The description of the volcanic units, their names and abbreviations follow  
1890 Carrasco et al. (2017b). The map shows location (white dots) and volcanological significance of the samples  
1891 used in this study. The yellow star indicates the locality of the measure N°10 of the Crust 1.0 global model  
1892 (Dziewonski and Anderson, 1981; Davies, 2013).

1893

1894

Figure 2



1896

1897

1898

1899

1900

1901

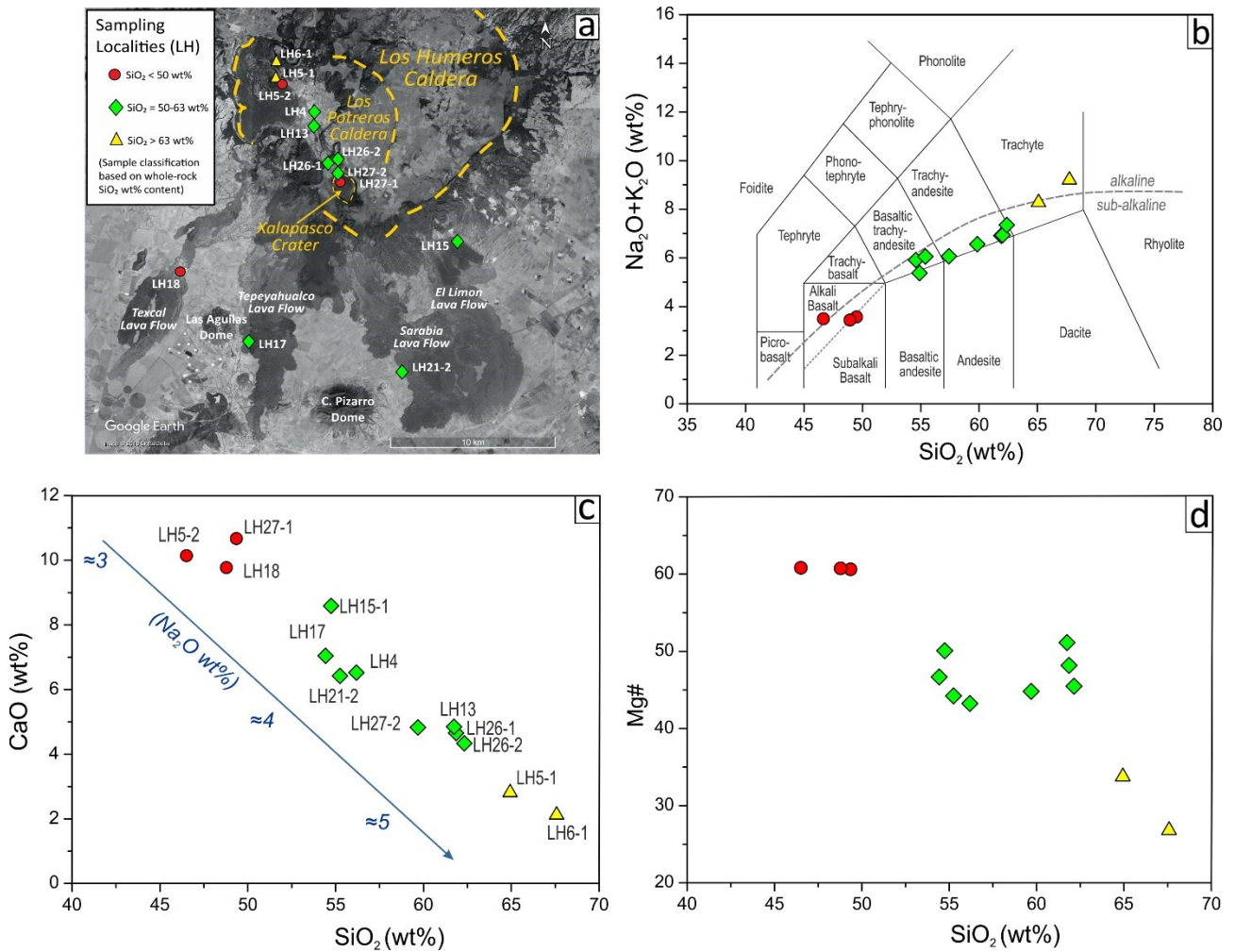
1902

1903

1904

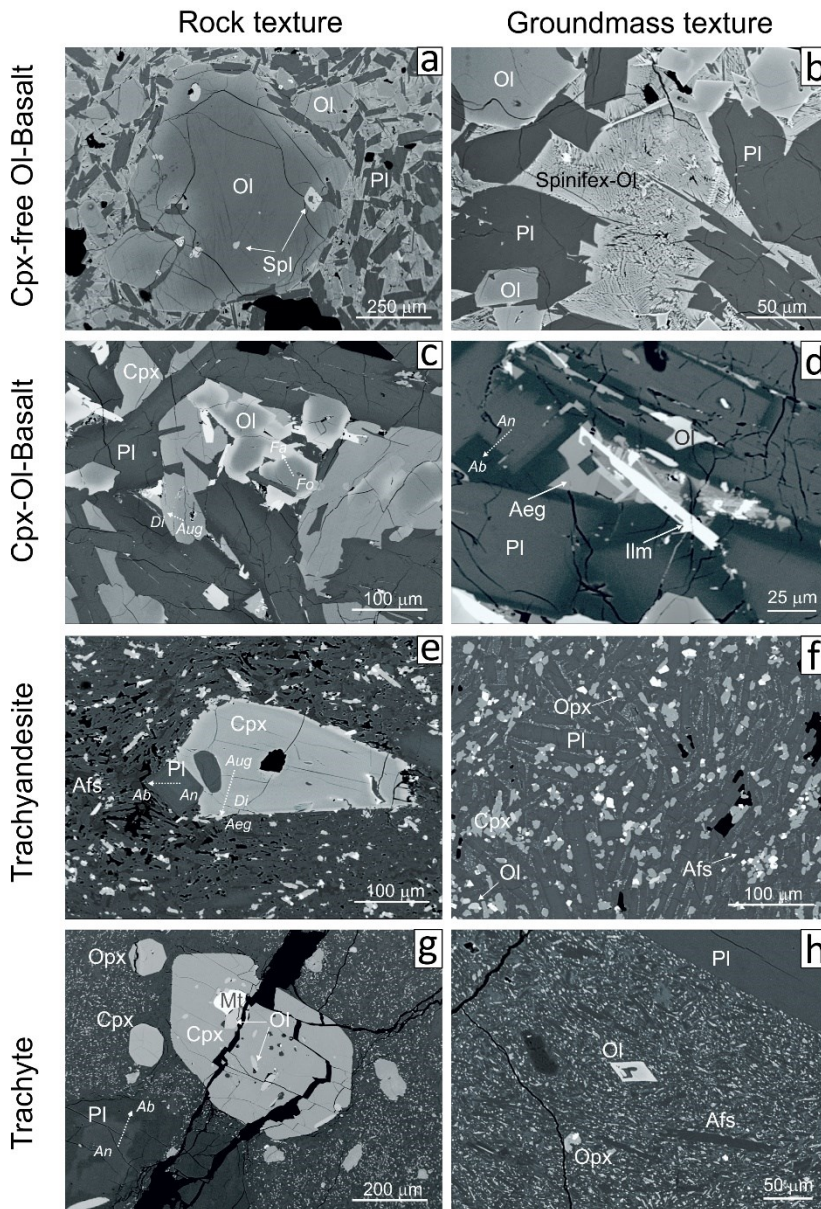
1905

**Figure-2.** Field photographs of LHPCS volcanic products. (a) E-W panoramic view of Xalapasco crater; the white dashed line indicates the limit of **Cpx-bearing** OI-basalts lavas filling the crater. (b) **Intra-caldera** trachyandesitic lavas outcropping at Los Potreros, south to Los Humeros town. (c) Trachyandesitic lava-dome outcropping inside Los Potreros caldera, north to Xalapasco crater. (d) E-W panoramic view from the SE Los Humeros caldera rim. With dashed lines are indicated the two major trachyandesitic lava flows of “El Limón” and “Sarabia”. Pico de Orizaba, Las Derrumbadas and Cerro Pizarro volcanoes are also indicated. **White dots indicate** sampling localities.



1907  
 1908 **Figure-3.** (a) Satellite image of the LHVC (Image Landsat from Google Earth Pro, 2018 Digital Globe; courtesy  
 1909 of Google) with localization of samples selected for the application of Rayleigh Fractional Crystallization  
 1910 model and for thermobarometry models. (b) Total alkali versus silica (TAS) diagram (Le Maitre et al., 2002).  
 1911 (c-d) Major elements selected Harker diagrams for LHPCS studied lavas. The different symbols (circle for  
 1912 basalt, diamond for trachyandesite and triangle for trachyte) represent the graphic code that will be used  
 1913 coherently along the manuscript.

1914  
 1915

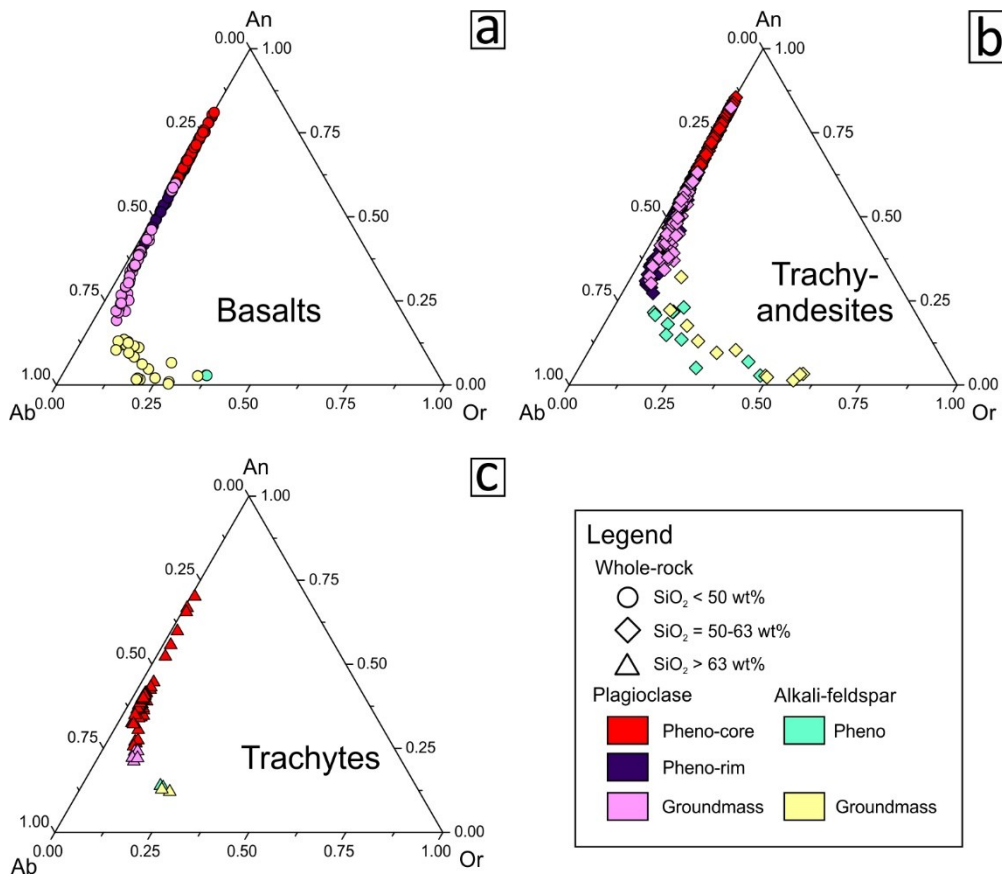


1917

1918 **Figure-4.** Microtextures and fabrics of the LHPCS lavas. (a) Back-scattered electrons (BSE) image of the Cpx-  
 1919 free Ol-basalt fabric, dominated by euhedral unzoned **homogeneous** Pl+Ol, with major olivine phenocryst  
 1920 characterized by Cr-Spl inclusions. (b) BSE image of Cpx-free Ol-basalt groundmass highlighting the spinifex  
 1921 to skeletal and dendritic crystallization of olivine, **associated to the swallow-tailed morphology of plagioclase.**  
 1922 (c) BSE image of Cpx-bearing Ol-basalt. **Normal monotonous zoning at rim** is observed for **all the main** mineral  
 1923 phases (Pl+Ol+Cpx). (d) BSE image of Cpx-bearing Ol-basalt groundmass characterized by albitic plagioclase,  
 1924 aegirine-pyroxene, Fe-rich olivine and ilmenite. (e-f) BSE images of trachyandesites. It is possible to observe  
 1925 a microcrystalline groundmass where major phenocrysts of Cpx and Pl are dispersed. (g-h) BSE images of  
 1926 trachytes, characterized by a microcrystalline groundmass and Pl+Cpx+Opx phenocryst. **Plagioclase**  
 1927 **phenocrysts show normal monotonous to normal step zoning.** Major Cpx phenocrysts present inclusion of  
 1928 Ol+Mt.

1929

1930 **Figure 5**



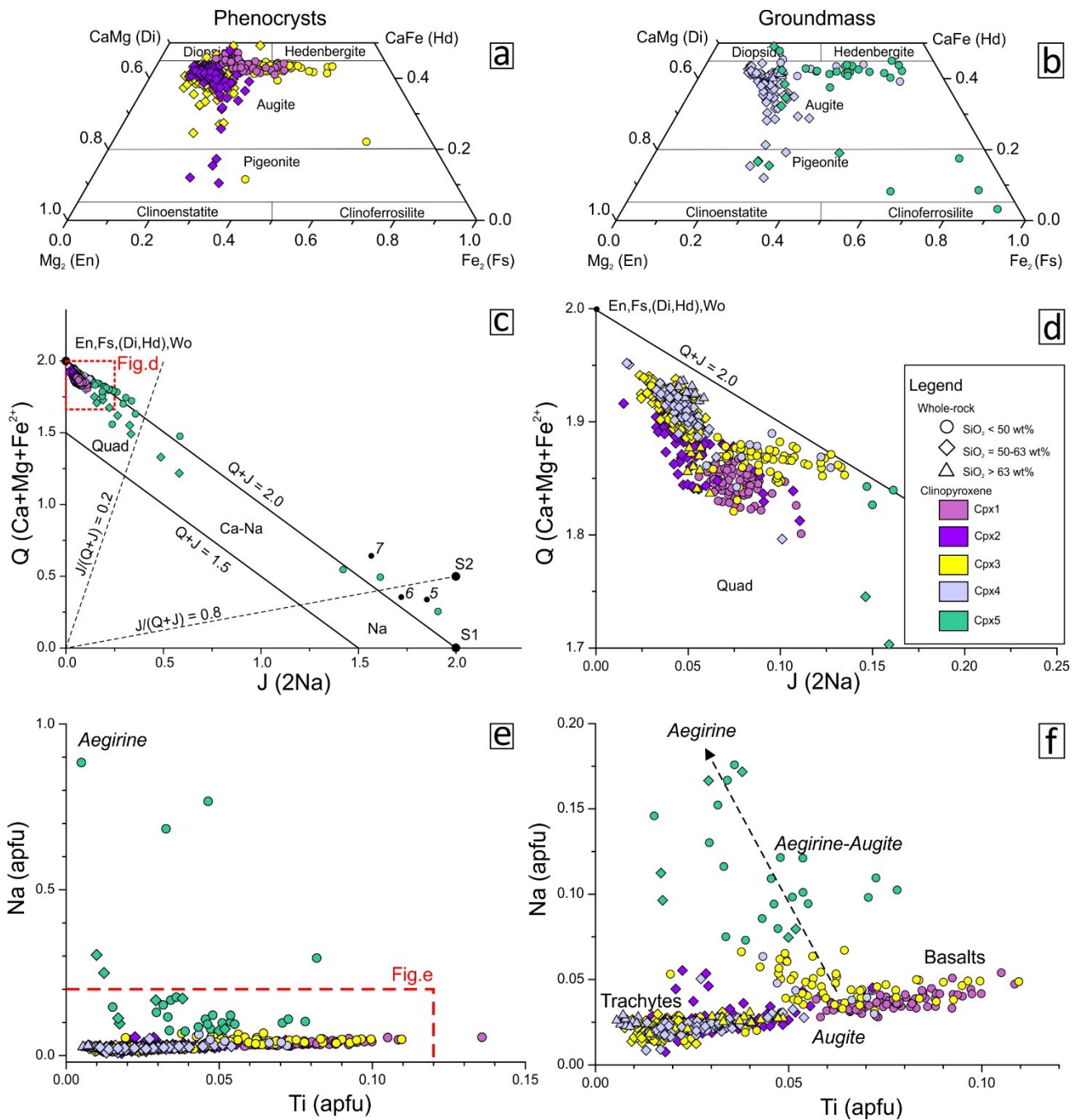
1931

1932 **Figure-5.** An-Ab-Or diagrams showing the composition of feldspar in (a) basalts (circles), (b) trachyandesites

1933 (diamonds) and (c) trachytes (triangles) of LHPCS lavas.

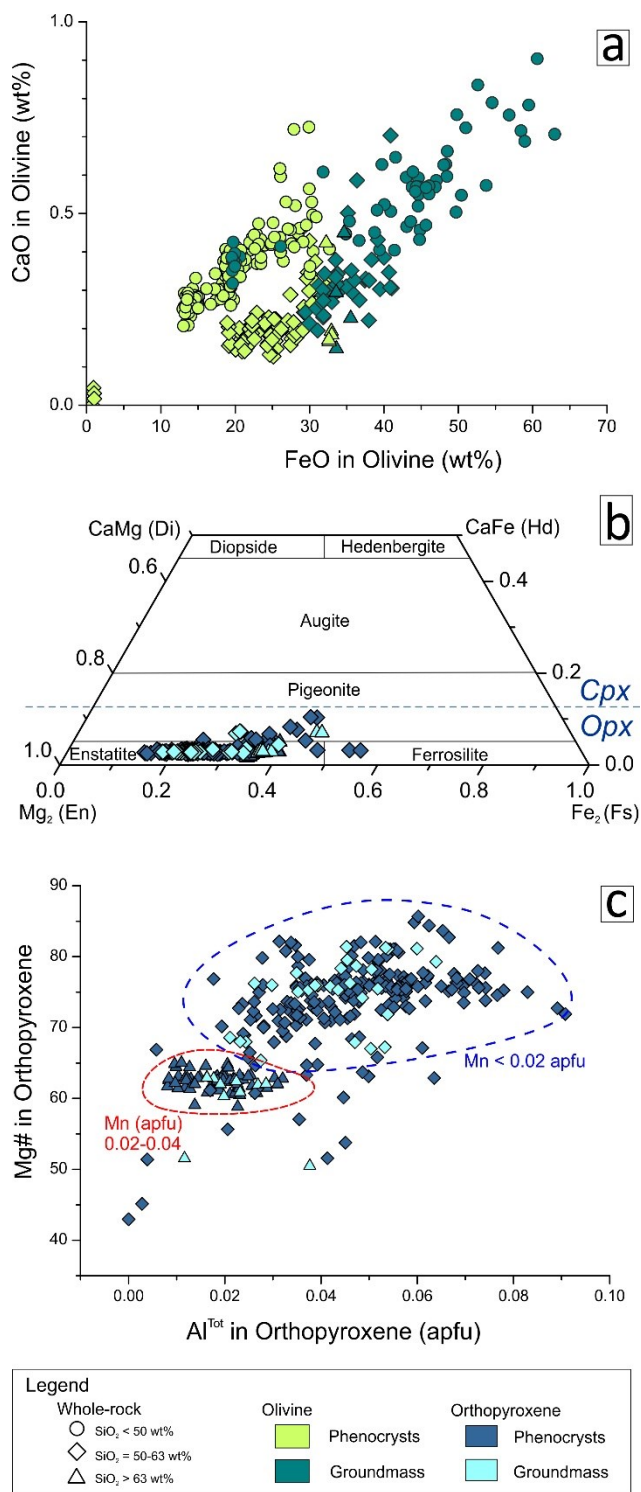
1934





1936  
 1937 **Figure-6.** Di-Hd-En-Fs, Q-J and Ti vs. Na diagrams showing the composition of clinopyroxenes in LHPCS lavas.  
 1938 Symbol shapes follow Fig. 3. (a) Di-Hd-En-Fs diagram for clinopyroxene phenocrysts (Cpx1, Cpx2, Cpx3). (b)  
 1939 Di-Hd-En-Fs diagram for clinopyroxene microlites (Cpx4) and Na-clinopyroxenes (Cpx5). (c) Q-J diagram for  
 1940 pyroxenes with indication of **endmembers** (Morimoto, 1989). (d) Enlargement of area indicated in (c). (e) Ti  
 1941 vs. Na (apfu) diagram illustrating the compositional differences between clinopyroxenes. (f) Enlargement of  
 1942 area indicated in (e), showing the main Augite trend characterizing the evolution from basalts to trachytes  
 1943 and the **divergent trend** of Aegirine-Augite and Aegirine series.

1945 **Figure 7**

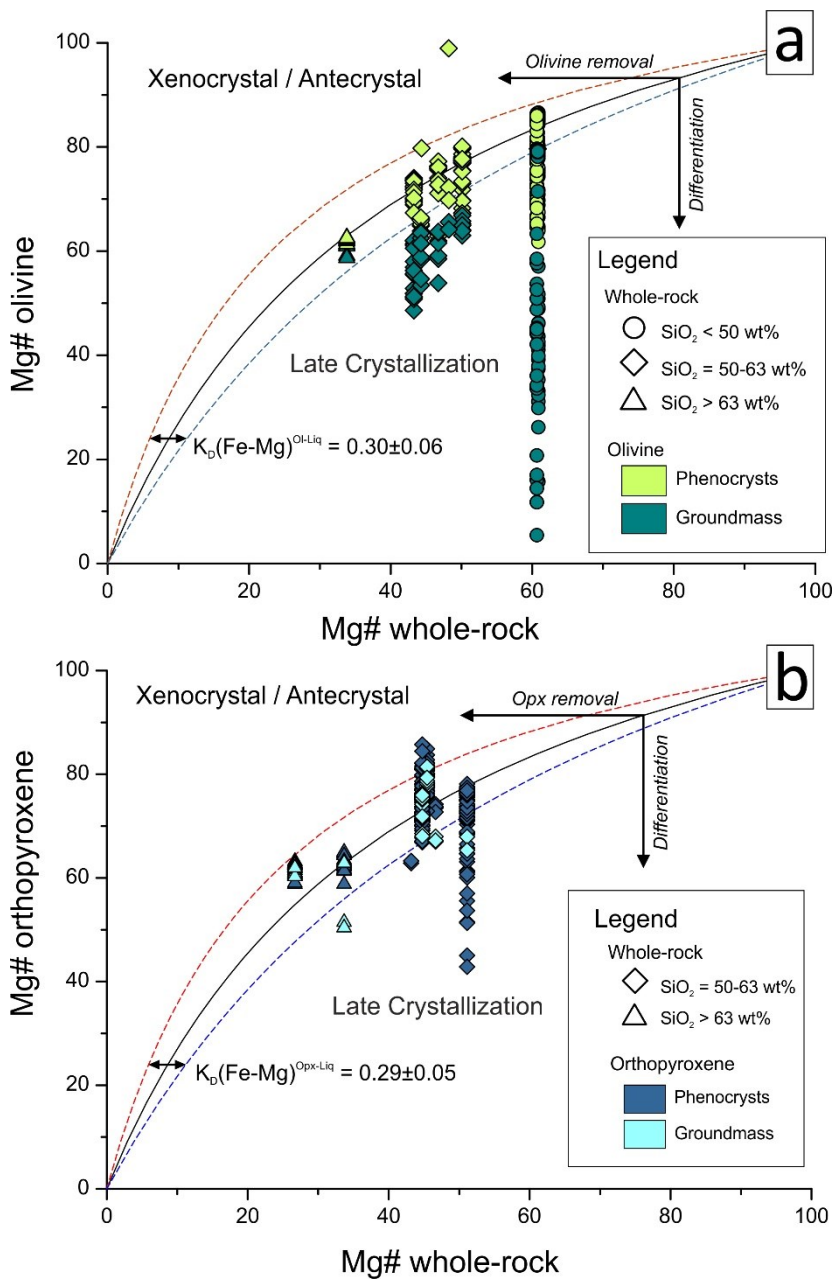


1946

1947 **Figure-7.** (a) CaO vs. FeO diagram showing the composition of olivine in LHPCS lavas. (b) Di-Hd-En-Fs diagram  
 1948 showing the orthopyroxene chemistry in LHPCS studied lavas. (c) Al vs. Mg# diagram showing the main  
 1949 compositional differences between orthopyroxene populations from trachytes and trachyandesites. Mn  
 1950 (apfu) contents are also reported for the two populations.

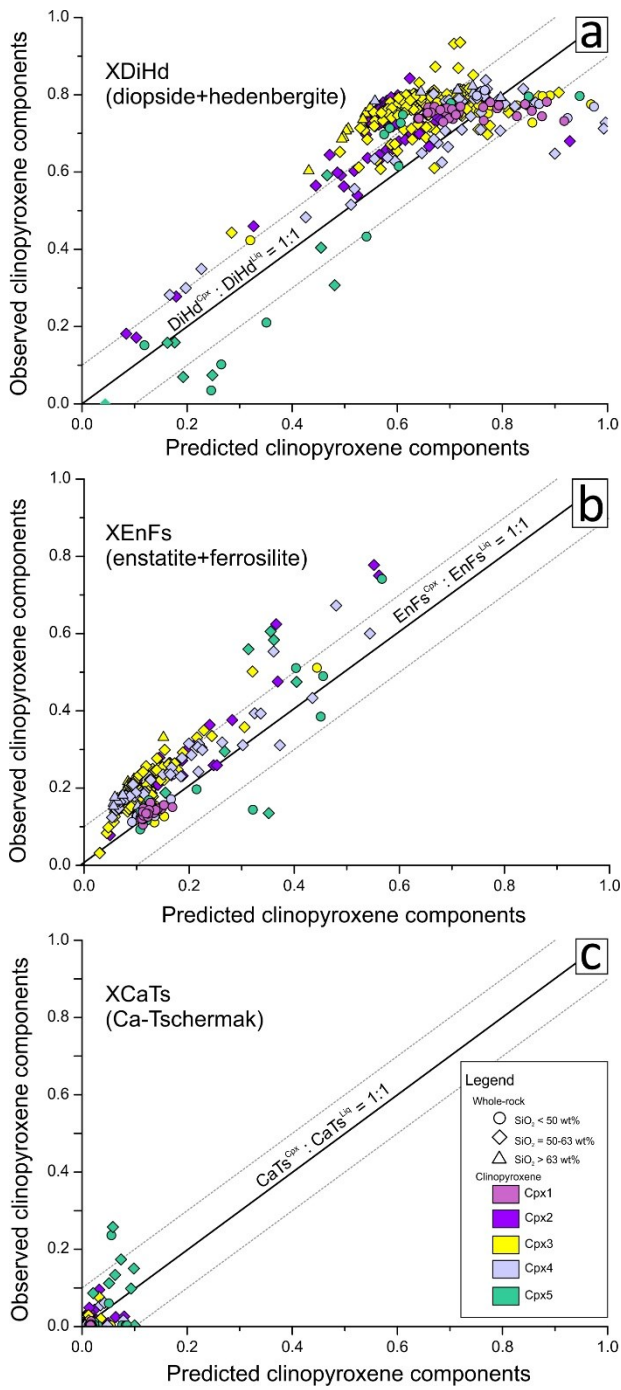
1951

1952



1954  
 1955 **Figure-8.** Rhodes diagrams showing the results of test of equilibrium liquid and olivine (a) and orthopyroxene  
 1956 (b). The partitioning of Fe-Mg between mineral and liquid (Fe-Mg exchange coefficient) or  $K_D^{\text{min-liq}}(\text{Fe-Mg})$  is  
 1957 shown (black lines). The accepted range of equilibrium constant values for both figures (a) and (b) is indicated  
 1958 by dashed lines.  $K_D^{\text{min-liq}}(\text{Fe-Mg})$  values are from Putirka (2008). **Nominal melt compositions are selected from**  
 1959 **whole-rock analyses.** Vectors of olivine and orthopyroxene removal from melt and closed system  
 1960 differentiation are redrawn after Putirka (2008 and references therein). Fields of Xenocrystal/Antecrystals  
 1961 and Late Crystallization are also indicated. Symbols and colors refer to Fig. 7.

1962  
 1963



1965

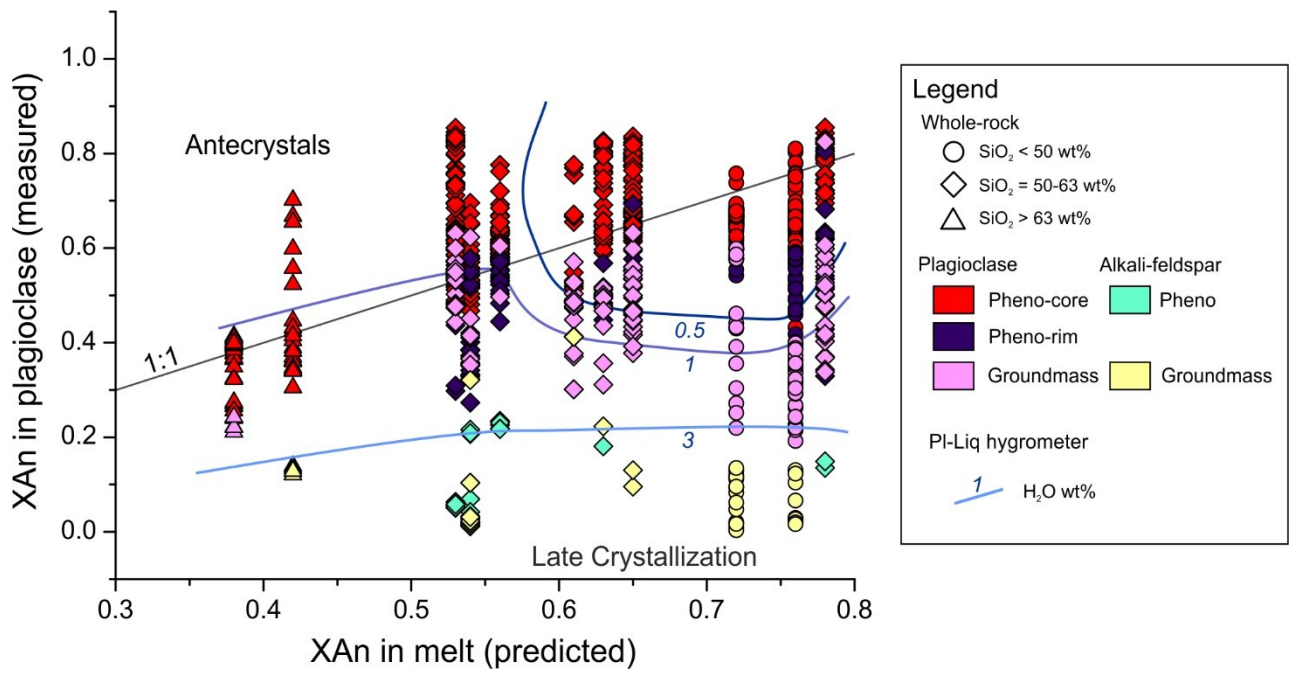
1966

1967 **Figures-9.** Clinopyroxene-melt equilibrium tests: (a) DiHd: diopside-hedenbergite, (b) EnFs: enstatite-  
 1968 ferrosilite, and (c) CaTs: Ca-Tschermak components. Equilibrium associated with observed components in  
 1969 pyroxenes are paired with predicted components in respective hosting-melts. The accepted range of  
 1970 equilibrium is indicated in each figure by dashed lines. Nominal melt compositions for clinopyroxene are  
 1971 selected from **whole-rock analyses**. Symbols and colors refer to Fig. 6.

1972

1973

1974 **Figure 10**



1975

1976

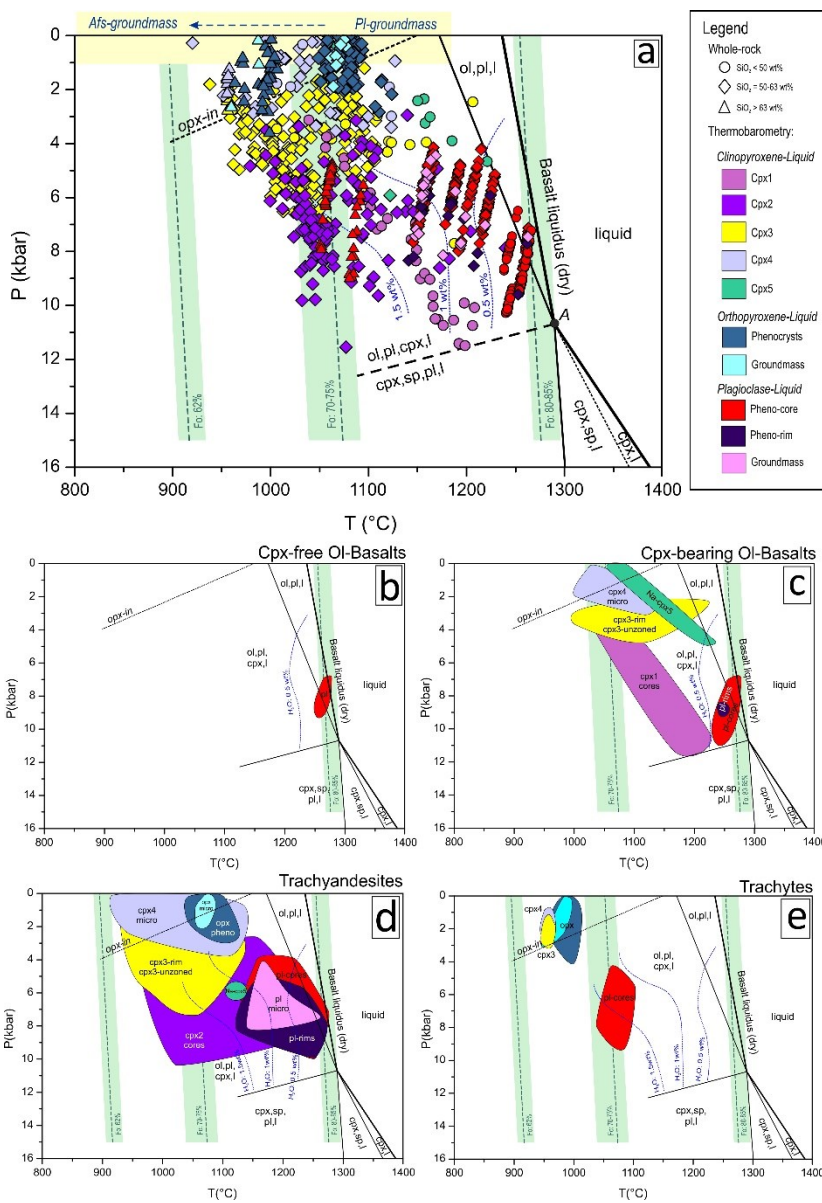
1977 **Figure-10.** Plagioclase-melt equilibrium test. Equilibrium associated with anorthite (XAn) component in  
1978 plagioclase are paired with predicted anorthite in melt. Nominal melt compositions for **plagioclase** are  
1979 selected from whole-rock **analyses**. Calculated water concentrations using **plagioclase-melt hygrometer**  
1980 (Putirka, 2008) are reported in diagrams with isolines (graded blue lines). Symbols and colors refer to Fig. 5.

1981

1982

1983

1984



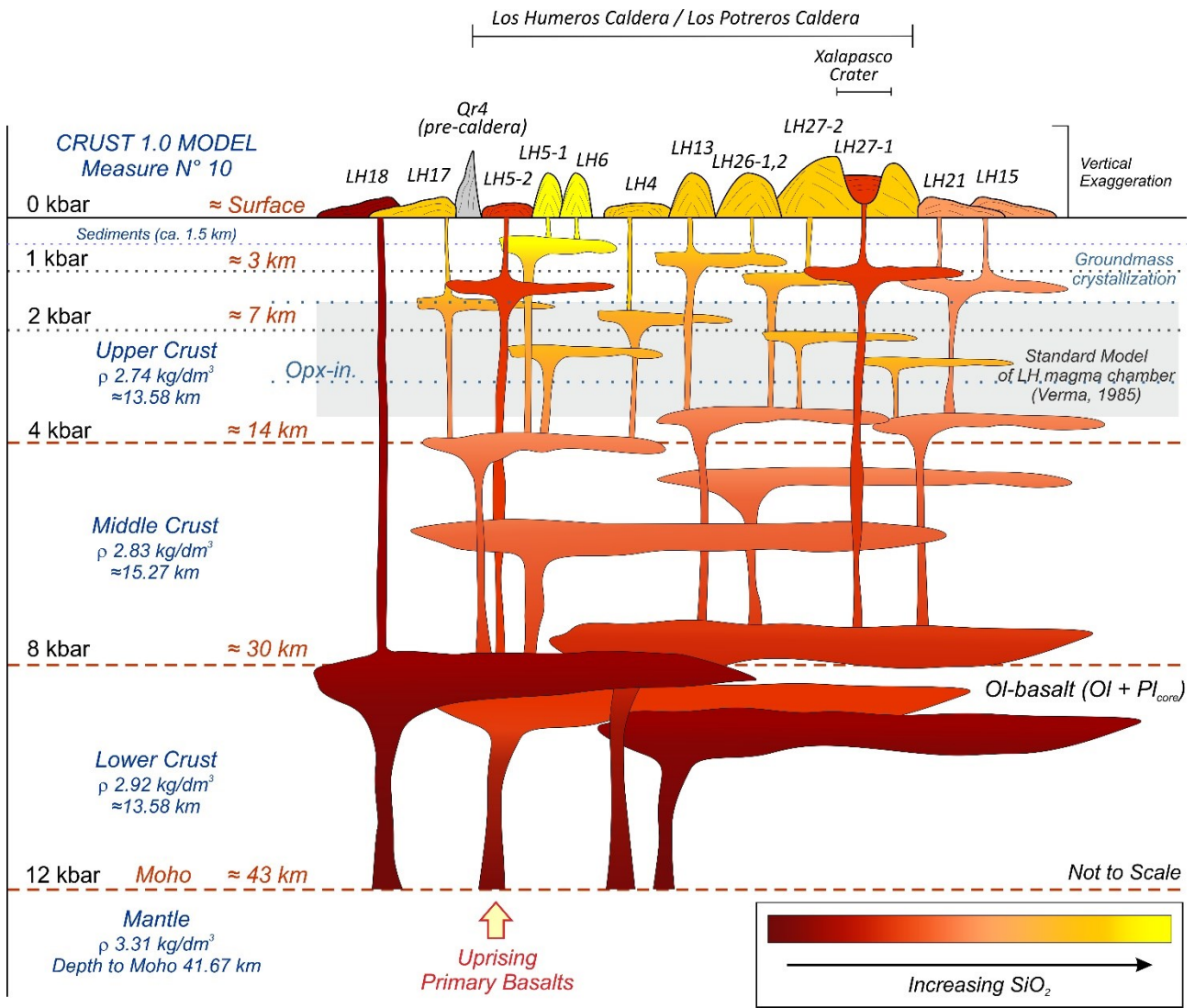
1986

1987

1988 **Figure-11. Thermobarometric estimates; a)** A summary of the results obtained from thermobarometry  
 1989 models applied to Los Humeros post-caldera stage lavas. Symbols refer to whole-rock chemistry  
 1990 compositions, whereas colors of different phases refer to mineral chemistry diagrams. Green-shaded field  
 1991 shows the results of olivine-liquid thermometry. Blue dashed isolines represent the results of plagioclase-  
 1992 melt hygrometer. Yellow-shaded field indicates pressure-temperature domain of crystallization of feldspars  
 1993 in groundmass. Basalt liquidus curve, ol+cpx+ol+sp+l stability fields and point “A” (basalt liquidus in  
 1994 equilibrium with mantle peridotite mineral assemblage of ol+cpx) are redrawn after Grove (2000). Opx-in  
 1995 stability curve is redrawn after Wallace and Anderson (2000). **Schematized results are presented separately**  
 1996 **for b) cpx-free ol-basalt; c) cpx-bearing ol-basalts; d) trachyandesites; and e) trachytes.**

1997

1998



2000  
2001  
2002  
2003  
2004  
2005  
2006  
2007  
2008  
2009

**Figure-12.** Schematic representation (not to scale) of the magmatic plumbing system feeding LHPCS activity, beneath Los Humeros caldera as derived by pressure-temperature estimates obtained from mineral-liquid thermobarometry models. The conceptual model is integrated with the crustal structure of the study area as derived by the Measure N°10 of the Crust 1.0 global Model (Davies, 2013). Grey shaded field indicates the depth and thickness of the existing conceptual model of a single, huge classical magma chamber proposed by Verma (1985a, 1985b) and mainly related to the Los Humeros caldera-stage activity.

2010 **Table 1**

**Table 1 - Major element bulk-rock compositions of LHPCS studied lava samples.**

Rock type	Basalts			Trachyandesites								Trachytes	
Sample	LH5-2	LH18	LH27-1	LH17	LH15-1	LH21-2	LH4	LH27-2	LH13	LH26-1	LH26-2	LH5-1	LH6-1
SiO <sub>2</sub> , wt%	46.51	48.78	49.35	54.43	54.74	55.24	56.18	59.69	61.74	61.85	62.14	64.93	67.58
TiO <sub>2</sub>	1.471	1.490	1.372	1.394	1.075	1.561	1.375	1.016	0.882	0.889	0.933	0.738	0.605
Al <sub>2</sub> O <sub>3</sub>	16.23	16.17	17.11	16.33	20.68	15.99	16.57	17.39	15.68	15.70	16.82	15.47	15.83
Fe <sub>2</sub> O <sub>3</sub> <sup>tot</sup>	10.78	10.62	10.26	8.08	6.49	8.62	7.88	5.76	5.15	5.22	5.32	4.58	3.73
MnO	0.161	0.160	0.155	0.123	0.092	0.133	0.114	0.087	0.085	0.085	0.095	0.077	0.074
MgO	8.44	8.29	7.97	3.57	3.28	3.45	2.90	2.36	2.72	2.45	2.24	1.18	0.69
CaO	10.14	9.77	10.67	7.04	8.59	6.42	6.52	4.83	4.85	4.66	4.52	2.81	2.12
Na <sub>2</sub> O	3.11	2.98	3.21	4.10	3.68	4.14	3.96	4.31	4.19	4.31	4.30	4.79	5.26
K <sub>2</sub> O	0.33	0.41	0.30	1.76	1.64	1.86	1.99	2.20	2.67	2.58	2.76	3.44	3.89
P <sub>2</sub> O <sub>5</sub>	0.19	0.21	0.17	0.32	0.26	0.34	0.34	0.27	0.25	0.23	0.22	0.18	0.13
LOI	1.90	0.81	-0.35	0.90	0.49	0.52	1.19	1.55	0.50	0.93	0.70	0.73	0.31
Total (wt%)	99.27	99.68	100.20	98.05	101.01	98.29	99.02	99.47	98.72	98.91	100.10	98.92	100.20
Mg#	61	61	61	47	50	44	43	45	51	48	45	34	27

Note: LOI - loss on ignition; Mg# - molar [Mg\*100/(Mg + Fe<sup>tot</sup>)].

2011

2012